



저작자표시-비영리-동일조건변경허락 2.0 대한민국

이용자는 아래의 조건을 따르는 경우에 한하여 자유롭게

- 이 저작물을 복제, 배포, 전송, 전시, 공연 및 방송할 수 있습니다.
- 이차적 저작물을 작성할 수 있습니다.

다음과 같은 조건을 따라야 합니다:



저작자표시. 귀하는 원 저작자를 표시하여야 합니다.



비영리. 귀하는 이 저작물을 영리 목적으로 이용할 수 없습니다.



동일조건변경허락. 귀하가 이 저작물을 개작, 변형 또는 가공했을 경우에는, 이 저작물과 동일한 이용허락조건하에서만 배포할 수 있습니다.

- 귀하는, 이 저작물의 재이용이나 배포의 경우, 이 저작물에 적용된 이용허락조건을 명확하게 나타내어야 합니다.
- 저작권자로부터 별도의 허가를 받으면 이러한 조건들은 적용되지 않습니다.

저작권법에 따른 이용자의 권리는 위의 내용에 의하여 영향을 받지 않습니다.

이것은 [이용허락규약\(Legal Code\)](#)을 이해하기 쉽게 요약한 것입니다.

[Disclaimer](#)



공학박사 학위논문

SURFACE COATING OF IMPLANTABLE  
MEDICAL DEVICES FOR ADDED  
THERAPEUTIC FUNCTIONALITY

치료 기능 부가를 위한 이식형  
의료기기의 표면 코팅 연구

2015년 2월

서울대학교 대학원

협동과정 바이오엔지니어링 전공

박민

SURFACE COATING OF IMPLANTABLE  
MEDICAL DEVICES FOR ADDED THERAPEUTIC  
FUNCTIONALITY

치료 기능 부가를 위한 이식형 의료기기의 표면 코팅  
연구

지도 교수 최 영 빈

이 논문을 공학박사 학위논문으로 제출함

2014년 11월

서울대학교 대학원

협동과정 바이오엔지니어링 전공

박 민

박 민의 공학박사 학위논문을 인준함

2014년 12월

위원장 김희찬 (인)

부위원장 최영빈 (인)

위원 윤형진 (인)

위원 이정찬 (인)

위원 홍진기 (인)

Ph.D. Dissertation

SURFACE COATING OF IMPLANTABLE  
MEDICAL DEVICES FOR ADDED THERAPEUTIC  
FUNCTIONALITY

BY

MIN PARK

FEBRUARY 2015

INTERDISCIPLINARY PROGRAM FOR BIOENGINEERING  
THE GRADUATE SCHOOL  
SEOUL NATIONAL UNIVERSITY

SURFACE COATING OF IMPLANTABLE  
MEDICAL DEVICES FOR ADDED THERAPEUTIC  
FUNCITONALITY

BY

MIN PARK

INTERDISCIPLINARY PROGRAM FOR BIOENGINEERING  
THE GRADUATE SCHOOL  
SEOUL NATIONAL UNIVERSITY

THIS DISSERTATION IS APPROVED FOR THE  
DEGREE OF DOCTOR OF PHILOSOPHY

DECEMBER 2014

DOCTORAL COMMITTEE:

Chairman

*Hee Chan Kim, Ph. D.*

Vice Chairman

*Young Bin Choy, Ph. D.*

Member

*Hyung-Jin Yoon, M.D., Ph. D.*

Member

*Jung Chan Lee, Ph. D.*

Member

*Jin kee Hong, Ph. D.*

## Abstract

# SURFACE COATING OF IMPLANTABLE MEDICAL DEVICES FOR ADDED THERAPEUTIC FUNCTIONALITY

By

Min Park

Interdisciplinary Program for Bioengineering  
The Graduate School  
Seoul National University

This dissertation is described with material, design, fabrication and analysis/evaluation for surface coating of implantable medical devices, *i.e.*, bone fixation systems and silicone implants, in order to add the therapeutic functionality. Even though the implantable medical devices have been widely developed and used in the clinical field, these still have drawbacks associated with lack of therapeutic functionality. To solve these, we suggest a promising multifunctional medical device adding therapeutic functionality, maintaining intact functionality of the implantable

medical device.

Firstly, in order to control the corrosion rate of magnesium (Mg), we coated the surface of magnesium (Mg) with a biodegradable polymer, polycaprolactone (PCL) and varied coating thickness in a reproducible manner using an automated apparatus designed to follow the widely-accepted dip-coating method. Herein, PCL served as a good permeation barrier owing to its hydrophobicity and slower degradation in biological fluid than Mg. As we increased the coating thickness from 0 to  $13.31 \pm 0.36 \mu\text{m}$ , the volume of hydrogen gas and amount of Mg ions, the indicators of Mg corrosion, decreased by almost half from  $0.57 \text{ ml/cm}^2/\text{day}$  and  $0.55 \text{ mg/day}$  to  $0.20 \text{ ml/cm}^2/\text{day}$  and  $0.26 \text{ mg/day}$ , respectively. Therefore, we demonstrated that the thicker coating could better hinder the water permeation to the Mg surface and thus, a corrosion rate could be reduced in this work. Secondly, we prepared a bone plate enabled with local, sustained release of alendronate, which is a drug known to inhibit osteoclast-mediated bone resorption and also expedite bone-remodeling activity of osteoblasts. For this, we coated a bone plate already in clinical use (PLT-1031, Inion, Finland) with a blend of alendronate and a biocompatible polymer, azidobenzoic acid-modified chitosan (i.e., Az-CH) photo-crosslinked by UV irradiation. As we performed the *in vitro* drug release study, the drug was released from the coating at a rate of  $4.03 \mu\text{g/day}$  for 63 days in a sustained manner. To examine the effect on bone regeneration, the plate was fixed on an 8 mm cranial critical size

defect in living rats and a newly formed bone volume was quantitatively evaluated by micro-computed tomography (micro-CT) at schedule times for 8 weeks. At 8 week, the group implanted with the plate enabled with sustained delivery of alendronate showed a significantly higher volume of newly formed bone ( $52.78 \pm 6.84\%$ ) than the groups implanted with the plates without drug ( $23.6 \pm 3.81\%$ ) ( $p < 0.05$ ). The plate enabled with alendronate delivery also exhibited good biocompatibility on H&E staining, which was comparable to the Inion plate already in clinical use. Therefore, we suggest that a bone plate enabled with local, sustained delivery of alendronate can be a promising system of a combined functionality of bone fixation and its expedited repair.

Lastly, we proposed the acute, local suppression of transforming growth factor beta (TGF- $\beta$ ), a major profibrotic cytokine, to reduce fibrosis around silicone implants. To this end, we prepared silicone implants that were able to release tranilast, a TGF- $\beta$  inhibitor, in a sustained manner for 5 days or 15 days. We performed histologic and immunohistochemical analyses for 12 weeks after the implantation of the implants in living rats. The capsule thicknesses and collagen densities significantly decreased compared with those around the non-treated silicone implants. Notably, early suppression of TGF- $\beta$  affected the fibrogenesis that actually occurs at the late stage of wound healing. This change may be ascribed to the decrease in monocyte recruitment mediated by early TGF- $\beta$  during the

acute inflammatory reaction. Thus, a significant decrease in differentiated macrophages was observed along with a decrease in the quantity of TGF- $\beta$  and fibroblasts during the subsequent inflammation stage; these changes led to a diminished fibrotic capsule formation.

---

**Keywords :** biopolymer, bone fixation system, coating, corrosion, fibrous capsule, silicone implant

**Student Number :** 2012–30967

# Contents

Abstract .....	i
Contents .....	v
List of Tables .....	ix
List of Figures .....	xi
Chapter 1. Introduction .....	1
1.1 Implantable Medical Devices .....	1
1.2 Bone Fixation system .....	7
1.2.1 Drawbacks of Bone Fixation system .....	12
1.3 Silicone Implant.....	16
1.3.1 Drawbacks of Silicone Implant.....	23
1.4 Research Purpose .....	28
Chapter 2. Surface Coating of Implantable Medical Devices .....	30
2.1 Surface Coating Technology .....	30
2.1.1 Dip Coating .....	31
2.1.2 Spray Coating .....	34
2.1.3 Drop Casting .....	37
2.2 Biopolymers as a Coating Material .....	39
2.2.1 Synthetic polymer: Polycaprolactone (PCL) and Poly(lactic-co-glycolic acid) (PLGA) .....	44
2.2.2 Natural polymer: Chitosan.....	53

<b>Chapter 3. Polycaprolactone Coating with Varying Thicknesses for Controlled Corrosion of Magnesium .....</b>	<b>60</b>
3.1 Introduction .....	60
3.2 Materials and Methods .....	64
3.2.1 Materials .....	64
3.2.2 Sample Preparation and Coating Process .....	65
3.2.3 Immersion test .....	66
3.2.4 Characterization of PCL coating .....	67
3.3 Results .....	68
3.3.1 Coating analysis .....	68
3.3.2 Coating Rate Analysis .....	69
3.3.3 Surface Characterization during Corrosion .....	71
3.4 Discussion .....	73
3.5 Conclusion .....	76

<b>Chapter 4. Acute Suppression of TGF- <math>\beta</math> with Local, Sustained Release of Tranilast against the Formation of Fibrous Capsules around Silicone Implants .....</b>	<b>90</b>
4.1 Introduction .....	90
4.2 Materials and Methods .....	94
4.2.1 Materials .....	94
4.2.2 Sample Preparation .....	95
4.2.3 Characterization .....	96

4.2.4 <i>In vivo</i> Animal Study .....	98
4.2.5 Histopatholoic Evaluation by Various Stainging Methods .....	99
4.2.6 Statistical Analysis .....	100
4.3 Results .....	101
4.3.1 Implant Characterization .....	101
4.3.2 Capsule Thickness .....	103
4.3.3 Collagen Density .....	105
4.3.4 Fibroblasts .....	106
4.3.5 TGF- $\beta$ .....	107
4.3.6 Monocytes/macrophages .....	109
4.4 Discussion .....	110
4.5 Conclusion .....	113

**Chapter 5. Bioabsorbable Bone Plates Enabled with Local,  
Sustained Delivery of Alendronate for Bone  
Regeneration .....** 149

5.1 Introduction .....	149
5.2 Materials and Methods .....	153
5.2.1 Materials .....	153
5.2.2 Synthesis of an Aziobenzoic Acid-Modified Chitosan (Az-CH) .....	154
5.2.3 Preparation of Bone Plate Samples .....	154
5.2.4 Characterizations of Az-CH .....	156
5.2.5 Characterizations of Az-CH .....	157

5.2.6 Measurement of Drug–Loading Amount.....	157
5.2.7 Measurement of Drug–Loading Amount .....	158
5.2.8 <i>In vivo</i> Drug Release Study .....	159
5.2.9 <i>In vivo</i> Cell Cytotoxicity Evaluation .....	159
5.2.10 <i>In vivo</i> Animal Study .....	160
5.2.11 Histopathologic Evaluation .....	162
5.2.12 Statistics.....	163
5.3 Results .....	163
5.3.1 Characterization of Az–CH .....	163
5.3.2 Characterization of Plate Samples .....	164
5.3.3 <i>In vitro</i> Drug Release Profile .....	166
5.3.4 Cytotoxicity .....	166
5.3.5 <i>In vivo</i> new bone formation .....	167
5.3.6 Histological Evaluation .....	168
5.4 Discussion .....	168
5.5 Conclusion .....	171
Chapter 6. General Conclusion .....	186
References .....	189
Abstract in Korean .....	199
Acknowledgement .....	202
Appendix .....	204

# List of Tables

Table 1.1	A comparison between specific orthopedic implant prosthetic materials .....	11
Table 1.2	Advantages and disadvantages of PDMS.....	18
Table 1.3	A Comparison table between saline– and silicone breast implant .....	19
Table 1.4	Incidence rate of various complications related to silicone implants .....	25
Table 2.1	List of Representative natural polymers .....	41
Table 2.2	List of Representative synthetic polymers....	42
Table 2.3	Various factors influencing biodegradation of polymers .....	43
Table 2.4	Physical properties of polycparolactone.....	49
Table 2.5	Degradation rate of biodegradable polymers .	50
Table 2.6	Various degradation times of PLGA depending on the ratio of co–monomers, i.e., lactic acid and glycolic acid .....	51
Table 2.7	Marketed products produced with PLGA, biodegradable polymer.....	52
Table 2.8	Specification of chitosan .....	56
Table 2.9	Principal properties of chitosan in relation to its use in biomedical engineering .....	57

Table 2.10 Various biomedical applications of chitosan .	58
Table 2.11 List of chitosan based formulations prepared by different methods .....	59
Table 3.1 Compositions of Hank's solution used for the immersion test .....	78
Table 3.2 Average thicknesses of PCL coatings according to the number of dippings .....	79
Table 5.1 Mechanical property of the plate samples prepared in this work .....	172

# List of Figures

Figure 1.1 U.S. implantable medical devices market in 2010–2018 .....	5
Figure 1.2 Global market share of implantable medical devices in 2011 .....	6
Figure 1.3 U.S. annual incidence of osteoporotic fractures compared to other diseases in 2011.....	14
Figure 1.4 X-ray images showing the failure of the bone fixation system (bone plates and screws) related to osteoporotic bone fractures .....	15
Figure 1.5 Molecular structure of polydimethylsiloxane (PDMS) consisting of silicone implant .....	20
Figure 1.6 US silicone market report in medical devices by application in 2008.....	21
Figure 1.7 Optical images of various silicone implants in clinical use .....	22
Figure 1.8 Optical images of capsular contracture formed around the silicone implants .....	26
Figure 1.9 (a) Smooth surface showing a geographical surface with rock formations and small pins and (b) textured surface depicting a granular surface pitted with cuboid shaped wells .....	27
Figure 2.1 Schematic illustration of dip coating .....	32

Figure 2.2 Landau and Levich equation for estimating thickness (H) of coating film .....	33
Figure 2.3 Schematic illustration of spray coating.....	35
Figure 2.4 Schematic illustration of screen printing using spray coating .....	36
Figure 2.5 Schematic illustration of drop casting .....	38
Figure 2.6 Molecular Structure of polycaprolactone (PCL) .....	47
Figure 2.7 Molecular structure of poly(lactic- <i>co</i> -glycolic acid) $x$ = number of units of lactic acid; $y$ = number of glycolic acid .....	48
Figure 2.8 Molecular structure of chitosan .....	55
Figure 3.1 Schematics of an automated apparatus for polycaprolactone (PCL) coating. The Mg coins were (a) loaded into the apparatus, (b) dipped into 5% w/v PCL solution for 5 s and (c) extracted to the air for 60 s, completing a single set of dipping process .....	80
Figure 3.2 Schematic illustration of a funnel system prepared for measurement of the hydrogen gas volume generated by Mg corrosion .....	81
Figure 3.3 SEM images of the surfaces of (a) NCM, (b) 1DCM, (c) 10DCM and (d) 50DCM. Scale bars = (a) 100 $\mu\text{m}$ and (b-d) 10 $\mu\text{m}$ , respectively.	

Figure 3.4 SEM images of the half-masked samples of (a) 1DCM, (b) 10DCM, and (c) 50DCM observed from the side. The white arrows each indicate the coating thickness, measured between the top of the coating and the Mg surface. Scale bars = 10  $\mu\text{m}$ . ..... 83

Figure 3.5 SEM images and EDS spectra obtained from (a) NCM, (b) 1DCM, (c) 10DCM and (d) 50DCM. Scale bars = (a) 100  $\mu\text{m}$  and (b-d) 10  $\mu\text{m}$ . ..... 84

Figure 3.6 Volume of hydrogen gas generated from NCM, 1DCM, 10DCM and 50DCM immersed in pH 7.4 Hank's solution at 37 °C ..... 85

Figure 3.7 Amount of Mg ions released from NCM, 1DCM, 10DCM and 50DCM immersed in pH 7.4 Hank's solution at 37 °C ..... 86

Figure 3.8 SEM images of the sample surfaces obtained during the immersion test. The samples and days of imaging were (a1) NCM, day 1; (a2) NCM, day 14; (b1) 1DCM, day1; (b2) 1DCM, day 14; (c1) 10DCM, day 1; (c2) 10DCM, day 14; (d1) 50DCM, day 1; and (d2) 50DCM, day 14. Scale bars = 200  $\mu\text{m}$ . ..... 87

Figure 3.9 EDS spectra and respective elemental compositions obtained from the samples during the immersion test. The samples and days of analysis were (a1) NCM, day 1; (a2) NCM, day 14; (b1) 1DCM, day 1; (b2) 1DCM, day 14; (c1) 10DCM, day 1; (c2) 10DCM, day 14; (d1) 50DCM, day 1; and (d2) 50DCM, day 14. Scale bars = 200  $\mu$ m. .... 88

Figure 4.1 Schematic illustration of the coating procedure for the silicone implant ..... 115

Figure 4.2 Optical images of the silicone implants prepared in this work. (a) Shell of a silicone implant cut into a circle, 2 cm in diameter (*i.e.*, ca. 3  $\text{cm}^2$  in area) and 1.5 mm in thickness. (b) Two of the circular shells, shown in (a), were then bonded with medical epoxy to create the implant sample used in this work. Scale bars: 5 mm ..... 116

Figure 4.3 Procedure of implantation surgery on SD rat dorsal region. Male Sprague–Dawley rats aged 8 weeks and weighing 250–300 g were used for the *in vivo* animal experiments in the current study. The animals were maintained under a 12/12 h light/dark cycle with free

access to water and food during the entire experimental period. The protocol was approved by the Institutional Animal Care and Use Committee at Seoul National University Bundang Hospital (BA1102-077/006-01). For implant insertion, (a) the animals were each anesthetized using an intraperitoneal injection of a mixture (0.1 ml/kg) of Zoletil® 50 and Rompun® (1:1 v/v). Then, the hair on the dorsal area was shaved. (b) Before incision, the surgical site was marked with a surgical pen. (c) A 2 cm incision was made along the vertebra, and (d) a pocket was made via the subpanniculus plane using a surgical scissor. (e) The sample was inserted in the pocket. (f) The incision was closed with nylon 4-0 thread (Ethicon, Cornelia, GA, USA), and the surgical site was disinfected again with Betadine. .... 117

Figure 4.4 Scanning electron micrographs of the surfaces of (a) IM, (b) PLGA\_IM, (c) TR\_IM and (d) PLGA\_TR\_IM. The scale bars represent 100  $\mu\text{m}$ ..... 118

Figure 4.5 Fourier transform infrared (FTIR) spectra of

(a) intact tranilast, (b) intact PLGA, (c) IM, (d)	
PLGA_IM, (e) TR_IM and (f) PLGA_TR_IM. 119	
Figure 4.6 <i>In vitro</i> drug release profiles of the TR_IM and PLGA_TR_IM ..... 120	
Figure 4.7 Evaluation of the thickness of the capsule formed around the implants. (a) Mean capsule thickness at each biopsy time and (b) representative histological images around the implants using H&E staining at week 12. Scale bars: 1 mm. The images were obtained from (A) IM, (B) PLGA_IM, (C) TR_IM and (D) PLGA_TR_IM samples. The double-sided arrow indicates the capsule thickness in the image. The single-sided arrow indicates the location of the implant in the image. The asterisk (*) represents a significant difference compared with the IM group ( $P < 0.05$ ). Double asterisks (**) represent a significant difference between the TR_IM and PLGA_TR_IM groups ( $P < 0.05$ ). ..... 121	
Figure 4.8 Representative images around the implants with H&E staining for evaluation of the capsule thickness. The images were obtained from the (A) IM, (B) PLGA_IM, (C) TR_IM and (D)	

PLGA\_TR\_IM samples at (a) week 1, (b) week 2, (c) week 4, (d) week 8 and (e) week 12. The thinnest region from each of the sample images was chosen to measure the capsule thickness, as indicated with the double-sided arrow. The single-sided arrow indicates the location of the implant in the image. Scale bars, 1 mm. .... 122

Figure 4.9 Evaluation of the density of collagen deposition around the implants. (a) Mean collagen density at each biopsy time and (d) representative histological images around the implants using MT staining at week 12. Scale bars: 100  $\mu\text{m}$ . The images were obtained from (A) IM, (B) PLGA\_IM, (C) TR\_IM and (D) PLGA\_TR\_IM samples. The arrow indicates the location of the implant in the image. The asterisk (\*) represents a significant difference compared with the IM group ( $P < 0.05$ ). Double asterisks (\*\*) represent a significant difference between the TR\_IM and PLGA\_TR\_IM groups ( $P < 0.05$ ). .... 125

Figure 4.10 Representative images around the implants with MT staining for week 12. Scale bars: 100  $\mu\text{m}$ . The arrow

indicates the location of the implant in the image. .... 126

Figure 4.11 Evaluation of the number of fibroblasts around the implants. (a) Mean grading scores of fibroblasts at each biopsy time and (b) representative IHC images around the implants at week 12. Scale bars: 100  $\mu\text{m}$ . The images were obtained from (A) IM, (B) PLGA\_IM, (C) TR\_IM and (D) PLGA\_TR\_IM samples, and the arrow indicates the location of the implant in the image. The asterisk (\*) represents a significant difference compared with the IM group ( $P < 0.05$ ). Double asterisks (\*\*) represent a significant difference between the TR\_IM and PLGA\_TR\_IM groups ( $P < 0.05$ ). .... 129

Figure 4.12 Representative images around the implants with IHC staining for evaluation of the fibroblast quantity. The images were obtained from the (A) IM, (B) PLGA\_IM, (C) TR\_IM and (D) PLGA\_TR\_IM samples at (a) week 1, (b) week 2, (c) week 4, (d) week 8 and (e) week 12. Scale bars: 100  $\mu\text{m}$ . The arrow indicates the location of the implant in the

image. .... 130

Figure 4.13 Evaluation of the degree of TGF- $\beta$  expression around the implants. (a) Mean grading scores of TGF- $\beta$  expression at each biopsy time and representative IHC images at (b) week 2 and (c) week 12. Scale bars: 100  $\mu\text{m}$ . The images were obtained from (A) IM, (B) PLGA\_IM, (C) TR\_IM and (D) PLGA\_TR\_IM samples, and the arrow indicates the location of the implant in the image . The asterisk (\*) represents a significant difference compared with the IM group ( $P < 0.05$ ). Double asterisks (\*\*) represent a significant difference between the TR\_IM and PLGA\_TR\_IM groups ( $P < 0.05$ ) 133

Figure 4.14 Representative images around the implants with IHC staining for evaluation of the TGF- $\beta$  expression. The images were obtained from the (A) IM, (B) PLGA\_IM, (C) TR\_IM and (D) PLGA\_TR\_IM samples at (a) week 1, (b) week 2, (c) week 4, (d) week 8 and (e) week 12. Scale bars: 100  $\mu\text{m}$ . The arrow indicates the location of the implant in the image. .... 134

Figure 4.15 Evaluation of the acute inflammation around

the implant with H&E staining. (a) The degree of acute inflammation was semi-quantitatively evaluated according to the number of inflammatory cells, such as polymorphonuclear leukocytes (PMNs), with the analysis yielding the following grades: 0 (None), 1 (Mild), 2 (Moderate) and 3 (Severe). At each biopsy time and for each implant sample, five images were obtained from each of the five animals, giving a total of 25 images for statistical analysis. The representative images were obtained from the implants of (A) IM, (B) PLGA\_IM, (C) TR\_IM and (D) PLGA\_TR\_IM at (b) week 1, (c) week 2, (d) week 4, (e) week 8 and (f) week 12. Scale bars: 100  $\mu$ m. The arrow indicates the location of the implant in the image. The number of inflammatory cells continuously decreased until week 12; this decrease suggests that the acute inflammation gradually decreased. At each biopsy time, there were no significant differences in the number of inflammatory cells among all the experimental groups. This result indicates that the release

of tranilast had no great impact on the overall resolution of acute inflammation during the entire period of experiments. Of note, the degree of cellularity was relatively higher until week 2, possibly because the acute inflammation was prolonged due to the presence of the bulky silicone implant in the wounds..... 137

Figure 4.16 Evaluation of monocyte and macrophage quantity. (a) Mean grading scores of monocyte/macrophage quantity at each biopsied time and representative IHC images at (b) week 8 and (c) week 12. Scale bars: 100  $\mu\text{m}$ . The images were obtained from (A) IM, (B) PLGA\_IM, (C) TR\_IM and (D) PLGA\_TR\_IM samples, and the arrow indicates the location of the implant on the image. The asterisk (\*)represents a significant difference compared with the IM group ( $P < 0.05$ ). Double asterisks (\*\*) represent a significant difference between the TR\_IM and PLGA\_TR\_IM groups ( $P < 0.05$ ) 141

Figure 4.17 Representative images around the implants with IHC staining for evaluation of the

monocyte/macrophage quantity. The images were obtained from the (A) IM, (B) PLGA\_IM, (C) TR\_IM and (D) PLGA\_TR\_IM samples at (a) week 1, (b) week 2, (c) week 4, (d) week 8 and (e) week 12. Scale bars: 100  $\mu\text{m}$ . The arrow indicates the location of the implant in the image. ..... 142

Figure 4.18 Evaluation of monocyte quantity. (a) Mean grading scores of monocyte quantity at each biopsied time and representative IHC images at (b) week 1 and (c) week 2. Scale bars: 100  $\mu\text{m}$ . The images were obtained from (A) IM, (B) PLGA\_IM, (C) TR\_IM and (D) PLGA\_TR\_IM samples, and the arrow indicates the location of the implant on the image. The asterisk (\*) represents a significant difference compared with the IM group ( $P < 0.05$ ). Double asterisks (\*\*) represent a significant difference between the TR\_IM and PLGA\_TR\_IM groups ( $P < 0.05$ ). 145

Figure 4.19 Representative images around the implants with IHC staining for evaluation of the monocyte quantity. The images were obtained from the (A) IM, (B) PLGA\_IM, (C) TR\_IM

and (D) PLGA\_TR\_IM samples at (a) week 1, (b) week 2, (c) week 4, (d) week 8 and (e) week 12. Scale bars: 100  $\mu\text{m}$ . The arrow indicates the location of the implant in the image. .... 146

Figure 5.1 (A) Schematic illustration of coating procedure. The coating solution was prepared by dissolving Az-CH or a blend of Az-CH and alendronate in an aqueous acetic acid solution (2% v/v) for preparation of the Az-CH\_P or AL\_Az-CH\_P, respectively. (B) Optical images of the plate samples (a) without and (b) with the coating. The arrows indicate the locations of the coatings. The scale bars represent 3 mm. .... 173

Figure 5.2 Optical images of the plate samples (A) without and (B) with the coating used for evaluation of mechanical property and in vivo bone regeneration. The arrows indicate the locations of the coatings. The scale bars are 5 mm. .... 175

Figure 5.3 (A) UV spectra of (a) chitosan, (b) 4-azidobenzoic acid, and (c) Az-CH. (B) FTIR

spectra of (a) chitosan, (b) 4-azidobenzoic acid and (c) Az-CH, respectively. ....	176
Figure 5.4 Scanning electron micrographs of the surfaces (A) without and (B) with the coating on the AL-Az-CH_P. The scale bars represent 100 $\mu\text{m}$ .....	178
Figure 5.5 FTIR spectra of (a) IP, (b) Az-CH, (c) alendronate, (d) Az-CH_P and (e) AL-Az-CH_P. The dashed lines indicate the major peaks from IP, Az-CH and alendronate, respectively. .....	179
Figure 5.6 Stress-strain curve obtained from the plate samples prepared in this work using a universal-testing machine (UTM; Instron-5543, MA, USA) equipped with a load cell of 71 kN, where both ends of the sample were clamped and pulled at a rate of 3 mm/min until break. ....	180
Figure 5.7 <i>In vitro</i> drug release profiles of the AL-Az-CH_P.....	181
Figure 5.8 Cytotoxicity evaluation of the plate samples. The number of L929 fibroblasts adhering to the surfaces of the IP, Az-CH_P and AL-Az-CH_P were assessed. ....	182

Figure 5.9 Micro-CT image analysis on new bone formation in cranial defects of the animal group with no treatment and the ones fixed with the IP, Az-CH\_P and AL-Az-CH\_P at 1, 4 and 8 weeks after implantation. (A) Micro-CT images and (B) new bone volume percent around the cranial defects. \*At 4 and 8 weeks, the AL-Az-CH\_P group was statistically significantly different from the no treatment group. (p < 0.05). ..... 183

Figure 5.10 Histological images from the tissue around the cranial defect obtained at 8 week after implantation of the plate samples. The arrows indicate the specific locations of new bone formation. The scale bars represent 100  $\mu\text{m}$ .

185

# Chapter 1

## Introduction

### 1.1 Implantable Medical Devices

Implantable medical devices are defined as devices fabricated to improve an existing biological structure, support or improve a damaged biological system by implanting the medical devices into the body (1). The representative examples of the implantable medical devices are pace makers, cochlear implants, drug delivery devices, drug-eluting stents, silicone implants or orthopedic implants such as bone plate/screw, pin or rods. In the United States (US), the Food and Drug Administration (FDA) requires manufacturers of the implantable medical devices to demonstrate safety and effectiveness before these can be

marketed, that is, indicating that FDA approval means “reasonable assurance of safety and effectiveness (2). By the FDA, a variety of medical devices are classified with three regulations: Class I, Class II and Class III. The classifications are assigned by the degree of the risk that the medical devices give the patients and the level of regulatory control that the FDA determines is necessarily needed to legally market the medical devices. Generally, as the level of classification increases, the risk to the patients increases. The regulatory classifications of medical devices are described below(3):

Class I: The medical devices have minimal potential harm to the patients. The devices are typically simple in design and have a history of safe use. Examples of Class I devices are arm slings and hand-held surgical instruments.

Class II: The medical devices have general controls that are not sufficient to assure safety and effectiveness. Class II medical devices are needed to comply with Special Controls which include below;

- Special labeling requirements,
- Mandatory performance standards, both International and United States
- Postmarket surveillance

- FDA medical device specific guidance

Class II devices usually need pre-market notification by submission and FDA review of a 510(k) clearance to market submission. Examples of Class II devices are physiologic monitors, x-ray systems, gas analyzers, pumps, and surgical drapes.

Class III: The medical devices have the most stringent regulatory control. Class III medical devices generally maintain or support human life. These devices are the most important in hindering impairment of human health or an unreasonable risk of disease or injury to the patients. Examples of Class III devices are: replacement heart valves, orthopedic implants, silicone gel-filled breast implants, and implanted cerebella stimulators.

According to one of the U.S. reports of implantable medical devices market, it is expected that U.S. demand for implantable medical devices will increase about 5 % annually to \$ 80 million in 2018 (Figure 1.1). Additionally, considering a global market share of implantable medical devices in 2011, the U.S. is the largest market in the world and occupies almost 41 % of all global markets (Figure 1.2). Especially, it is reported that

orthopedic implants will occupy the largest segment among various implantable medical implants, showing 8.8 % of the growth rate annually due to technological advances and safety improvement.

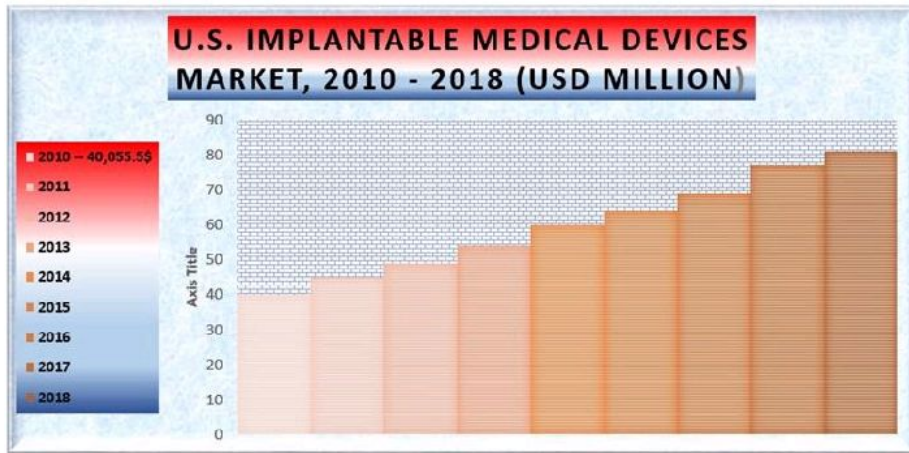


**Fig. 1.1** U.S. implantable medical devices market in 2010-2018

*Ref. <http://resources.infosecinstitute.com>*

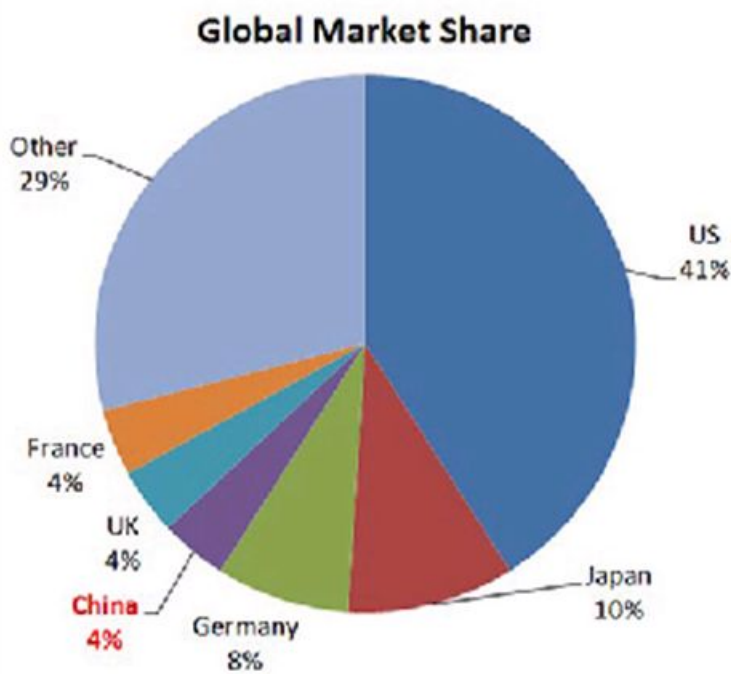


**Fig. 1.2** Global market share of implantable medical devices in 2011

**Ref.** <http://www.novotekchina.com>

## 1.2 Bone Fixation System

Bone fixation systems are defined as stabilizing frames to hold the broken bones in proper position(4). Examples of the bone fixation systems include bone plate/screw, pins, rods, nails and wires. Generally, the bone fixation systems are divided into two categories(5); one is external fixation system and the other is internal fixation system(6). In case of the former, orthopedic pins or screws are placed into the bone via small incisions into the skin or muscle. Then, the pins or screws are attached to the plate outside the skin. The external fixation systems have been usually used as a temporary treatment for fractures. Especially, since they can easily be applied, the external fixation systems are often put on when multiple injuries occur to the patients and a surgery to fix the fractured bones is not yet prepared. In other words, the external bone fixation systems give the patients good, temporary stability until the patients become healthy enough for the final surgery. In case of the latter, the internal fixation systems enable the patients with fractured bones to return the normal life early and allows shorter hospital stays and reduces the incidence of nonunion and malunion of fractured bones.

The bone plates mainly act to hold the broken pieces of bone together(7). They are attached to the bone with screws and needed to be removed or biodegraded after healing is complete. The bone screws are generally designed depending on the various types of the fractured bones. They are also fabricated with different sizes or shapes based on bones with different sizes. They can be used without or with plates, rods or nails in order to hold the fractured bones. Like bone plates, screws may be degraded or removed after bone healing is complete. When the long bones are fractured, the best way to hold the pieces of the fractured bones together is to insert nails or rods into the hollow center of the bone. Additionally, screws can be used at both ends of the rods to prevent the fractured bones from rotating, shortening, thereby holding the rods in proper place until the fractured bones are fully healed. This is usually applied to heal the majority of fractures in the femur as well as tibia. The wires are also used to pin the bones back together. They can be utilized to hold pieces of bones together which are too small to be fixed with screws. Especially, they are used to treat fractures of small bones including those found in the foot or hand.

The bone fixation systems have been fabricated with a variety of materials such as metals, composites, non-biodegradable

polymers (i.e., UHMWPE), ceramics or biodegradable polymers (4, 8, 9). Titanium and its alloys, stainless steel and cobalt–chromium alloys are representative metals which have been widely used to fabricate metallic bone fixation systems(8). These metals have each advantage and disadvantage, as shown in Table 1.1. For example, titanium and its alloys have relatively high yield strength and stainless steel has relatively high ductility. Cobalt–chromium alloy has excellent resistance against fatigue and cracking. Composites are manufactured in several ways; mechanical bonding between materials, chemical bonding and physical bonding. Their advantages are that extreme variability in properties is possible. Meanwhile, there are problems like matrix cracking or debonding of fiber from matrix. The examples of composites are fiberglass, concretes and laminates. Ceramics are also used to develop the bone fixation systems due to its high compressive strength and high biocompatibility(10). However, they have drawbacks such as a difficulty to process owing to very high melting point and low tensile strength. UHMWPE (Ultra High Molecular Weight Polyurethane) has many benefits including high density, superior wear characteristics and low friction(11). By these advantages, UHMWPE has been widely used to fabricate total joint

arthoplasty. Metallic bone fixation systems are often removed through secondary surgery since they are not degraded after bone healing is complete. Owing to problems associated with the secondary surgery, bioabsorbable bone fixation systems have been developed and are composed of biodegradable polymers such as poly(lactic-co-glycolic acid) (PLGA) or poly(lactic acid) (PLA) (9). However, the bioabsorbable bone fixation systems have relatively lower mechanical strength compared to metallic bone fixation systems, thereby limited use in parts of the fractured bones.

Metals	Titanium	Cobalt-chromium-molybdenum	Stainless steel
Chemical make-up	Ti6Al4V	30~60 % Co 20~39 % Cr 7~10 % Mo	Cr, Ni, Mo Cr oxide layer when dipped in Nitric acid
Young's modulus	110GPa	200 GPa	190 GPa
Benefits	Yield strength, Ti > stainless steel	Stronger and more corrosion resistance to fatigue, cracking and stress	Strong, cheap, relatively biocompatible
Uses	Cementless joint replacements, fracture fixation devices	Total joint arthroplasty, need to be inserted with a lower modulus polymer cement for fixation to prevent stress shielding of surrounding bone	Rarely used in new designs in joint replacement, fracture fixation devices
problems	Poor wear characteristics	Co, Cr, Mo known to be toxic in ionic form, high modulus	Excessively corrosive in some cases Susceptible to fatigue cracking Very high modulus

**Table 1.1 A Comparison Between Specific Orthopedic Implant Prosthetic Materials**

**Ref.** Dumbleton JH, Black J: *An Introduction to Orthopaedic Materials, chap 8. Springfield, IL, Charles C Thomas, 1975*

**Ref.** Ludwigson DC: Requirements for metallic surgical implants and prosthetic devices. *Metals Engineering Quarterly: American Society of Metallurgists 1, 1965*

**Ref.** Mears DC: *Materials and Orthopaedic Surgery. Baltimore, Williams & Wilkins, 1979*

### 1.2.1 Drawbacks of Bone Fixation Systems

Among various reasons inducing bone fractures, the fractured bones associated with osteoporosis give the most serious problem to the patients with osteoporosis(5). It is reported that osteoporotic fractures occurs at least two times more annual incidences than heart shock (Fig. 1.3). Herein, osteoporosis is a progressive disease characterized by a decrease in bone mass and density(12). The osteoporotic patients often show a low bone density, thereby delaying bone healing. Owing to this, bone healing of osteoporotic can be problematic, especially, causing severe complications such as microfracture, malunion or loosening of the bone fixation systems even though proper fixation of fractured bone is applied (Figure 1.4)(13). It has been reported that failure of bone fixation systems occur in 2 % to 10 % of fractures related to osteoporosis.

Biocompatible metals including titanium alloy, stainless steel and cobalt–chromium alloy have been widely used for orthopedic fixation systems due to their relatively high mechanical strength(14). However, a secondary surgery is often used to remove these metallic bone fixation systems after bone healing is complete because they are not biodegraded in the body, thereby inducing low patient's compliance. To solve these problems, bioabsorbable bone fixation systems composed of biodegradable polymers such as poly(lactic–co–glycolic acid) (PLGA) or poly(lactic acid) (PLA) have been developed and

already approved in clinical use(9). However, such polymeric bone fixation systems are limited in their applications due to relatively lower mechanical strength. To meet the needs in both mechanical strength and biodegradability, magnesium (Mg) and its alloys have attracted significant attention for the use in bone fixation system(15). Especially, the mechanical properties of Mg are known to be similar to those of natural bone, as compared with the other metals commonly used for orthopedic implants(16). On the other hand, Mg is limited in orthopedic applications due to its high corrosion rate, resulting in rapid loss of mechanical strength before bone healing(17). This rapid corrosion of Mg also leads to high accumulation of hydrogen gas generated near the implantation site. This forms a hydrogen gas pocket, which often causes necrosis of tissues and separation between the implant and tissues, leading to delay in bone healing.

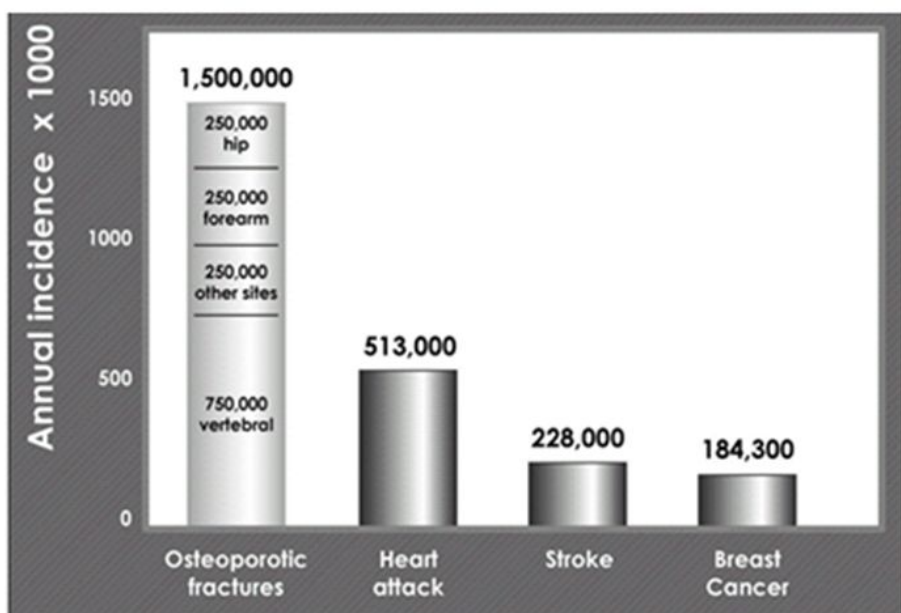


**Figure 1.3** U.S. annual incidence of osteoporotic fractures compared to other diseases in 2011

*Ref. <http://www.boneandjointburden.org>*

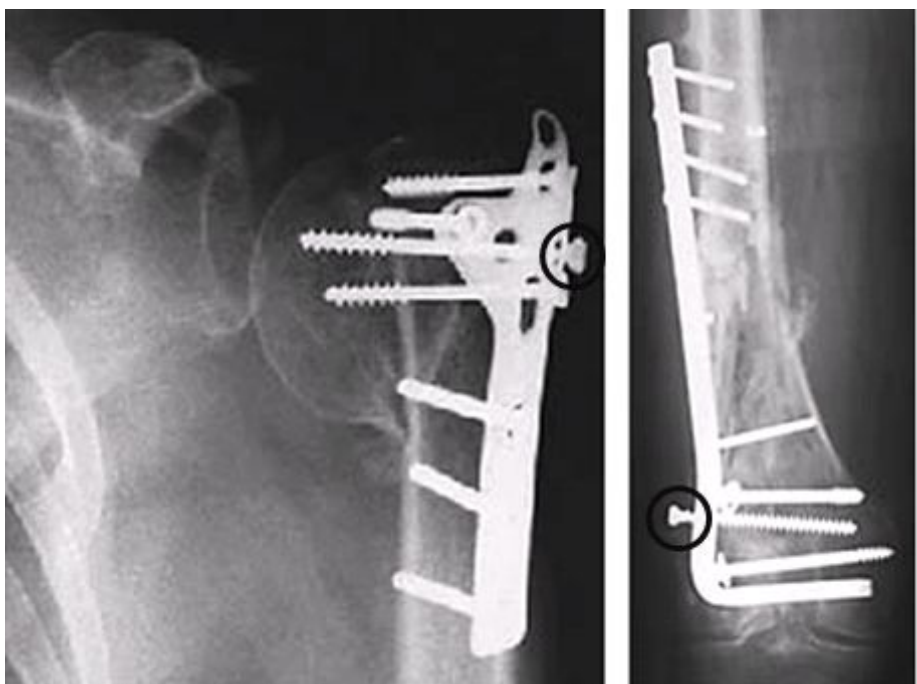


**Figure 1.4** X-ray images showing the failure of the bone fixation system (bone plates and screws) related to osteoporotic bone fractures.

*Ref. Stromsoe K. Fracture fixation problems in osteoporosis. Injury. 2004;35(2):107-13.*

### 1.3 Silicone Implants

A Medical silicone, called as PDMS, has been widely found for a variety of applications in the medical field due to its high biocompatibility, biodurability, low surface tension and chemical stability(18). Polydimethylsiloxane (PDMS) is a mixed inorganic-organic polymer with the chemical formula  $[R_2SiO]_n$ , where R is an methyl group as one of the organic groups such as methyl, ethyl or phenyl(18). The silicone consists of an inorganic silicon-oxygen backbone (i.e.,  $-Si-O-Si-O-Si-O-$ ) with organic side groups attached to the silicon atoms (Figure 1.5). Especially, silicone has many advantages and disadvantages, as shown in Table 1.2. The representative advantages of silicone are chemically inert, good thermal stable, easily and inexpensively fabrication whereas the disadvantages of that are extremely hydrophobic and strong tendency to adsorb other molecules onto the surface(19). According to a silicone market report of biomedical applications in US, catheters and tubing occupied the highest portion than any other devices. Then, the portion of the implants followed that of the catheters and tubing (Figure 1.6).

Silicone implants, as one of the many different kinds of medical devices composed of PDMS, have been widely used for breast

augmentation or reconstruction in plastic surgery(18). The silicone implant is defined as a prosthesis which changes size, shape and texture of woman's breast (Figure 1.7). There are two types of silicone implants; one is the saline implant filled with saline solution and the other is the silicone implant with viscous silicone gel (Table 1.3)(20). Both of them were already proved by FDA and saline is firmer and silicone has more cohesive feeling resembling a nature breast. However, when the silicone implants are ruptured after implantation, silicone gel induces more inflammation to the connective tissues around the silicone implant(21).

Advantages	Disadvantages
<ul style="list-style-type: none"> <li>• Isotropic and homogenous</li> <li>• Chemically inert</li> <li>• Optically transparent</li> <li>• Good thermal stability</li> <li>• Easily and inexpensively fabricated</li> </ul>	<ul style="list-style-type: none"> <li>• Extremely hydrophobic</li> <li>• Strong tendency to adsorb other molecules onto the surface</li> <li>• Unstable and poorly controlled</li> <li>• Electroosmotic flow</li> </ul>

**Table 1.2** Advantages and disadvantages of PDMS

*Ref. A. Mata, A.J. Fleischman, S. Roy, Characterization of polydimethylsiloxane (PDMS) properties for biomedical micro/nanosystems, Biomedical microdevices, 7 (2005) 281-293*

Silicone breast implant	Saline breast implant
<ul style="list-style-type: none"> <li>• FDA approved</li> <li>• Approved for general use in patients over 22 years of age</li> <li>• Approved for reconstructive breast surgery at any age</li> <li>• More cohesive feeling resembling a natural breast</li> <li>• Three shape: moderate, moderate plus and high profile</li> <li>• Available in textured or smooth surface</li> <li>• May ripple less</li> </ul>	<ul style="list-style-type: none"> <li>• FDA approved</li> <li>• Breast augmentation patients 18 years of age</li> <li>• Approved for reconstructive breast surgery at any age</li> <li>• Flexible volume size that can be adjusted during surgery</li> <li>• Saline is firmer</li> <li>• Three shape: moderate, moderate plus and high profile</li> <li>• Available in textured or smooth surface</li> <li>• May rippled more than silicone</li> </ul>

**Table 1.3** Comparison table between saline- and silicone breast implant

**Ref.** Stevens WG, Pacella SJ, Gear AJ, Freeman ME, McWhorter C, Tenenbaum MJ, et al. Clinical experience with a fourth-generation textured silicone gel breast implant: a review of 1012 Mentor MemoryGel breast implants. *Aesthetic Surgery Journal*. 2008;28(6):642-7.

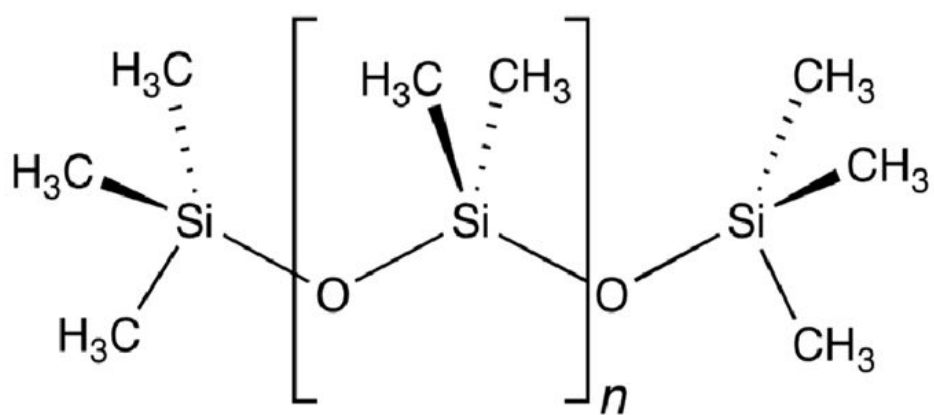


**Figure 1.5** Molecular structure of polydimethylsiloxane (PDMS) consisting of silicone implant

*Ref. <http://commons.wikimedia.org/wiki/File:Pdms.png>*

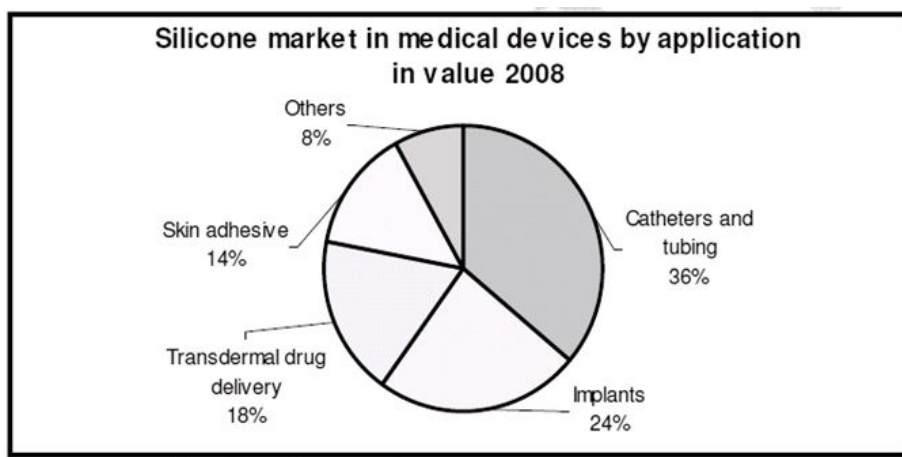


**Figure 1.6** US silicone market report in medical devices by application in 2008

*Ref. <http://www.marketsandmarkets.com>*

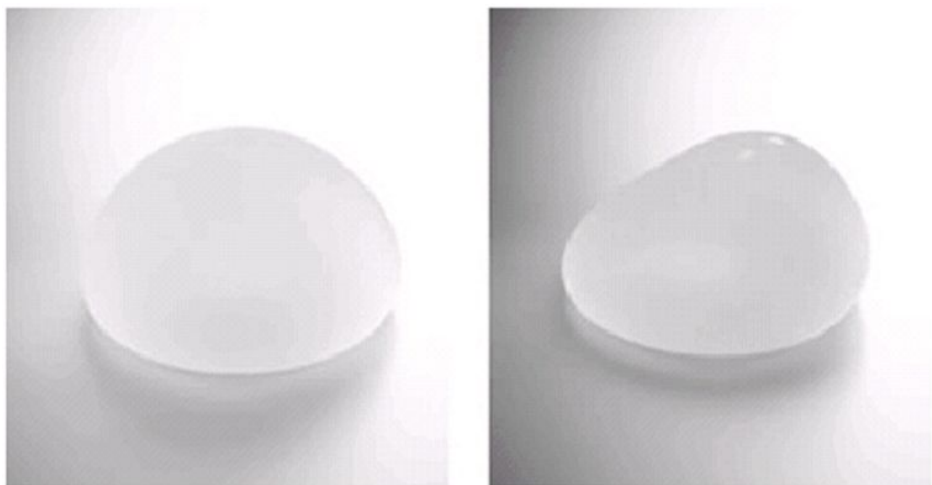


**Figure 1.7** Optical images of various silicone implants in clinical use

*Ref. <http://lakecharlesobgyn.com>*

### 1.3.1 Drawbacks of Silicone Implants

Silicone implants have been widely used throughout the world with the purpose of breast reconstruction and augmentation for more than four decades(19). However, there are still growing concern about the safety of the silicone implants, with regard to severe local complications such as capsular contracture, gel bleed, infection or implant rupture(22). Among them, the capsular contracture that results from pathological fibrosis is one of the most unfavorable complications with a reported incidence of 1.3–50 % in patients undergoing breast implant surgery(23) (Table 1.4). Capsular contracture is accepted as a response of the inflammatory reaction against foreign materials in the human body (Figure 1.8) (24). The capsular contracture leads to tighten and squeeze the silicone implant by the formation of tightly-woven collagen fibers to isolate the silicone implants from the human body, thereby resulting in being very painful and discomforting. The degree of an incidence of capsular contracture is graded using the four “Baker Grade”(22):

- Grade I — the breast is normally soft and appears natural in size and shape
- Grade II — the breast is a little firm, but appears normal
- Grade III — the breast is firm and appears abnormal
- Grade IV — the breast is hard, painful to the touch, and appears abnormal

There are two different types of surfaces of the silicone implants, today; one is the textured— and the other is the smooth surface (Figure 1.9)(21). A surface of the silicone implant is

usually known to interact directly with the breast tissue when the silicone implant is inserted. In this aspect, Wong et al. and Barnsley et al. demonstrated that the occurrence of capsular contracture on textured surfaces appeared about five-fold less as compared with smooth surfaces(20, 21). In other words, textured surface of the silicone implant is regarded to influence the formation of capsular contracture.

Reason	%
<b>Contracture</b>	<b>55.6</b>
<b>Size change</b>	<b>21.8</b>
<b>Malposition</b>	<b>8.2</b>
<b>Waviness</b>	<b>4.3</b>
<b>Deflation</b>	<b>4.1</b>
<b>Infection</b>	<b>2.7</b>
<b>Ruptured gel</b>	<b>1.6</b>
<b>Palpability</b>	<b>0.8</b>
<b>anxiety</b>	<b>0.4</b>

**Table 1.4** Incidence rate of various complications related to silicone implants

**Ref.** Handel N, Cordray T, Gutierrez J, Jensen JA. A long-term study of outcomes, complications, and patient satisfaction with breast implants. *Plastic and reconstructive surgery*. 2006;117(3):757-67.

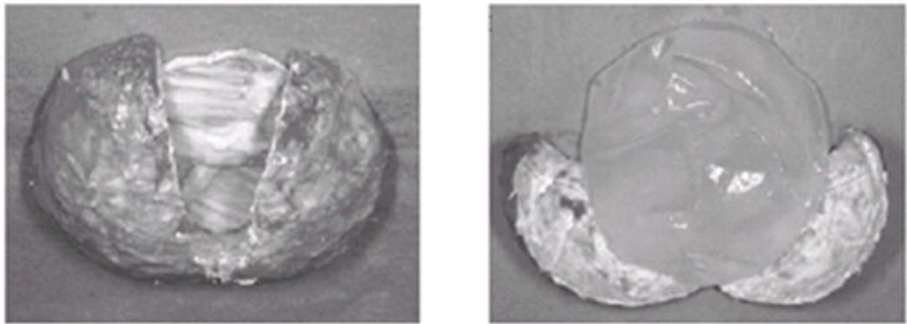


**Fig. 1.8** Optical images of capsular contracture formed around the silicone implants

**Ref.** <http://www.labseed.com>

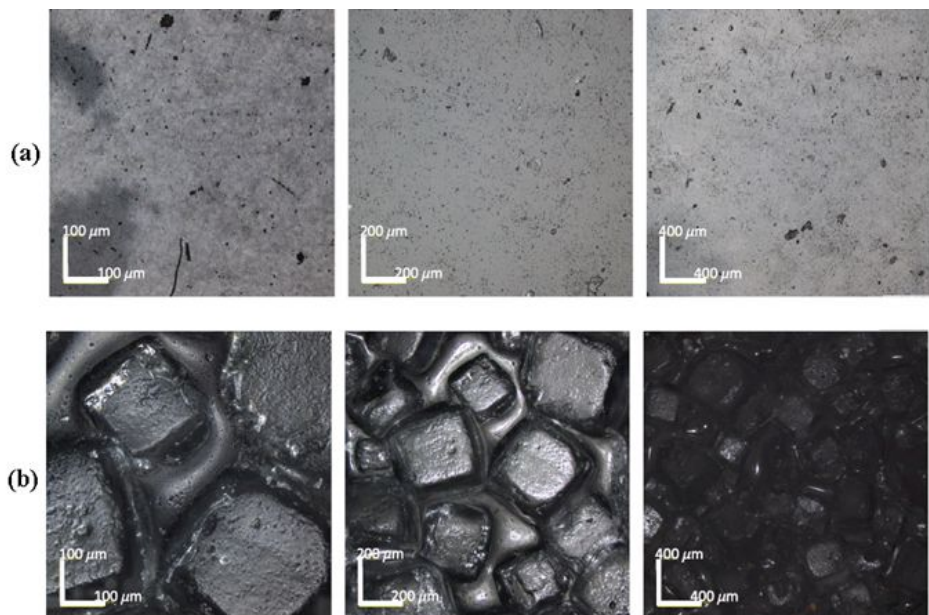


**Fig. 1.9** (a) Smooth surface showing a geographical surface with rock formations and small pins and (b) textured surface depicting a granular surface pitted with cuboid shaped wells

*Ref. Valencia-Lazcano AA, Alonso-Rasgado T, Bayat A. Physico-chemical characteristics of coated silicone textured versus smooth breast implants differentially influence breast-derived fibroblast morphology and behaviour. Journal of the mechanical behavior of biomedical materials. 2014;40:140-55.*

## 1.4 Research Purpose

The major purpose of the dissertation is to develop customized surface coating technologies in order to solve a variety of drawbacks that have been not fully resolved in implantable medical devices such as bone fixation systems and silicone implants.

The critical problems related to the bone fixation systems can be broadly described by lack of therapeutic functionality and rapid corrosion rate in biological fluid environment. Additionally, the serious drawback associated with silicone implants is the capsular contracture induced by the formation of fibrous capsule around silicone implants due to foreign body reaction. To solve these problems, with biodegradable various polymers, the optimized coating technologies on the surface of the implantable devices, *i.e.*, bone fixation systems and silicone implants, are introduced to add the therapeutic functionality, maintaining an intact functionality of the medical devices.

In Chapter 2, we present various surface coating technologies such as dip coating, spray coating and drop casting which were applied in this work. Then, a variety of biopolymers as a coating material is introduced, focused on their physical, chemical properties and biocompatibility, biodegradability and biomedical applications. Among these biopolymers, the biopolymers (PCL, PLGA and chitosan) used as coating materials are described in detail.

In Chapter 3, we employ a biodegradable polymer,

polycaprolactone (PCL) coating on the surface of magnesium (Mg) bone fixation system to prevent the rapid corrosion rate of Mg, hence maintaining the sufficient mechanical strength of Mg until bone healing is complete. Moreover, we suggest that the corrosion rate of Mg can be controlled depending on the coating thickness.

In Chapter 4, we present bioabsorbable bone fixation systems enabled with local, sustained delivery of alendronate for bone regeneration. To solve the failure of the bone fixation systems associated with osteoporotic bone fractures, we coated the bone plates with azidobenzoic acid-modified chitosan (Az-CH) loaded with alendronate which is known to treat osteoporosis. Then, the Az-CH coating with drug was photocrosslinked by UV irradiation to give a covalent bonding between the bone plate and Az-CH coating.

In Chapter 5, we aim to develop the silicone implants enabled with local, sustained exposure of tranilast, as an inhibitor of TGF- $\beta$  to reduce the fibrous capsule around the silicone implants. To this end, we prepared silicone implants that were able to release tranilast for 5 days or 15 days in a sustained manner. We performed histologic and immunohistochemical analyses for 12 weeks after the implantation of the implants in living rats.

# Chapter 2

## Surface Coating of Implantable Medical Devices

### 2.1 Surface Coating

In order to enhance the physical or chemical properties of materials in medical devices as well as to give a better interaction of the medical devices with the biological system around them, polymeric surface coatings are often applied in biomedical engineering field(25). In many studies, a variety of the substrates are coated with polymeric films through physical interactions. Moreover, to achieve better adhesion between

polymeric coating and substrate, chemical coating technologies have been significantly developed through covalent bonding or ionic interaction(25). To implement these, various coating methods have been introduced for a long time, for example, dip coating, spray coating, spin coating and drop casting.

### **2.1.1 Dip coating**

Dip coating usually means that the substrate is dipped into the solution and then withdrawn at a controlled speed (Figure 2.1)(26). The advantages of dip coating are quite good uniformity, very thin layers and large area coverage(27). However, dip coating have limitations such as non-waste of materials, –time consuming and –double side coverage. Above all, thickness of coating film can be controlled by the balance of forces at the liquid–substrate interface through Landau and Levich equation (Figure 2.2). Based on this equation, thickness of coating film can be sufficiently programmed by viscosity of coating solution and withdraw speed. In this reason, as a concentration of polymer dissolved in solvent increases, coating thickness increases.

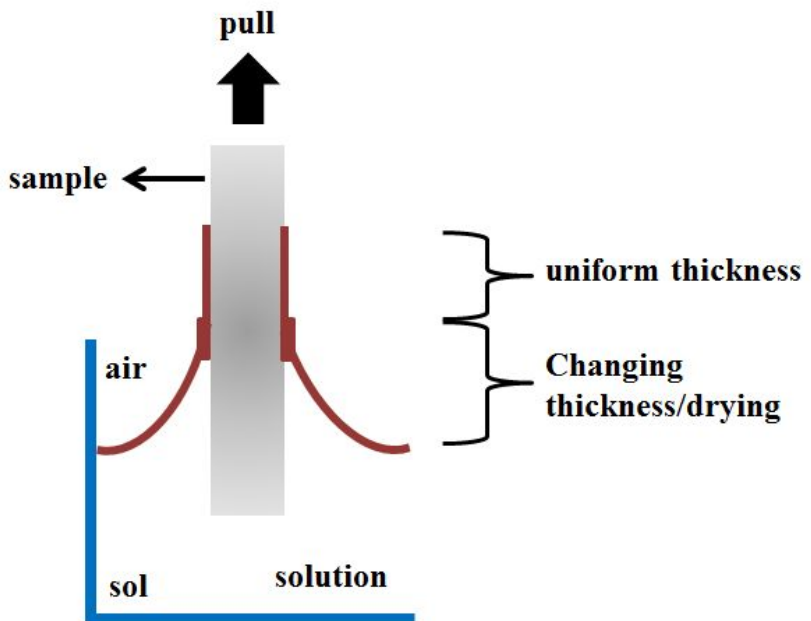


**Fig. 2.1** Schematic illustration of dip coating

*Ref. C. Brinker, G. Frye, A. Hurd, C. Ashley, Fundamentals of sol-gel dip coating, Thin Solid Films, 201 (1991) 97-108.*

Landau and Levich equation:

$$H = \frac{0.94(\mu v)^{2/3}}{\gamma^{1/6}(\rho g)^{1/2}}$$

$\mu$ = fluid viscosity     $v$  = withdrawal speed

$\rho$ = fluid density     $g$  = gravitational acceleration

$\gamma$ = surface tension (liquid-air)

**Fig. 2.2** Landau and Levich equation for estimating thickness (H) of coating film

*Ref. C. Brinker, G. Frye, A. Hurd, C. Ashley, Fundamentals of sol-gel dip coating, Thin Solid Films, 201 (1991) 97-108.*

### **2.1.2 Spray coating**

Spray coating means that a substrate is hit by a vaporized solution flux (Figure 2.3). In particular, the film morphology or thickness can be controlled by air pressure, solution viscosity, solvent properties including evaporation rate, gun tip geometry such as diameter of gun tip nozzle, distance between nozzle and substrate. Advantages of spray coating include adjustable layer thickness, large area coverage, independence on substrate topology while a disadvantage of that is relatively very poor homogeneity of the coating film. Spray coating can also be applied to screen printing meaning that the solution containing the active material is squeezed through a screen mask onto the substrate surface (Figure 2.4).

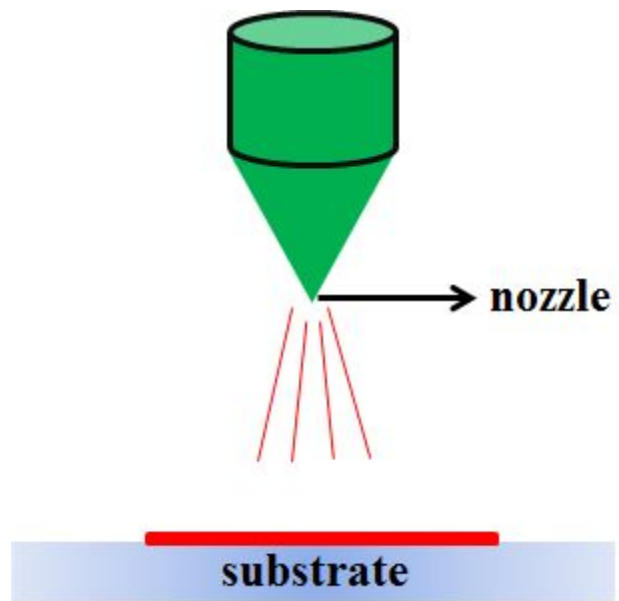


**Fig. 2.3** Schematic illustration of spray coating

*Ref. H. Hansen, Method for spray-coating medical devices, in, Google Patents, 2003.*

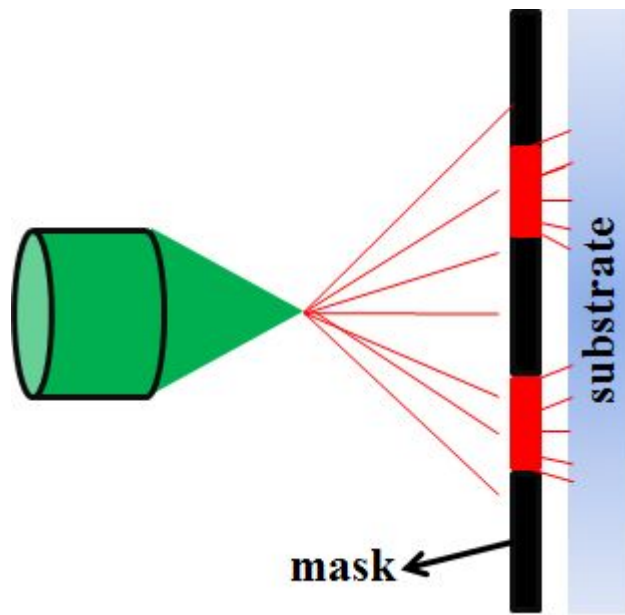


**Fig. 2.4** Schematic illustration of screen printing using spray coating

*Ref. H. Hansen, Method for spray-coating medical devices, in, Google Patents, 2003.*

### **2.1.3 Drop Casting**

Drop casting is to drop a solution onto a substrate and to evaporate solvent spontaneously (Figure 2.5). Particularly, thickness of coating film is proportional to solution concentration. Advantages of drop casting are very simple process and non-waste of material while disadvantages of that are that thickness of coating film is relative is too thick to precisely control and large area coverage is difficulty and uniformity of coating film is not that good. In generally, when an evaporation time of solvents is long, heating of the substrate to speed up the evaporation process is required, thereby enhanced morphology of coating film.

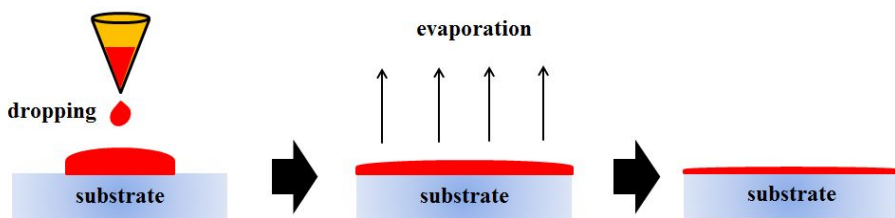


**Fig. 2.5** Schematic illustration of drop casting

**Ref.** A. Farag, I. Yahia, Structural, absorption and optical dispersion characteristics of rhodamine B thin films prepared by drop casting technique, *Optics Communications*, 283 (2010) 4310-4317.

## 2.2 Biopolymers as a Coating Material

The optimized biopolymers as a coating material must be properly applied to give the additional functionalities such drug delivery system, anti-bacterial effect, anti-corrosion or enhanced biocompatibility on the surface of medical devices(25). In this aspect, it is very critical to select and design biopolymers because of their intact diversity, thereby needing a thorough understanding of the surface and bulk properties of the biopolymers which are able to give mechanical, chemical, interfacial or biological functionality. In detail, water permeability and hydrophobicity of biopolymers strongly influence the water sorption ability, which in turn determines the rate of hydrolytic degradation and swelling. Elastic modulus, ultimate yield strength, toughness or ductility of biopolymers also govern mechanical properties like flexibility and biodurability. Considering these properties, biopolymers should properly be selected based on the purpose of the coating. For example, when the bioabsorbable medical devices are coated with biodegradable polymers to reduce corrosion or erosion in biological fluid environment, biopolymers with even slower degradation rate in biological environment must be of important required(28).

First, biopolymers are accepted as one of polymers which function in contact with living cells or tissues with no complications and adverse side effects. Biopolymers can be generally divided into two parts; Natural and synthetic

polymers(29, 30).

Natural polymers derived from natural sources such as protein, enzymes, polysaccharides and polynucleotides are of great interested in the biomedical engineering field (Table 2.1)(31). Their advantages are biodegradable, non-toxic, -inflammatory, mechanical property similar to the tissue, encouraging of cell attachment and growth. However, there are a few disadvantages including poor reproducibility owing to difficulties in purification and difficulties to obtain the natural sources. In these reasons, synthetic polymers, for example, poly(lactic acid) (PLA), poly(glycolic acid) (PGA), poly(lactic-co-glycolic acid) (PLGA), polycaprolactone, have been developed and widely available in biomedical engineering field (Table 2.2)(32, 33). Moreover, biopolymers can be classified into non-biodegradable and biodegradable polymers in biological fluid environment(34). Biodegradation usually occurs by a variety of factors such as enzyme, microbial origin or water (Table 2.3).

	Polymer	Incidence	Physical function
Proteins	Silk	Synthesized by arthropods	Protective cocoon
	Keratin	Hair	Thermal insulation
	Collagen	Connective tissues	Mechanical support
	Gelatin	Partly amorphous collagen	Industrial product
	Fibrinogen	Blood	Blood clotting
	Elastin	Neck ligament	Mechanical support
	Actin	Muscle	Contraction
	Myosin	Muscle	Contraction
Polysaccharides	Cellulose	Plants	Mechanical support
	Amylose	Plants	Energy reservoir
	Dextran	Synthesized by bacteria	Matrix for growth of organism
	Chitin	Insects	Provides shape and form
	Glycosaminoglycans	Connective tissues	Contributes to mechanical support
polynucleotides	Deoxyribonucleic acids (DNA)	Cell nucleus	Direct protein biosynthesis
	Ribonucleic acid(RNA)	Cell nucleus	Direct protein biosynthesis

**Table. 2.1** List of representative natural polymers

*Ref. Uhrich KE, Cannizzaro SM, Langer RS, Shakesheff KM. Polymeric systems for controlled drug release. Chemical reviews. 1999;99(11):3181-98.*

Classification	Polymer
Biodegradable polyesters	Poly(lactic acid), poly(glycolic acid), poly(hydroxy butyrate), polycaprolactone, poly( $\beta$ -malic acid), poly(dioxanones)
Polyanhydrides	Poly(sebacic acid), poly(adipic acid), poly(terphthalic acid) and various copolymers
Polyamides	Poly(imino carbonates), polyamino acids
Phosphorous-based polymers	Polyphosphates, polyphosphonates, polyphophazenes
Others	Poly(cyano acrylates), polyurethanes, polyortho esters
Cellulose derivatives	Carboxymethyl cellulose, ethyl cellulose, cellulose acetate, cellulose acetate propionate, hydroxypropyl methyl cellulose
Silicones	Polydimethylsiloxane, colloidal silica
Acrylic polymers	polymethacrylates, poly hydro(ethylmethacrylate)
others	Polyvinyl pyrrolidone, ethyl vinyl acetate, poloxamers

**Table. 2.2** List of representative synthetic polymers

**Ref.** Soppimath KS, Aminabhavi TM, Kulkarni AR, Rudzinski WE. *Biodegradable polymeric nanoparticles as drug delivery devices*. *Journal of Controlled Release*. 2001;70(1):1-20.

**Ref.** Makadia HK, Siegel SJ. *Poly lactic-co-glycolic acid (PLGA) as biodegradable controlled drug delivery carrier*. *Polymers*. 2011;3(3):1377-97.

<b>Factors influencing biodegradation of polymers</b>
<b>Chemical structure and composition</b>
<b>Physico-chemical factors (ion exchange, ionic strength, pH)</b>
<b>Physical factors (shape, size, chain-defects)</b>
<b>Morphology (amorphous, semicrystalline, crystalline, microstructure, residual stress)</b>
<b>Mechanism of degradation (enzymatic, hydrolysis, microbial)</b>
<b>Molecular weight distribution</b>
<b>Processing conditions and sterilization process</b>
<b>Annealing and storage history</b>
<b>Route of administration and site of action</b>

**Table. 2.3** Various factors influencing biodegradation of polymers

*Ref. Langer R, Chasin M. Biodegradable polymers as drug delivery systems. Marcel Dekker, New York; 1990.*

### **2.2.1 Polycaprolactone (PCL) and Poly(Lactic–co–glycolic acid) (PLGA) as a synthetic polymer**

As one of biodegradable aliphatic polyesters, polycaprolactone (PCL) has been significantly used as biomaterials of the matrix of drug delivery particles and the scaffold in tissue engineering due to its excellent biocompatibility and biodegradability (Figure 2.6)(30). PCL is approved by FDA for human clinical applications because of such good biocompatibility. It has inherit physical properties such as a low melting temperature (63 °C) and glass–transition temperature (−60 °C) (Table 2.4). Above all, the most critical property of PCL is that its degradation rate is the slowest as compared with other biodegradable polymers, showing that its degradation time is at least over 24 months(35). Herein, polymer degradation is defined as “the chemical reaction inducing a cleavage of main–chain bonds, which in turn result in short oligomers, monomers and very low molecular weight degradation by– products(36). Especially, PCL can be degraded by a hydrolytic mechanism as well as a micro–organism. Due to its relatively very low degradation rate, to prevent corrosion or erosion of medical devices in biological fluid environment, polycaprolactone has attracted significant attention as a diffusion barrier to water. For instance, as a bioabsorabable metal,

magnesium(Mg) and its alloys have been applied to orthopedic implants(28). However, owing to a very rapid corrosion rate of magnesium, magnesium-based orthopedic implants cannot sufficiently maintain the mechanical strength until bone healing is complete, thereby limited in clinical use. To overcome such problem, many studies have been conducted through biodegradable polymer coating on surface of magnesium-based orthopedic implants(26, 35). Herein, polycaprolactone is accepted as the most excellent candidate among any other biodegradable polymers.

Biodegradable poly(lactic-co-glycolic acid)(PLGA) is also one of the aliphatic polyesters and the copolymer of the two monomers, *i.e.*, lactic acid and glycolic acid (Figure 2.7) (37). In general, the name of PLGA usually refers to the ratios of the two monomers used. For instance, PLGA 40:60 is a copolymer of 40 % lactic acid and 60 % glycolic acid. Like PCL, PLGA copolymers are one of approved synthetic polymers approved by FDA for human clinical applications because of their good biocompatibility(33). They can be also degraded through hydrolysis of the ester bonds into lactic and glycolic acid, which are excreted by normal metabolic pathways, thereby showing non-toxic byproducts. Moreover, PLGA can be easily fabricated

and processed and their physical, mechanical, chemical properties can be sufficiently controlled by varying the ratio of the co-monomers(30, 38). Its degradation time can be also programmed by controlling the ratio of the co-monomers (Table 2.5 and 2.6). Due to its versatility, PLGA has been commonly employed for development of biomedical devices in clinical use such as bioabosrabable bone fixation systems, bioabsorabable surgical sutures and drug delivery systems(39, 40). Particularly, PLGA-based microspheres have widely developed and marketed in clinical use. This can be ascribed by the fact that drug release profiles can be controlled by the biodegradability and hydrolysis of PLGA, followed by a slow diffusion-controlled release of drug. In this reasons, there are currently an increasing number of PLGA-based microsphere products for small/large molecule, proteins and vaccines on the market. Table 2.7 shows FDA-approved microspheres derived from PLGA. Risperdal Consta from Jansen is known to be one of the most successful products with sales of more than \$ 1.5 billion in 2011. This is developed to treat schizophrenia, enabling a sustainable release of risperidone for 2 weeks.

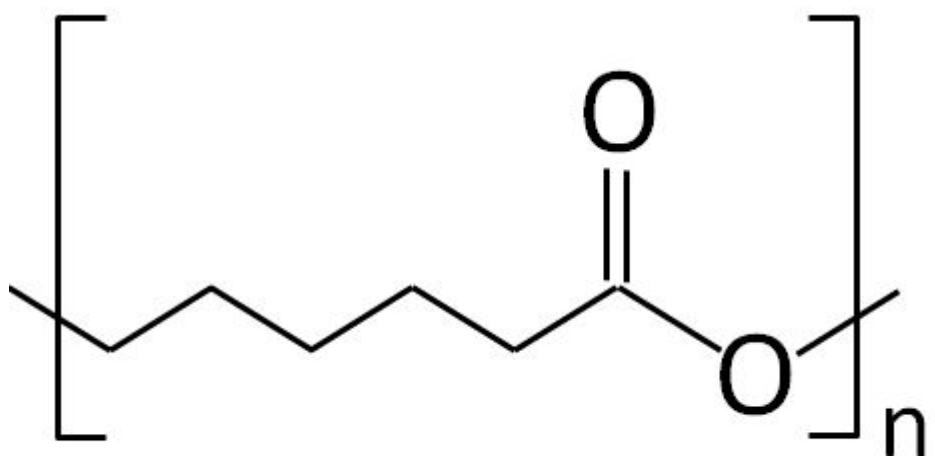


**Fig. 2.6** Molecular structure of polycaprolactone (PCL)  
Ref. <http://commons.wikimedia.org>

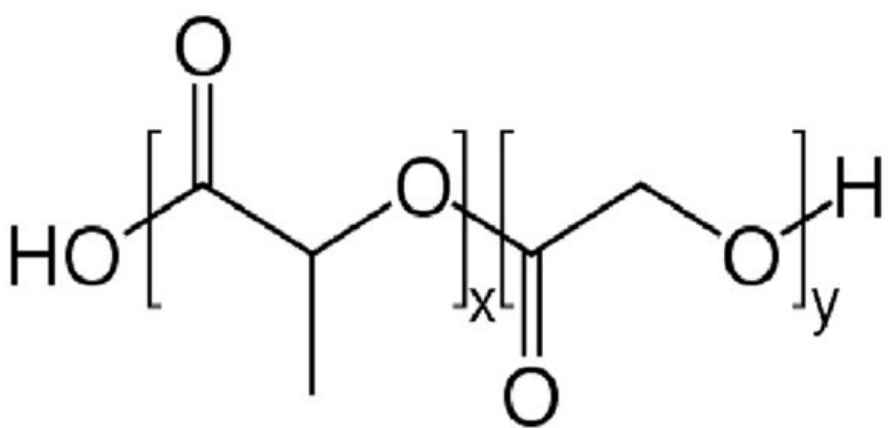


**Fig. 2.7** Molecular structure of poly(lactic-co-glycolic acid). x = number of units of lactic acid; y = number of units of glycolic acid.

*Ref. <http://commons.wikimedia.org>*

Some important physical properties of polycaprolactone	
1% Secant modulus (psi)	50,000
Elongation (%)	-759
Yield stress (psi)	1,600
Tensile strength (psi)	3500
Melting point (°C)	63
Glass transition temperature Partially crystalline (°C) Amorphous (°C)	-60 -71
Density (g/cm <sup>3</sup> ) 20 °C	1.149

**Table 2.4** Physical properties of polycaprolactone

*Ref. M.A. Woodruff, D.W. Hutmacher, The return of a forgotten polymer—polycaprolactone in the 21st century, Progress in Polymer Science, 35 (2010) 1217-1256.*

Polymer	Melting point (°C)	Glass-transition Temp (°C)	Modulus (Gpa)	Tensile Strength (Mpa)	Elongation at break (%)	Degradation time (months)
PGA	225-230	35-40	7.0	60-80	30	6-12
PLLA	173-178	60-65	2.7	60-70	3	>24
PDLLA	Amorphous	55-60	1.9	2	N/A	12-16
PCL	58-63	60-65	0.4	20-25	800-1000	>24

**Table 2.5** Various features of biodegradable polymers

**Ref:** Medical plastics and biomaterials magazine, march, 1998

Medical device manufacturing & technology 2005

The biomedical engineering handbook, Joseph D, Bronzino, Ed. CRC

Press in Cooperation with IEEE Press, Boca Raton, FL, 1995

Science, Vol. 297 p, 803 (2002)

Polymer	Degradation time (months)
<b>PGA</b>	<b>6-12</b>
<b>PLLA</b>	<b>&gt;24</b>
<b>85/15 PLGA</b>	<b>5-6</b>
<b>75/25 PLGA</b>	<b>4-5</b>
<b>65/35 PLGA</b>	<b>3-4</b>
<b>50/50 PLGA</b>	<b>1-2</b>

**Table 2.6** Various degradation times of PLGA depending on the ration of co-monomers, i.e., lactic acid and glycolic acid

*Ref.* Y. Wang, *Implantable medical devices fabricated from block copolymers*, in, *Google Patents*, 2011.

Trade name	Drug	Company	Release period	Application
Lupron Depot	Leuprolein acetate	Abbott	1,3 or 4 months	Prostate cancer
Nutropin Depot	Recombinant human growth hormone	Genentach-Alkomoe	1or 2 months	Prostate cancer
Zoladex	Goserelin acetate	Astra Zeneca	1 or 3 months	Prostate cancer
Frostap	Leuprorelin acetate	Ipen	1 month	Prostate cancer
Sandostatin LAR Uepot	Octrotide acetate	Novartis	1 month	GH suppression anti-cancer
Vivitrol	Nnaltrexone	Alkemes	1 month	Alcohol
Posilac	Recombinant bovine ecmatropin	Cli Lilly	2 weeks	Prostate cancer
Aresin	minocycline	Orpharma	2 weeks	Periodential dissease

**Table 2.7** Marketed products produced with PLGA, biodegradable polymer

*Ref.* <http://www.samedanltd.com>

## 2.2.2 Chitosan as a natural polymer

Chitosan is originated from partial deacetylation of chitin from crustacean shells (Figure 2.8) and is a polysaccharide consisting of glucosamine and N-acetylglucosamine(41). The term chitosan is used to explain a series of chitosan polymers with different molecular weights (50 kDa ~ 2000 kDa) and degree of deacetylation (40 % ~ 99.8 %)(Table 2.8). The solubility of chitosan is dependent on the degree of deacetylation. That is, chitosan with a low degree of deacetylation (40 %) is known to be soluble up to pH 9 while that with a high degree of deacetylation (85 %) soluble up to pH 6.5. Once the chitosan is dissolved, the amine groups of the chitosan are protonated and the resulting chitosan solution is positively charged.

Until now, chitosan has been significantly employed for biomedical applications such as surgical sutures, dental implants, artificial skin and drug delivery carriers (Table 2.9 and 2.10)(42). This is because chitosan has good bioadhesive, very excellent biocompatibility, film forming, hydrolysis by lyzosyme, wound healing properties and antibacterial effect. Especially, chitosan has been extremely examined in the pharmaceutical field for its potential in controlled release drug systems(Table

2.11) (43). This is due to the viscosity gel layer surrounding the drug particles, degree of crosslinking of chitosan, swelling capacity or bioadhesive(42). In addition, chitosan has been often used as coating material in drug delivery systems since it has an excellent good film forming properties. In other words, as a coating material, chitosan has a variety of advantages including controlled release of drug for a prolonged period of time(41, 43). Lastly, chitosan has mucoadhesive properties, which lead to formulate the bioadhesive dosage forms that can be delivered to oculalr, nasal, buccal and gastro-enteric route. This can be ascribed by the fact that chitosan is protonated in an acid solution and the resulting solution is positively charged, which can bind strongly to negatively charged surface such as cell surface and mucosa. This mechanism can eventually enhance the residence time of drugs on cells and tissues, thereby resulting in sustained release of drug(44).

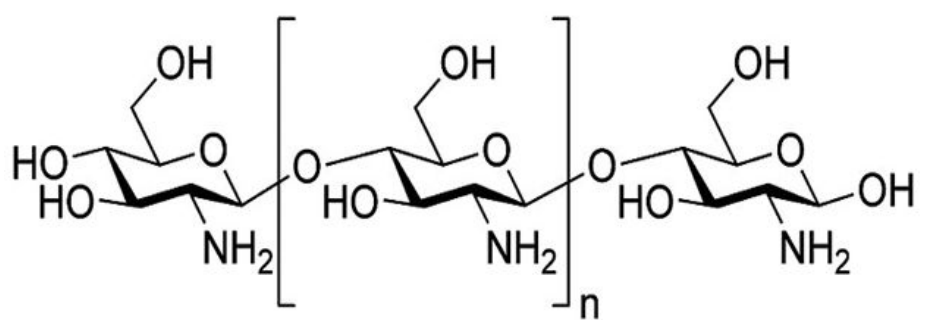


**Fig 2.8** Molecular structure of chitosan

*Ref. <http://de.wikipedia.org/wiki/Chitosan>*

Parameters	Description
<b>Appearance(powder or flake)</b>	<b>White or yellow</b>
<b>Particle size</b>	<b>Less than 30 <math>\mu\text{m}</math></b>
<b>Viscosity(1% solution/1% acid)</b>	<b>Less than 5 cps</b>
<b>Density</b>	<b>Between 1.35 to 1.40 g/cm<sup>3</sup></b>
<b>Molecular weight</b>	<b>50,000 to 200,000 Da</b>
<b>pH</b>	<b>6.5 to 7.5</b>
<b>Moisture content</b>	<b>More than 10 %</b>
<b>Ash value</b>	<b>More than 2 %</b>
<b>Matter insoluble in water</b>	<b>0.5 %</b>
<b>Degree of deacetylation</b>	<b>66 % to 99.8 %</b>
<b>Heavy metal (Pb)</b>	<b>Less than 10 ppm</b>
<b>Heavy metal (As)</b>	<b>Less than 10 ppm</b>
<b>Protein content</b>	<b>Less than 0.3 %</b>
<b>Loss on drying</b>	<b>Less than 10 %</b>
<b>Glass transition temperature</b>	<b>203 °C</b>

**Table 2.8 Specification of chitosan**

*Ref. Rinaudo M. Chitin and chitosan: properties and applications. Progress in polymer science. 2006;31(7):603-32.*

Potential biomedical applications	Principal characteristics
Surgical sutures	Biocompatible
Dental implants	Biodegradable
Artificial skin	Renewable
Rebuilding of bone	Film forming
Corneal contact lenses	Hydrating agent
Time release drugs for animals and humans	Nontoxic, biological tolerance
Encapsulating material	Hydrolyzed by lysozyme Wound healing properties Efficient against bacteria, viruses, fungi

**Table 2.9** Principal properties of chitosan in relation to its use in biomedical applications

**Ref.** Bhattacharai N, Gunn J, Zhang M. Chitosan-based hydrogels for controlled, localized drug delivery. *Advanced drug delivery reviews*. 2010;62(1):83-99.

	Wound & Hemostats	Biosurgery	Scaffold & Cell therapy	Vaccine delivery	Drug delivery	ophtalmology
Segments of application	Surgical wound, traumatic wound, burns, chronic wound	Cardiovascular, neurology, maxillo facial, general surgery, digestive, orthopedic, urological	Scaffold for cell culture, cell delivery, cell encapsulation, tissue engineering	Parenteral, transdermal, oral, sublingual, nasal, pulmonary	Buccal, sublingual, nasal, pulmonary, oral, ocular, vaginal	Topical, intravitreal, subconjunctival
systems	Wound dressing, hydrophilic, hydrogel, interactive wound dressing, burn dressing, sponges, films foam	Films, sponge, sealant, glue, fibres, tubes	Porous scaffolds, porous films, thermosetting gels, tubes	Adjuvants, hydrogels, solutions, microparticle, nanoparticle, preservation	Microparticle, nanoparticle, hydrogel, film, dressing, tablets	Viscoelastic solutions, nanoparticle, inserts

**Table 2.10** Various biomedical applications of chitosan

*Ref.* Ravi Kumar MN. *A review of chitin and chitosan applications. Reactive and functional polymers.* 2000;46(1):1-27.

<b>Types of system</b>	<b>Method of preparation</b>	<b>Drug</b>
Tablets	Matrix	5-ASA, diclofenac sodium, theophylline, mesalamine
	Coating	Propranolol HCl
Capsules	Capsule shell	Insulin
Microshperes/ microparticles	Emulsion cross-linking	Gentamicin sulphate, hemoglobin, diclofenac
	Coacervation/precipitation	Propranolol HCl
	Spray-drying	Cimetidine, bovine serum albumin
	Ionic gelation	Bovine serum albumin
	Reverse micellar method	Doxorubicin
Beads	Coacervation/precipitation	Bovine serum albumin
Films	Solution casting	Ofloxacin, paclitaxel
Gel	Cross-linking	5-fluorouracil

**Table 2.11** List of chitosan based formulations prepared by different methods

**Ref.** Ravi Kumar MN. *A review of chitin and chitosan applications. Reactive and functional polymers.* 2000;46(1):1-27.

# Chapter 3

## Polycaprolactone Coating with Varying Thicknesses for Controlled Corrosion of Magnesium

### 3.1 Introduction

Biocompatible metals, such as titanium alloy, stainless steel and cobalt–chromium based alloy, have been widely used for orthopedic fixation devices, such as bone screws and plates, because of their relatively high mechanical strength and fracture toughness (16, 45). However, a secondary surgery is usually needed to remove such metallic implants after complete bone healing since they are not degradable in the body, thereby possibly causing low patients' compliance(16). To overcome

those problems, the orthopedic implants composed of biodegradable polymers, such as poly(lactide-co-glycolide) (PLGA) and poly(L-lactide) (PLLA), have been developed and already approved in clinical use (1, 29). However, such polymeric implants are limited in their applications mostly due to considerably lower mechanical strength (46).

To meet the needs in both mechanical strength and biodegradability, magnesium (Mg) and its alloys have attracted a great deal of interest for the use in orthopedic fixation devices (15, 36, 47). The mechanical properties of Mg, such as the density (1.74 g/cm<sup>3</sup>), Young's modulus (42 GPa) and ultimate yield strength (35 ~ 283 MPa), are known to be similar to those of natural bone, as compared with the other metals commonly used for orthopedic devices (48, 49). On the other hand, the implants made of titanium and its alloy, stainless steel or Co-Cr alloys, are reported to often induce serious stress shielding, which is caused by a big difference in mechanical property between natural bone and the metals, eventually leading to implant loosening (16). As for biodegradation, the Mg-based implant is corroded in biological fluid, releasing Mg ions, which are common metabolites already present in the body and also naturally available in bone tissue (50, 51). The Mg ions,

therefore, are known to be readily excreted by the urine system (52).

However, Mg alone is extremely limited in orthopedic applications due to its high corrosion rate, resulting in rapid loss of mechanical strength before complete bone healing (16, 53).

This rapid corrosion of Mg also leads to high accumulation of hydrogen gas generated near the implantation site. This forms a hydrogen gas pocket, which often causes necrosis of tissues and separation between the implant and tissues, leading to delay in bone healing (53, 54). Therefore, to be applicable, control over the corrosion rate of Mg is needed to retain the mechanical strength of the Mg implant during the period of bone healing, as well as allowing the implant to be eventually fully degraded.

A variety of methods have been suggested to control the corrosion rate of Mg. The alloying elements, such as zirconium and cerium, when added to magnesium, could delay the corrosion of Mg to some extent, which, however, could potentially cause toxicity by releasing the alloying elements during corrosion (55, 56). The surface of Mg or its alloys have been coated with the materials, such as chitosan (57), stearic acid (58) and many different biodegradable polymers (59, 60). These polymeric coatings could serve as a permeation barrier of biological fluid,

thereby hindering Mg corrosion while being eventually degraded into non-toxic products. However, to our knowledge, the coatings prepared in the previous studies were mostly not reproducible to give an inhomogeneous permeation barrier of biological fluid throughout the Mg surface and thus, those coatings did not seem to precisely control Mg corrosion.

In this work, in order to delay corrosion, we pursued to prevent water permeation to the Mg surface simply by increasing the coating thickness of biodegradable polymer, polycaprolactone (PCL). PCL would serve as a good permeation barrier due to its hydrophobicity and slower degradation in biological fluid than Mg (60). We also pursued to produce a reproducible, homogeneous coating of PCL on the Mg surface with an automated apparatus designed to follow the widely-accepted dip-coating method (see Figure S1 in the Supplementary Information) (26, 27). Thus, a coin-shaped Mg sample was dipped into the polymer solution and dried in air in the determined period of time, giving a single set of dipping process, which were simply repeated, giving multiple sets of dipping and drying, to increase the coating thickness. In this work, we tried to average out a pore or defect formation in the coating in a reproducible manner, which, therefore, would provide a predictable water permeation profile,

thereby a detailed study on the effect of coating thickness on Mg corrosion(26).

In this work, we examined the coating on Mg samples with scanning electron microscopy (SEM). To study the effect of coating thickness on Mg corrosion, the in vitro immersion test was performed in Hank' s solution (61). We examined the amount of hydrogen gas and Mg ions generated by corrosion with time and also monitored the surface morphology and elemental composition with the samples extracted from Hank' s solution during corrosion.

## 3.2 Materials and Methods

### 3.2.1 Materials

Polycaprolactone (PCL; average MW = 10,000 ~ 14,000), Hank' s solution (Table 1) and chloroform were purchased from Sigma (MO, USA). The coins of Mg, 10 mm in diameter and 1.5 mm in thickness, were prepared, as previously reported (61). Briefly, commercial pure Mg ingot was melted and casted into the mold, which was then cooled down to give a rod, 10 mm in diameter.

The resulting rod was then cut into coins, 1.5 mm in thickness, which possessed the compositions of 99.97% Mg and some impurities (0.0214% Fe, 0.0027% Ni, 0.0053 Al and 0.0036% Mn).

### 3.2.2 Sample Preparation and Coating Process

Before coating, the coins were each polished with SiC papers of 1000 grits and 2000 grits, which were then washed with distilled water and ethanol, using an ultrasonic cleaner (NXCS-1200, Kodo Technical Research, Korea), and dried at room temperature. A coin was then loaded into the home-made apparatus (see Figure 3.1 (a)), where the coin was dipped into 5% w/v PCL solution in chloroform for 5 s (see Figure 3.1 (b)) and extracted to the air for 60 s (see Figure 3.1 (c)), completing a single set of dipping process. We repeated this dipping set to 0, 1, 10 and 50 times to give NCM, 1DCM, 10DCM and 50DCM. The samples were then unloaded from the apparatus and dried in atmosphere for 24 h to remove the residual solvent. The Mg samples with a half of the surface area masked with Ideal 9144 Masking Tape were also coated under the same conditions stated above. After removing the tape, the height difference between

the non-masked and masked surfaces (i.e., the coated and noncoated surfaces, respectively) on the Mg sample could represent the coating thickness. More than three samples prepared under each of the coating conditions were examined for statistics.

### 3.2.3 Immersion Test

To examine the corrosion behavior of the coated Mg samples, we performed the immersion test, using a Hank's solution with the compositions listed in Table 3.1. As the representative data of the corrosion rate, we measured the volume of hydrogen gas generated from the Mg samples, as previously reported (Figure 3.2) (61). Briefly, the samples were each hung in an individual holder by nylon thread to be fully immersed in 500 ml of pH 7.4 Hanks' solution at 37 ° C. At schedule intervals, the volume of hydrogen gas collected at the end of the funnel was measured for 14 days, which was calibrated to give the volume per unit area exposed at the surface of the immersed Mg sample. Under the same experimental condition, we also extracted the immersion media on days 1, 7 and 14, where the amount of released Mg ions were measured, using an inductively-coupled

plasma emission spectrometry (ICP–AES). During the immersion test, 500 ml of Hanks' solution was fully replaced with fresh one every 24 h. More than three samples for each of the coating thicknesses were tested for statistics.

### 3.2.4 Characterization of PCL coating

The surface and thickness of the coating was examined with scanning electron microscopy (SEM; 7410F, Jeol, Japan). Before imaging, the PCL-coated samples were each placed on a SEM sample mount and sputter coated with platinum for 10 min (208HR, Cressington Scientific, England). The noncoated Mg sample (i.e., NCM) was imaged without further treatment. To examine the coating thickness, the samples with only a half of the surface coated (i.e., the coated samples with tape masking) were imaged from the side, where the height difference between the coated and noncoated surface was measured. We also analyzed the surface of the samples after immersion test. The change in elemental composition of the coating during corrosion was examined with Oxford INCAFETx3 energy dispersive spectroscopy (EDS) equipped with the SEM.

### 3.3 Results

#### 3.3.1 Coating Analysis

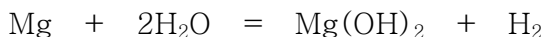
In this work, we coated the surface of Mg coins, 1.5 mm in height and 10 mm in diameter, with a biodegradable polymer, PCL and varied the coating thickness to examine its effect on Mg corrosion. To vary the thickness in a reproducible manner, the Mg samples were dip-coated using an automated apparatus under each of the fixed processing conditions (see Figure 3.1). As shown in Figure 3.3(a), the noncoated sample (i.e., NCM) exhibited a clean surface of Mg due to polishing. After coating with PCL, the surfaces became slightly rough, showing a number of pores, which were often observed with many different polymeric coatings incorporated with solvent evaporation (Figure 3.3 (b-d)) (62).

As we increased the number of dipping, the coating thickness also increased, as expected. The thicknesses of PCL coating were  $2.88 \pm 0.91 \mu\text{m}$ ,  $4.33 \pm 0.40 \mu\text{m}$  and  $13.31 \pm 0.36 \mu\text{m}$  with the numbers of dipping of 1, 10 and 50 times, respectively (i.e., 1DCM, 10DCM and 50DCM, respectively) (Table 3.2 and Figure 3.4). Under a dry condition, the coating appeared to

adhere well on the Mg surface. We also performed the EDS analysis on the surfaces of the noncoated and coated samples. As shown in Figure 3.5 (a), the surface of NCM was composed of Mg and O, indicating the formation of oxide layer on the surface of intact Mg after air contact. On the other hand, the coated samples exhibited the surface composed of C and O, i.e., the major elements in PCL, without the presence of Mg (Figure 3.5 (b-d)). This result implied that the Mg surface could be fully coated with PCL by the dipping method employed in this work.

### 3.3.2 Corrosion Rate Analysis

We examined the corrosion rate of the Mg samples, either coated or noncoated, by performing the immersion test in Hank's solution at 37 ° C, where we measured the volume of hydrogen gas collected from the immersion media. As the Mg corrodes, the hydrogen gas is generated by the reaction (61):



As shown in Figure 3.6, as the coating thickness increased, the rate of hydrogen gas generation decreased. The average rates of gas generation for the first 14 days were 0.57 ml/cm<sup>2</sup>/day, 0.52 ml/cm<sup>2</sup>/day, 0.31 ml/cm<sup>2</sup>/day and 0.20 ml/cm<sup>2</sup>/day for NCM,

1DCM, 10DCM and 50DCM. The thicker coating appeared to hinder water permeation towards the Mg surface, thereby slower corrosion and thus, less hydrogen gas. However, the rates between NCM and 1DCM were not significantly different possibly due to the thin coating of 1DCM ( $2.88 \pm 0.91 \mu\text{m}$ ). Notably, the total amounts of generated hydrogen gas were not very different among all samples at the early stage of immersion test until day 1. This suggested rapid water absorption, albeit little, via the PCL coating due to the porosity of the coating prepared by the dipping method employed in this work (60).

We also examined the amount of Mg ions released into the Hank's solution to confirm the corrosion behavior represented by the volume of generated hydrogen gas. As shown in Figure 3.7, the average rates of released amount of Mg ions for the first 14 days again decreased as the coating thickness increased. The rates were 0.55 mg/day, 0.50 mg/day, 0.34 mg/day and 0.26 mg/day for NCM, 1DCM, 10DCM and 50DCM, respectively. Again, at the early stage of immersion test (i.e., on day 1), the released amounts were not significantly different with all samples while only 50DCM exhibited a slightly lower amount of released Mg ions. However, the difference in released Mg-ion amount became more evident from day 7, where, however, the

difference between NCM and 1DCM was still not significant, as observed with the results from hydrogen gas generation.

### 3.3.3 Surface Characterization during Corrosion

We examined the change in morphology and elemental composition of the sample surface during corrosion. As shown in Figure 3.8 (a1–a2), considerably large pits and cracks were seen on the noncoated surface of Mg (i.e., NCM) even 1 day after immersion, which became more apparent after 14 day immersion, revealing comparably rapid corrosion of intact Mg. This change in morphology was not very different with that of 1DCM, also showing large pits and cracks from day 1 (Figure 3.8 (b1–b2)) probably due to the thin coating on 1DCM. However, for 10DCM and 50DCM, a relatively smooth surface was observed without apparent pits and cracks on day 1, as shown in Figure 3.8 (c1, d1). This could be ascribed to the presence of thick coating on the Mg surface, still showing the polymeric surface after 1 day immersion. After 14 day immersion, the surfaces of 10DCM and 50DCM eventually exhibited the fine network-like cracks by Mg corrosion (Figure 3.8 (c2, d2)). We also investigated the elemental composition of the surfaces

by the EDS analysis 1 day and 14 days after immersion. As shown in Figure 3.9 (a1–a2), the surface of NCM was composed of Mg, O, P and Ca, from day 1 after immersion, indicating deposition of corrosion products formed in the immersion media, Hank' s solution (Table 3.1). For 1DCM, the major elements of corrosion products, Mg, O, Ca and P, were also found from 1 day after immersion (Figure 3.9 (b1–b2)). Notably, C was not observed from day 1, suggesting an almost immediate disappearance of a thin polymer coating after immersion possibly due to detachment of the coating from the surface. However, as the thickness increased, the presence of the polymer coating was discernible during the period of the immersion test. The presence of C was evident 1 day after immersion with 10DCM, which, however, was not seen after 14 day immersion (Figure 3.9 (c1–c2)). After immersion, the elements of Mg, P and Ca were observed, indicating the occurrence of corrosion from day 1. However, with 50DCM, those elements of corrosion products were not observed on the surface 1 day after immersion (Figure 3.9 (d1)). Only C and O were detected, implying that the surface was fully covered with the PCL coating to hinder the corrosion of Mg to a large extent until day 1. After 14 day immersion, as shown in Figure 3.9 (d2), the corrosion appeared to occur even

with the presence of the polymer coating on the surface, as evidenced by detection of the elements of C, Mg, P and Ca from 50DCM.

### 3.4 Discussion

Recently, Mg and its alloys have been considered as a potential material to replace the other conventional types of metals in the field of orthopedic implants due to its biodegradability and proper mechanical strength (17). However, rapid corrosion of Mg and its alloys make their clinical application difficult, causing fast loss of mechanical strength before bone healing and local accumulation of hydrogen gas at the site of implantation. To overcome those obstacles, the surface of Mg or its alloys have been coated with many different types of biodegradable polymer (62, 63), which could impede water permeation to the Mg surface and thus, could eventually slow down the corrosion.

Given this, therefore, we increased the thickness of polymer coating to better slow down the Mg corrosion in this work. To prepare a reproducible profile of coating, the surface of Mg was coated under each of the fixed conditions, as designed in our automated apparatus (see Figure 3.1). As a result, the thicker

coating could better hinder the water permeation to the Mg surface and thus, a corrosion rate could be reduced during the period tested in this work. As shown in Figures (3.6–3.7), both the amounts of hydrogen gas and Mg ions decreased as the coating thickness increased. This result may allow one to simply conclude that the corrosion of Mg can be controlled by varying the thickness of polymer coating.

However, there are several critical limitations, considering the long-term application of polymer-coated Mg or its alloys. It should be noted that water permeation to the coated samples could not be completely prevented even at the early stage after immersion. Both hydrogen gas and Mg ions were detected 1 day after immersion for all samples (Figures (3.6–3.7)). All samples, except for the 50DCM (i.e., the sample with the thickest coating), exhibited the elements from corrosion products on their surfaces on day 1 (Figure 3.9). This could be ascribed to the inherent porosity of polymer coating as it was prepared with the polymer solution followed by solvent removal. The porous structure should facilitate water absorption via the polymer matrix in the coating (62).

A poor adhesion property between polymer and Mg would be also problematic for the use of polymers as a coating material

(60, 64). As the polymer swells after water absorption, the coating can be detached nonuniformly (60, 65). In this work, the polymer was not detected on the surface 1 day and 14 days after immersion for 1DCM and 10DCM, respectively (Figure 3.9 (b–c)). Considering a relatively long period of complete PCL degradation ( $> 5$  months) (66), most of the coating layer appeared to be peeled off from the Mg surface and freed to the immersion media. This could be ascribed to the fact that the weak interaction via Van der Waals between the coating layer and Mg as well as the partially accelerated degradation of PCL owing to  $Mg(OH)_2$  as a catalysis led to be peeled off from Mg surface(35). Because of this, a long-term suppression of Mg corrosion would be difficult (60).

In perspectives of the results from this work, therefore, we suggest the following considerations for better control on Mg corrosion by polymer coating. The coating may need to be less porous to better prevent water permeation, especially at the early stage. For this reason, coating with polymer solution would not be advantageous since the following solvent removal would leave a comparable number of pores in the coating (60). In this sense, for example, coating with molten polymer would be more beneficial, which would provide with denser matrix of polymer in

the coating. In addition, the coating may need to adhere well to the Mg surface for better corrosion control. Thus, pretreatment of Mg surface would be needed before polymer coating. Previously, many potential methods have already been introduced to chemically modify the metal surface for improved adhesion of polymer (63, 67).

### 3.5 Conclusion

This study demonstrates that the addition of a biodegradable polymer coating on Mg can significantly reduce the corrosion rate, depending on the coating thickness. During the period of immersion test employed in this work, the volume of hydrogen gas and amount of Mg ions generated by corrosion decreased by almost half with a relatively small increase in coating thickness ( $\sim 13 \mu\text{m}$ ). This could be ascribed to a fairly homogeneous barrier formation with a polymer, hindering water permeation to the surface of Mg in a reproducible manner. However, the coating may not be stable even at the early period after immersion in the biological fluid. For all coating thicknesses prepared in this work ( $0 \sim 13 \mu\text{m}$ ), the corrosion appeared to start even at the early stage, showing the presence of hydrogen

gas and Mg ions in the immersion media from day 1. The analyses of elemental composition on Mg surface also indicated the deposition of corrosion products and disappearance of polymer coating at the early stage, which was more evident with the thin coatings ( $\sim 4.33 \mu\text{m}$ ). The preparation method, using a polymer solution, would need solvent removal, eventually leaving many pores in the coating. Thus, water appeared to be absorbed relatively fast after immersion, leading to water contact with Mg surface, hence early start of corrosion. A poor adhesion property of polymer and metal would also cause detachment of polymer coating, which could be affected more with swelling of porous polymer coating. Therefore, we suggest these considerations, albeit not all, for proper control on Mg corrosion with a polymer coating: modification of Mg surface prior to coating for better polymer–metal adhesion and nonsolvent processing of polymer to create a coating of low porosity.

Compound	Molecular weight (g/mol)	Mass (g/L)
$\text{KH}_2\text{PO}_4 \cdot \text{H}_2\text{O}$	<b>136.09</b>	<b>0.060</b>
$\text{Na}_2\text{KHPO}_4 \cdot 2\text{H}_2\text{O}$	<b>178</b>	<b>0.060</b>
$\text{NaCl}$	<b>58.44</b>	<b>8.000</b>
$\text{KCl}$	<b>74.55</b>	<b>0.400</b>
$\text{NaHCO}_3$	<b>84.01</b>	<b>0.350</b>
$\text{MgSO}_4 \cdot 7\text{H}_2\text{O}$	<b>246.47</b>	<b>0.200</b>
Glucose	<b>180.16</b>	<b>1.000</b>
$\text{CaCl}_2 \cdot 2\text{H}_2\text{O}$	<b>147.02</b>	<b>0.185</b>

**Table 3.1** Compositions of Hank's solution used for the immersion test.

Dipping Number	Average thickness of coating ( $\mu\text{m}$ )
1	<b>2.88 <math>\pm</math> 0.91</b>
10	<b>4.01 <math>\pm</math> 0.40</b>
50	<b>13.41 <math>\pm</math> 0.36</b>

**Table 3.2** Average thicknesses of PCL coatings according to the number of dippings.

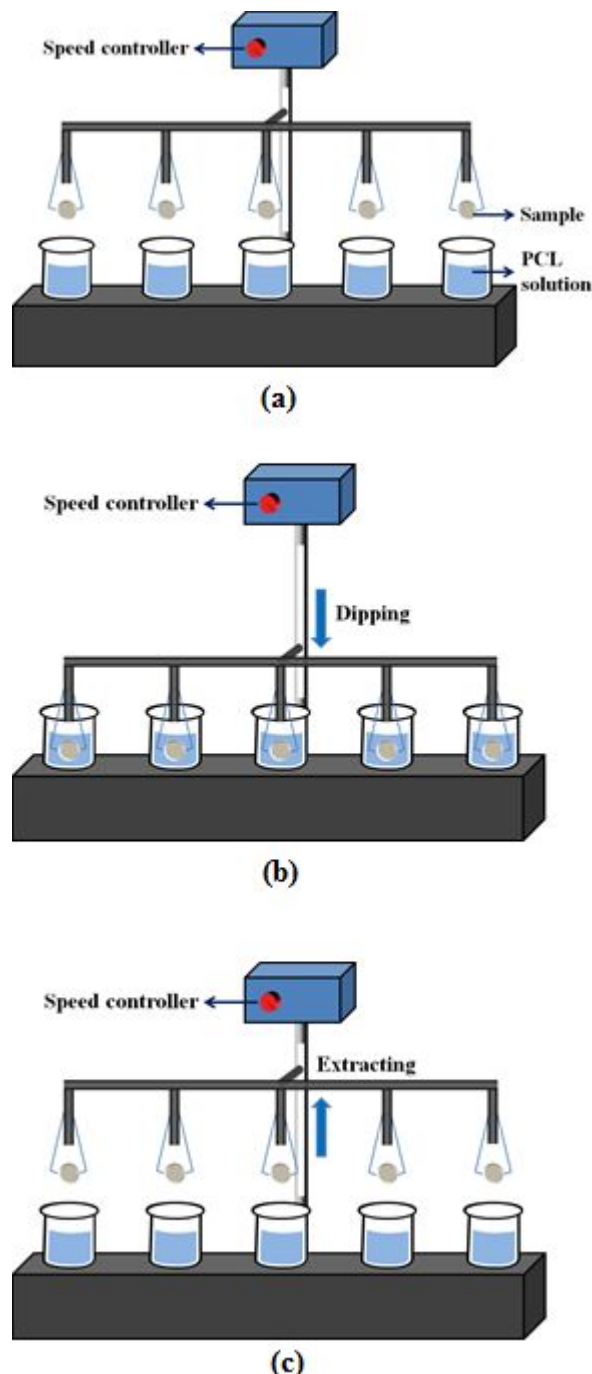


**Fig. 3.1** Schematics of an automated apparatus for polycaprolactone (PCL) coating. The Mg coins were (a) loaded into the apparatus, (b) dipped into 5% w/v PCL solution for 5 s and (c) extracted to the air for 60 s, completing a single set of dipping process.

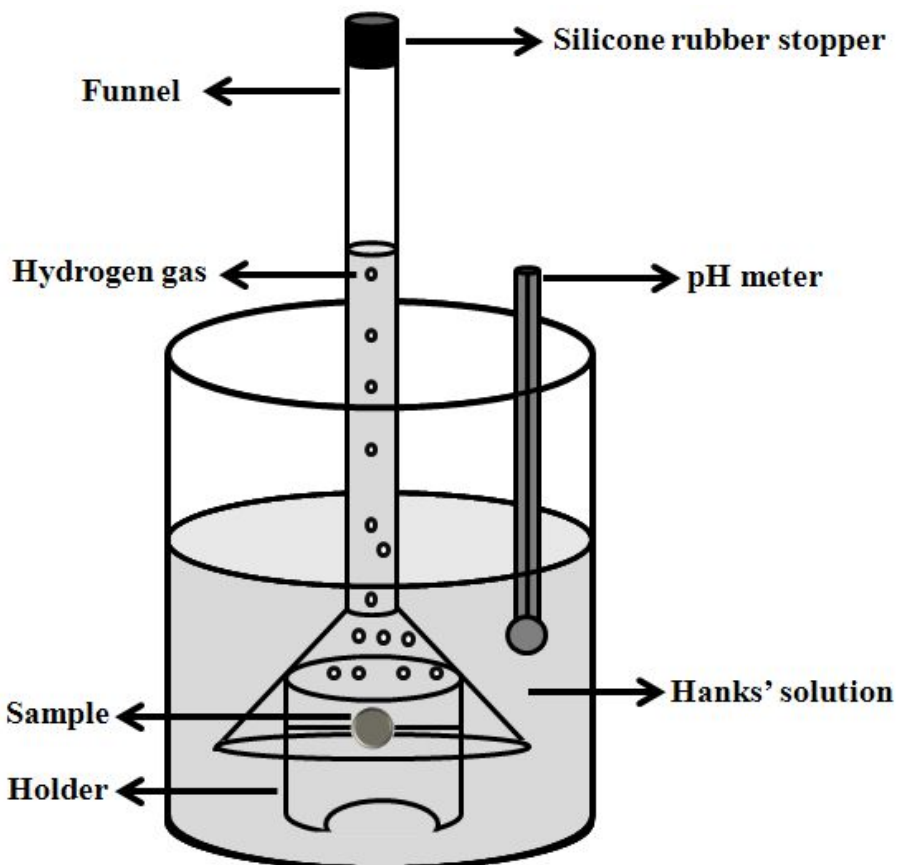


**Fig 3.2** Schematic illustration of a funnel system prepared measurement of the hydrogen gas volume generated by corrosion.

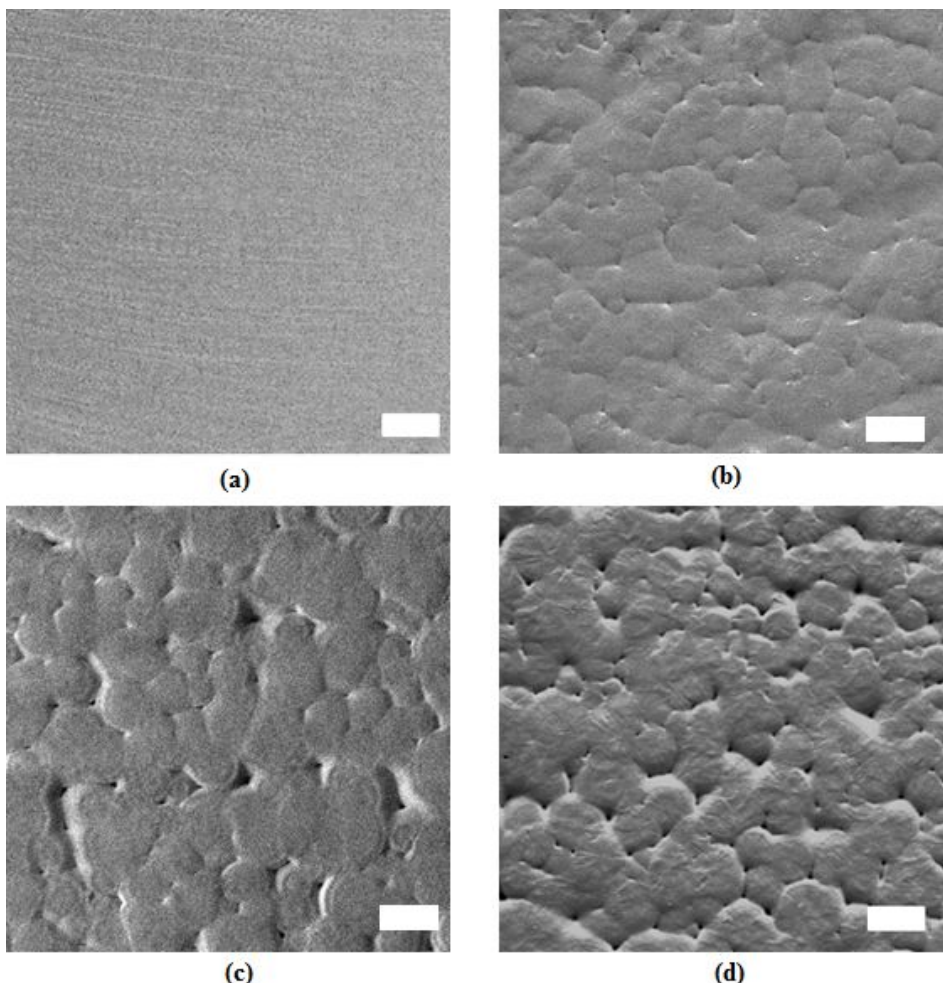


**Fig. 3.3** SEM images of the surfaces of (a) NCM, (b) 1DCM, (c) 10DCM and (d) 50DCM. Scale bars = (a) 100  $\mu\text{m}$  and (b-d) 10  $\mu\text{m}$ , respectively.

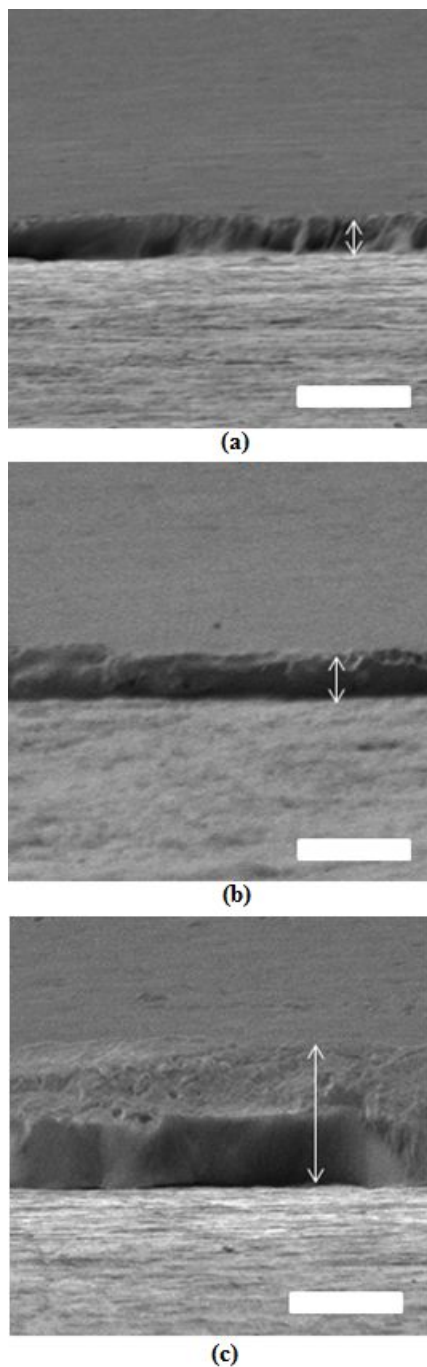
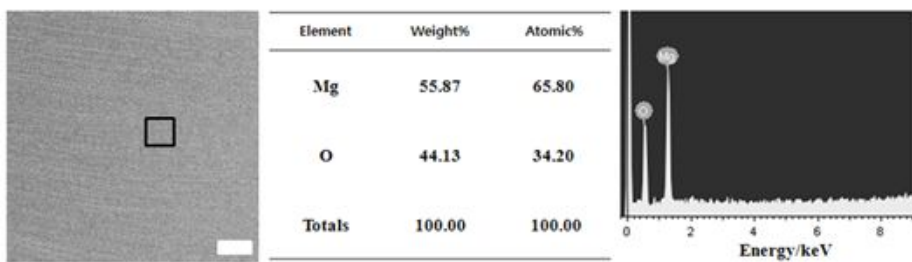
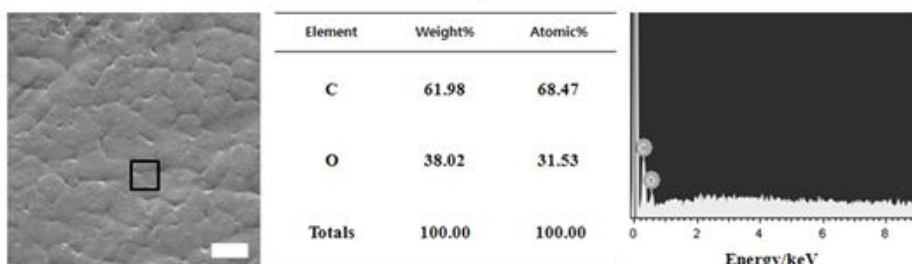


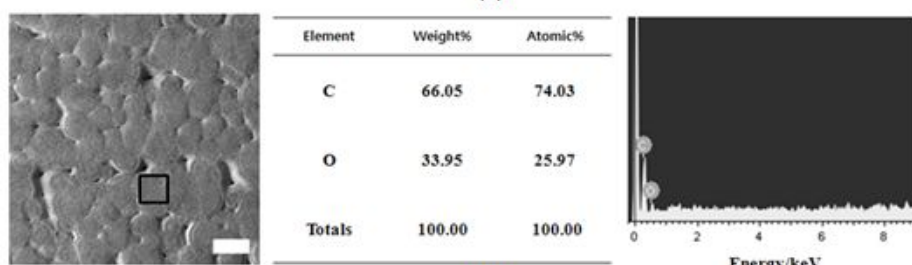
**Fig. 3.4** SEM images of the half-masked samples of (a) 1DCM, (b) 10DCM, and (c) 50DCM observed from the side. The white arrows each indicate the coating thickness, measured between the top of the coating and the Mg surface. Scale bars = 10  $\mu\text{m}$ .



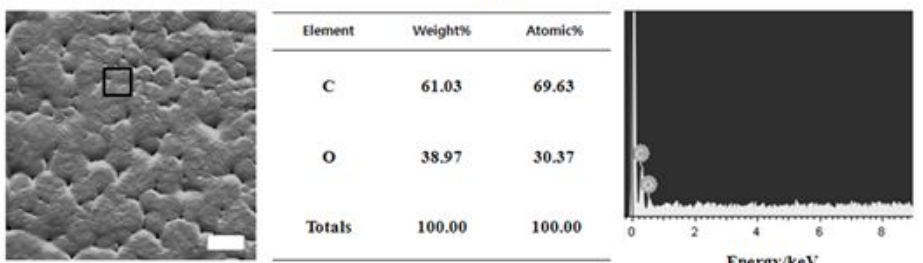
(a)



(b)

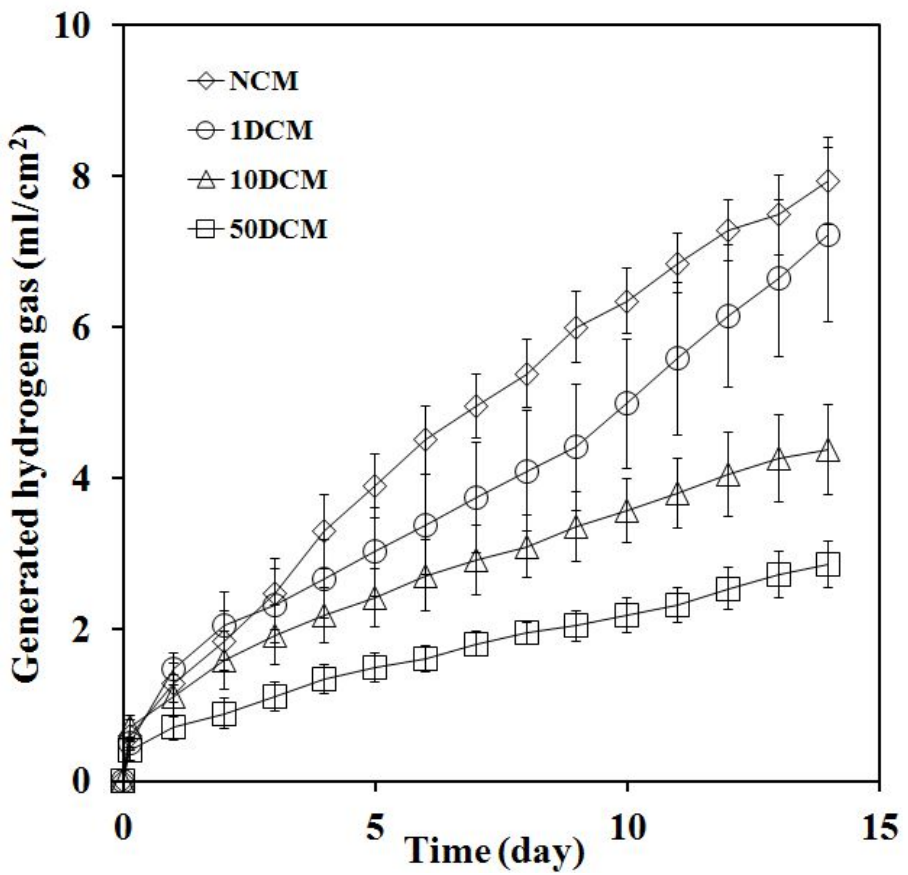


(c)

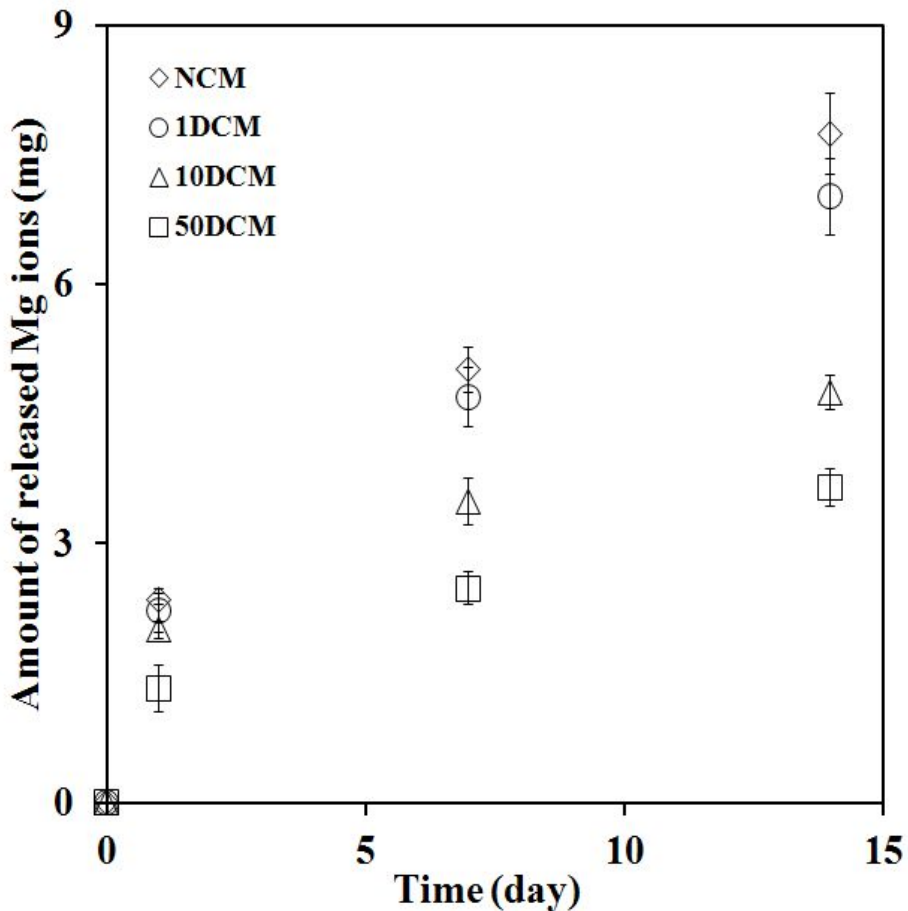


(d)

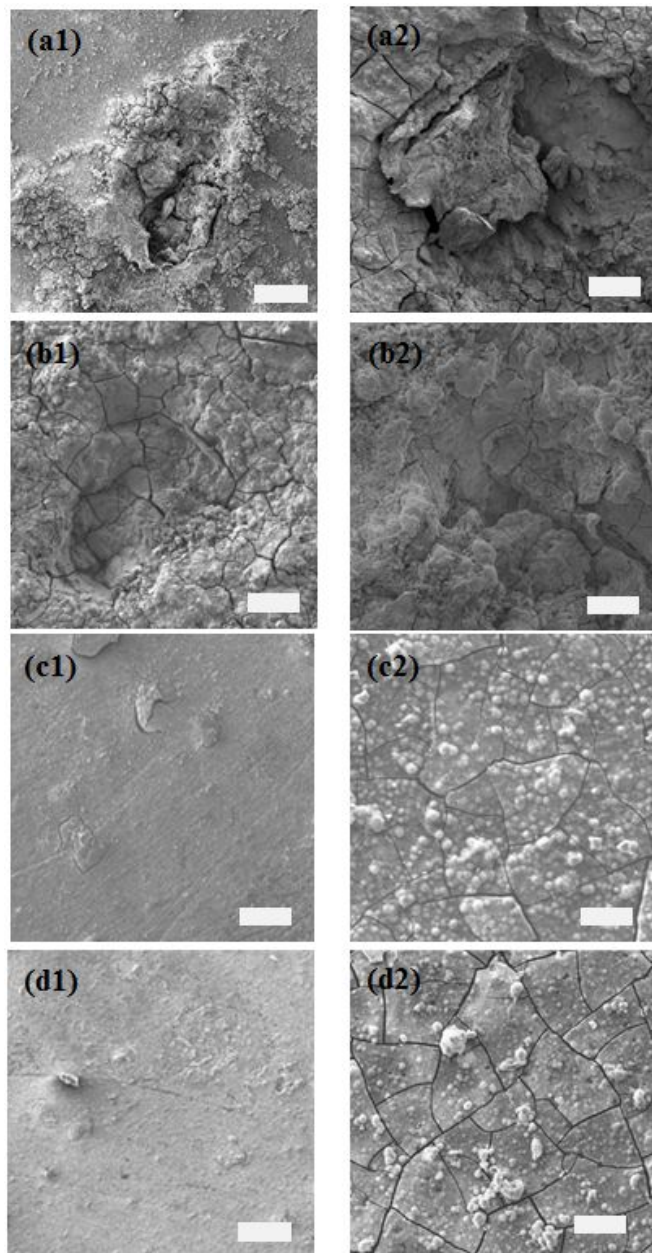
**Fig. 3.5** SEM images and EDS spectra obtained from (a) NCM, (b) 1DCM, (c) 10DCM and (d) 50DCM. Scale bars = (a) 100  $\mu$ m and (b-d) 10  $\mu$ m.



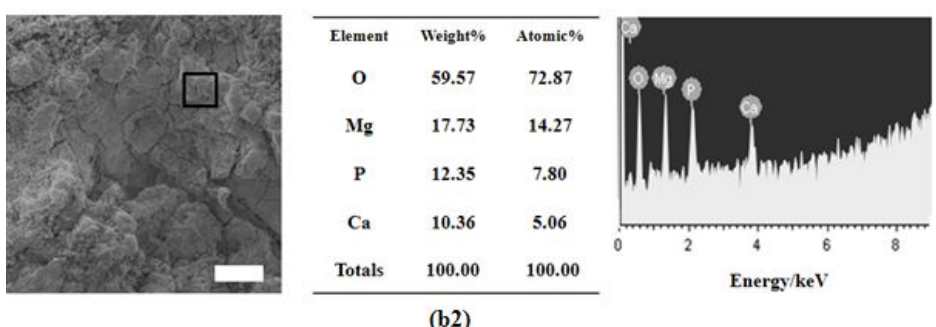
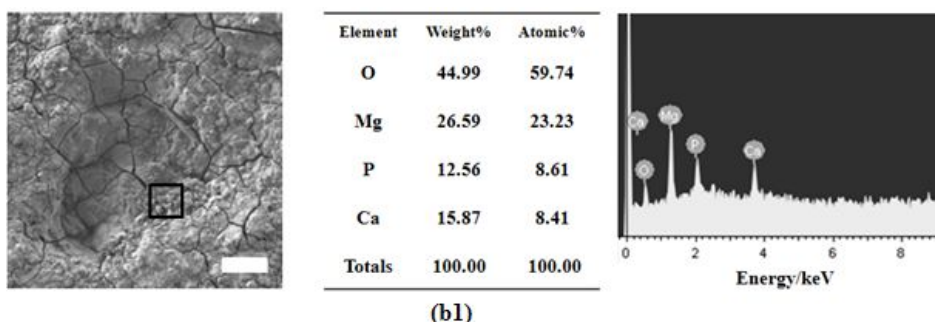
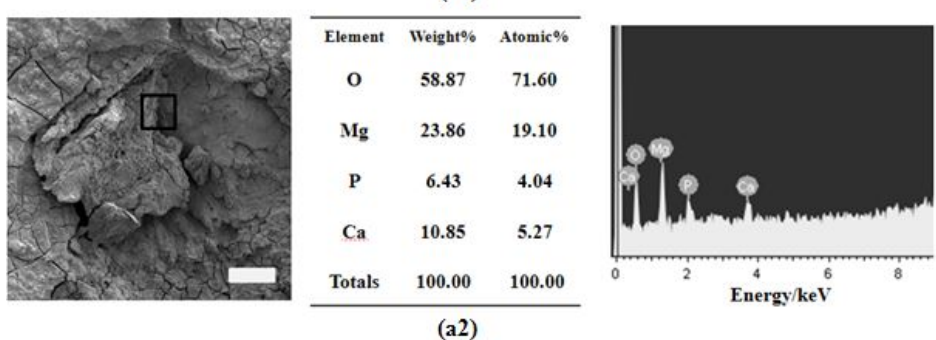
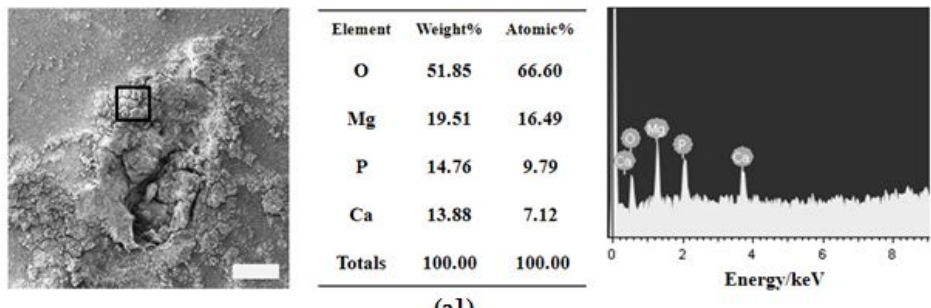
**Fig. 3.6** Volume of hydrogen gas generated from NCM, 1DCM, 10DCM and 50DCM immersed in pH 7.4 Hank's solution at 37 °C.



**Fig. 3.7** Amount of Mg ions released from NCM, 1DCM, 10DCM and 50DCM immersed in pH 7.4 Hank's solution at 37 °C.



**Fig. 3.8** SEM images of the sample surfaces obtained during the immersion test. The samples and days of imaging were (a1) NCM, day 1; (a2) NCM, day 14; (b1) 1DCM, day 1; (b2) 1DCM, day 14; (c1) 10DCM, day 1; (c2) 10DCM, day 14; (d1) 50DCM, day 1; and (d2) 50DCM, day 14. Scale bars = 200  $\mu\text{m}$ .



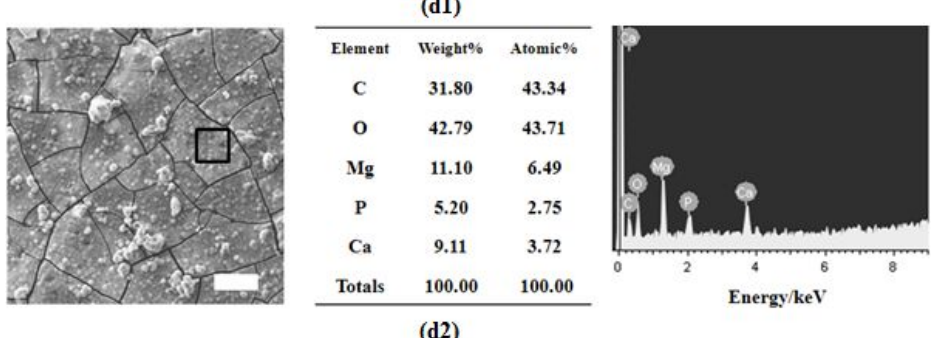
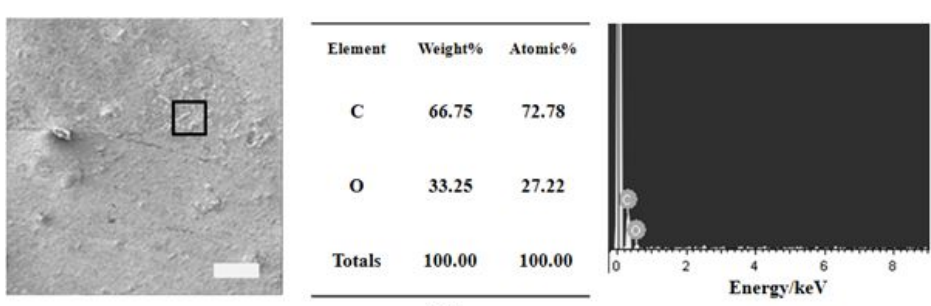
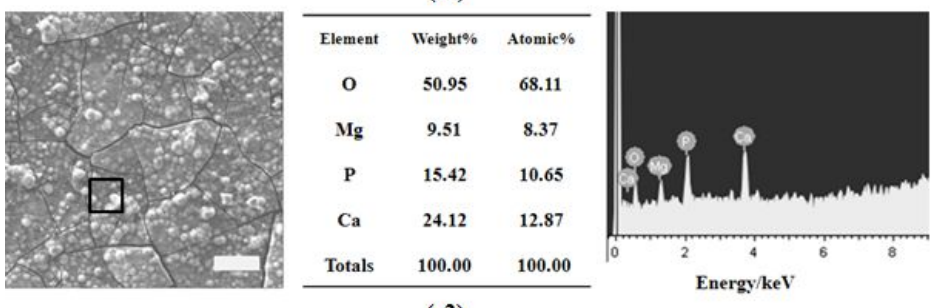
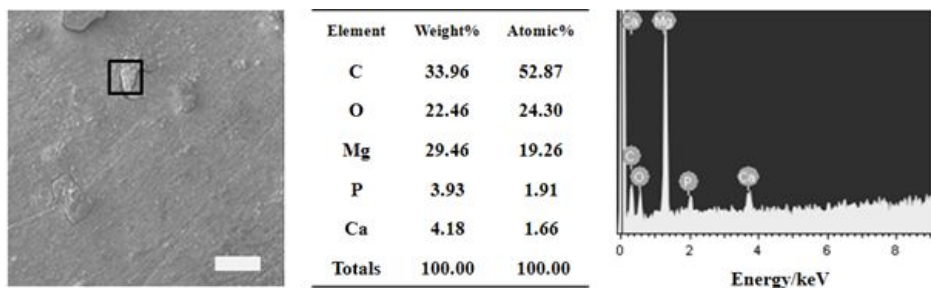


**Fig. 3.9** EDS spectra and respective elemental compositions obtained from the samples during the immersion test. The samples and days of analysis were (a1) NCM, day 1; (a2) NCM, day 14; (b1) 1DCM, day 1; (b2) 1DCM, day 14; (c1) 10DCM, day 1; (c2) 10DCM, day 14; (d1) 50DCM, day 1; and (d2) 50DCM, day 14. Scale bars = 200  $\mu$ m.

# Chapter 4

## Acute Suppression of TGF- $\beta$ with Local, Sustained Release of Tranilast against the Formation of Fibrous Capsules around Silicone Implants

### 4.1 Introduction

Silicone implants have been used over the past four decades for breast augmentation and post-mastectomy breast reconstruction

(20, 68). The capsular contracture that originates from pathological fibrosis is one of the most unfavorable complications, with a reported incidence of 1.3–30 % in patients undergoing breast implant surgery (24, 69). These patients must often undergo revision surgery to replace the implant (22) and are therefore at increased risk of developing complications and are burdened with financial difficulties (19).

Silicone implants cause natural foreign body reactions due to acute and chronic inflammation, leading to capsular fibrosis. In general, acute inflammation lasts up to a few days, depending on the size, shape and physicochemical properties of the silicone implant (70). In these implants, neutrophils are predominantly present during the first several days and are then replaced by monocytes migrating from the vasculature; the monocytes then constitute a substantial proportion of the cell types present (71, 72). Subsequently, the monocytes differentiate into macrophages, and this differentiation is accompanied by the transition from acute to chronic inflammation (73), (74).

Macrophages secrete various cytokines during chronic inflammation (72, 75); among these cytokines, TGF- $\beta$  is known to play a major role in the regulation of fibrosis (76, 77). In the early stage of acute inflammation, TGF- $\beta$  is released during

platelet degranulation and is thus involved in the recruitment of monocytes to the silicone implant (78). However, macrophages are mainly involved in the synthesis of TGF- $\beta$  during chronic inflammation (79, 80). This late production of TGF- $\beta$  promotes the recruitment and proliferation of fibroblasts and collagen synthesis (81, 82); these phenomena are associated with the formation of a thick fibrous capsule around the silicone implant. These findings suggest that preventing the formation of the capsular contracture around the silicone implant may be possible if the expression and activity of TGF- $\beta$  can be inhibited. To this end, tranilast (*N*-[3,4-dimethoxycinnamoyl]-anthranilic acid) might have therapeutic potential based on its inhibitory effects on TGF- $\beta$  (83). In particular, tranilast inhibits the secretion of TGF- $\beta$  and the expression of its receptors and blocks the phosphorylation of Smad-dependent and Smad-independent pathways in TGF- $\beta$  family signaling (84–86). Previous *in vivo* animal studies have shown that tranilast inhibited the TGF- $\beta$ -mediated accumulation of extracellular matrix components as well as fibroblasts and collagen (87–89). Interest in the anti-fibrotic effects of tranilast has increased due to its potential as a therapeutic candidate in patients with myocardial, renal and corneal stromal fibrosis (90–92).

Therefore, in this work, we hypothesized that the capsule formation, which is a later event in inflammation, would be diminished by local release of tranilast around the silicone implant, inhibiting the expression of TGF- $\beta$ , during the early stage of inflammation. Our hypothesis is supported by the fact that the early suppression of TGF- $\beta$  decreases the degree of monocyte recruitment, which would result in a lower number of differentiated macrophages (78) and thus a reduced secretion of TGF- $\beta$  during chronic inflammation(78, 81). The effects might be more pronounced with a longer suppression of TGF- $\beta$ , i.e., a prolonged release of tranilast, to better inhibit monocyte recruitment.

To test this hypothesis, we prepared three types of silicone implants for the current experiment by spray-coating the shell of clinically available silicone implants (SFS-LP, Hans Biomed, Korea) with tranilast only (i.e., TR\_IM) or with a blend of tranilast and poly (lactic-co-glycolic acid) (PLGA) (i.e., PLGA\_TR\_IM) (Fig. 4.1 and 4.2). With TR\_IM, the drug that absorbed in the silicone implant was released for short periods of time. With PLGA\_TR\_IM, the drug was released for longer periods of time, for which the PLGA served as a barrier to drug diffusion (93, 94). We also employed controls using the shell of

intact untreated silicone implants (i.e., IM) and those coated with PLGA only (i.e., PLGA\_IM). Thus, we attempted to examine the *in vivo* anti-fibrotic effects of tranilast for different periods of drug release in the area adjacent to the silicone implant. The four different types of silicone implants were inserted into the subpannliculus plane of the rats (Fig. 4.3), and the adjacent tissues were sampled at predetermined times for up to 12 weeks and analyzed histopathologically.

## 4.2 Materials and Methods

### 4.2.1 Materials

PLGA (50:50; inherent viscosity = 0.41 dl/g) was purchased from Lakeshore Biomaterials (Birmingham, AL, USA). Tween® 20 was purchased from Sigma-Aldrich (St. Louis, MO, USA). Medical epoxy (EPO-TEK® 301-2) was obtained from Epoxy Technology (Billerica, MA, USA). Tranilast and the shells of commercially available silicone breast implants (SFS-LP) were kindly donated by JW Pharmaceutical (Seoul, Korea) and Hans Biomed (Seoul, Korea), respectively. Moreover, dimethylformamide (DMF) was supplied by JT Baker (Center

Valley, PA, USA). Both Zoletil® 50 and Rompun® were obtained from Bayer (Seoul, Korea). Paraformaldehyde (4 %) was supplied by Dreamcell (Seoul, Korea).

#### 4.2.2 Sample Preparation

We prepared the four different types of samples as shown below:

- (1) IM: the shell of an intact silicone implant without treatment
- (2) PLGA\_IM: the shell of a silicone implant coated with PLGA only
- (3) TR\_IM: the shell of a silicone implant coated with tranilast only
- (4) PLGA\_TR\_IM: the shell of a silicone implant coated with a blend of PLGA and tranilast

To prepare the coated samples of PLGA\_IM, TR\_IM or PLGA\_TR\_IM, a DMF solution containing PLGA only (10 % w/v), tranilast only (0.1 % w/v) or both PLGA (10 % w/v) and tranilast (0.1 % w/v), respectively, was sprayed on the outer surface of the prepared implant shell samples with a diameter of 2 cm and a thickness of 1.5 mm, i.e., with an area of approximately 3 cm<sup>2</sup>, under the following conditions: 0.8 mm diameter of a spraying nozzle orifice (Dawon Metal, Korea), 20

cm distance between the spraying nozzle and the sample, 1.03 bar spraying pressure and 2 s spraying time (Fig. 4.1). This spraying process was repeated two times separated by a 30 min drying interval. Then, two of the coated, circular shells of the same type were combined such that the uncoated, inner surfaces of the shells faced each other and were then bonded with medical epoxy (EPO-TEK® 301-2, Epoxy Technology, Billerica, MA, USA) to create the implant samples used in this work. Thus, a coated area of approximately 6 cm<sup>2</sup> was exposed for each of the implant samples. This process was followed by a 1-day drying of the coated samples under vacuum to remove the residual solvent. To prepare the IM, two of the uncoated, circular shells with a diameter of 2 cm and a thickness of 1.5 mm were attached, as described above, again creating an exposed surface of approximately 6 cm<sup>2</sup> (Fig. 4.2).

#### 4.2.3 Characterization

The surfaces of the samples were examined using scanning electron microscopy (SEM; 7501F, Jeol, Japan). Prior to this, each sample was mounted on the SEM sample holder and sputter coated with platinum for 10 min (208HR, Cressington Scientific,

England). We also obtained the Fourier transform infrared (FTIR) spectra of the samples to examine the presence of tranilast or PLGA after coating (JASCO 6100, Japan). For this examination, each sample was milled with potassium bromide (KBr) to produce a fine powder and was then compressed into a thin pellet for analyses. At least three samples were measured for each implant type.

To measure the loading amount of tranilast, TR\_IM and PLGA\_TR\_IM were each immersed in 10 ml DMF and sonicated for 60 min (NXPC-2010, KODO, Korea); the aliquot was then measured spectrophotometrically (UV-1800, Shimadzu, Japan) at a wavelength of 331 nm. At least three samples were measured for each type of implant. The *in vitro* release profiles of tranilast were obtained for the TR\_IM and PLGA\_TR\_IM groups. The samples of each of the two types were immersed in 5 ml of phosphate-buffered saline (PBS) (pH 7.4) containing Tween<sup>®</sup> 20 (1 % v/v) with continuous agitation at 125 rpm in a shaking incubator (SI-300, Jeio Tech, Korea) at 37° C. At scheduled intervals, an aliquot of release medium (3 ml) was collected and an equal amount of the same fresh medium was returned. The sampled aliquots were measured spectrophotometrically (UV-1800, Shimadzu, Japan) at a

wavelength of 331 nm. The experiments were performed in triplicate for each of the sample types.

#### **4.2.4 *In vivo* Animal Study**

All animal procedures were performed in accordance with the National Research Council's Guide for the Care and Use of Laboratory Animals and approved by the Institutional Animal Care and Use Committee at Seoul National University Bundang Hospital (BA1102-077/006-01).

Male Sprague-Dawley rats aged 8 weeks and weighing 250–300 g were used for the *in vivo* animal experiments. Depending on the types of inserted sample, the animals were divided into four groups: those with IM inserted (IM group), those with PLGA\_IM inserted (PLGA\_IM group), those with TR\_IM inserted (TR\_IM group) and those with PLGA\_TR\_IM inserted (PLGA\_TR\_IM group). At least 30 animals were assigned to each of the implant groups. The detailed surgical procedures are described in Fig. 4.3. For the biopsy procedure, five animals were randomly selected from each experimental group and then sacrificed using carbon dioxide at 1, 2, 4, 6, 8 and 12 weeks after surgery. In each of the sacrificed animals, a dorsal region

was surgically removed to obtain a whole tissue sample in a single block, including the epidermis, dermis, posterior capsule, implant and anterior capsule, for histopathologic examinations.

#### 4.2.5 Histopathologic Evaluation by Various Staining Methods

For histopathologic evaluation, the biopsied tissue sample was fixed in 4% paraformaldehyde for 24 h, which was then infiltrated with paraffin wax. The paraffin block was cut into 4– $\mu\text{m}$  slices to prepare the tissue slides. The slides were then deparaffinized and rehydrated with xylene and ethanol for staining. The stained slides were evaluated by a professional pathologist using an optical microscope (X4, Carl Zeiss, Germany). At each biopsy time and for each implant sample, at least four images were obtained from each of the five animals, giving a total of at least 20 images for statistical analysis.

The capsule thickness was evaluated using hematoxylin and eosin (H&E) staining. In this work, we defined the capsule to include all three layers, *i.e.*, the internal layer of synovial-like metaplasia, the intermediate layer of conjunctive tissue and the external layer of collagen formed on the surface of the implant,

and we chose the thinnest region from each of the sample images to measure the capsule thickness (95, 96). To evaluate the density of collagen deposition around the implant, we performed Masson's trichrome (MT) staining (97). The collagen was stained blue; thus, the area of blue color from each image was selectively measured using Image J software (National Institutes of Health, Maryland, USA). The selected area was then divided by the whole tissue area in the same image to give the percentile value of collagen density. The numbers of fibroblasts, macrophages and monocytes and the degree of TGF- $\beta$  expression were semi-quantitatively evaluated using immunohistochemical (IHC) staining, and the analysis yielded the following grades: 0 (None), 1 (Mild), 2 (Moderate) and 3 (Severe) (98, 99).

#### 4.2.6 Statistical Analysis

We performed the Levene test for comparisons among the four experimental groups (100). We also performed a multivariate analysis of variance (MANOVA) of the dependent variables, such as the time point of biopsy and the type of samples. In addition, we compared the capsule thickness, collagen density, degree of TGF- $\beta$  expression and numbers of monocytes/macrophages,

monocytes and fibroblasts among the four experimental groups. We also compared these variables between two groups (the TR\_IM and the PLGA\_TR\_IM) to evaluate the effect of the period of tranilast release on the above variables. A p-value of < 0.05 was considered statistically significant

## 4.3 Results

### 4.3.1 Implant Characterization

Fig. 4.4 shows the scanning electron micrographs of the surfaces of each sample. For the IM, the rough surface was composed of the non-uniform wells with the size of  $324.45 \mu\text{m} \pm 68.32 \mu\text{m}$ , which is attributable to the type of the breast implant, i.e., a textured-type breast implant in clinical use (SFS-LP, Hans Biomed, Korea) (Fig. 4.4(a)). After the surface coating, this roughness was still observed, as shown in Fig. 4.4(b-d). The PLGA\_IM and the PLGA\_TR\_IM, however, were seen to be covered with the polymeric layers (Fig. 4.4(c-d)). Under visual examination, we did not observe the peeling or breaking of the coating in this work.

The presence of tranilast or PLGA in the coating was verified by Fourier transform infrared (FTIR) analysis (Fig. 4.5). The

dashed lines indicate the characteristic peaks of interest. For intact tranilast, there was a characteristic peak near the wavelength of  $1500\text{ cm}^{-1}$ , and this peak was ascribed to an ortho-disubstituted benzene group (101). For the intact PLGA, there was a strong peak near the wavelength of  $1750\text{ cm}^{-1}$  due to C=O stretching in the methane group (102). For the IM, there were two characteristic peaks at wavelengths of  $800\text{ cm}^{-1}$  and  $1100\text{ cm}^{-1}$  caused by Si-CH<sub>3</sub> rocking and Si-O-Si stretching, respectively, and both originated from silicone (101). In the FTIR spectra of the coated-samples, there was an overlapping in the characteristic peaks of each constituent, suggesting that the coated samples contain their own constituents. In other words, there were characteristic peaks of PLGA and silicone for the PLGA\_IM spectra. There were also characteristic peaks that originated from tranilast and the silicone in the TR\_IM spectra. Furthermore, there were characteristic peaks of all three constituents in the PLGA\_TR\_IM spectra. In this work, a similar amount of tranilast was loaded on the surfaces of the TR\_IM and PLGA\_TR\_IM samples in a reproducible manner; the amounts were measured to be  $147.95 \pm 1.60\text{ }\mu\text{g}$  and  $140.28 \pm 4.68\text{ }\mu\text{g}$  per sample (i.e., per  $6\text{ cm}^2$  exposed area), respectively. According to the *in vitro* drug release experiment (Fig. 4.6),

tranilast was released for short periods of time (5 days) because the drug was absorbed into the silicone matrix during the coating. For PLGA\_TR\_IM, however, tranilast was released for longer periods of time (15 days) due to the presence of PLGA. In this coating, drug appeared to be released mainly by diffusion via PLGA matrix, considering a much longer time for full degradation of PLGA (103).

#### 4.3.2 Capsule Thickness

To assess the effects of tranilast and the period of its local release on capsular formation, we compared the capsule thickness among the four experimental animal groups: the animal groups implanted with IM (i.e., IM group), PLGA\_IM (i.e., PLGA\_IM group), TR\_IM (i.e., TR\_IM group) and PLGA\_TR\_IM (i.e., PLGA\_TR\_IM group) (Fig. 4.7 and 4.8). At week 1, there was no significant difference in the capsule thickness among the four experimental groups. During the early stage, the capsule defined in this work would not be mainly composed of fibrosis tissues; instead, the capsule would contain cells recruited in response to the acute inflammation, such as neutrophils, basophils and eosinophils (104). The release of tranilast did not appear to have great impact on the overall resolution of acute inflammation.

At week 2 and thereafter, there was a significant difference in  
103

the capsule thickness among the four experimental groups. At weeks 2 and 4, in the PLGA\_IM group, the capsule thicknesses were significantly smaller compared with the IM group ( $P < 0.05$ ). Until week 12, however, the capsule thickness increased and showed no significant difference compared with the IM group. During the first four weeks, the decrease in capsule thickness might be attributed to the improved biocompatibility due to PLGA, causing reduced inflammation, compared with the bare silicone surface of the IM (105). Thereafter, possibly due to the continuous degradation of PLGA and the resulting byproducts, the capsule thickness became relatively greater in the PLGA\_IM group (106), which, however, was not statistically significantly different compared with the IM group.

Until 12 weeks, however, the capsule thickness was significantly smaller in the tranilast-loaded implant groups, i.e., the TR\_IM and PLGA\_TR\_IM groups, compared with the IM group ( $P < 0.05$ ). At weeks 2, 4, 8 and 12, the thicknesses were  $502.81 \pm 115.23 \mu\text{m}$ ,  $704.61 \pm 303.02 \mu\text{m}$ ,  $1060.94 \pm 317.78 \mu\text{m}$  and  $930.75 \pm 221.44 \mu\text{m}$ , respectively, in the TR\_IM group. In addition, the thicknesses were  $733.83 \pm 77.95 \mu\text{m}$ ,  $572.25 \pm 43.72 \mu\text{m}$ ,  $785.67 \pm 146.03 \mu\text{m}$  and  $429.46 \pm 84.05 \mu\text{m}$ , respectively, in the PLGA\_TR\_IM group. However, the capsules

of the IM group were thicker at all sampled times within 2 – 8 weeks with the thicknesses ranging from  $1152.19 \pm 166.06 \mu\text{m}$  to  $1455.17 \pm 65.68 \mu\text{m}$ . At week 12, in the TR\_IM and PLGA\_TR\_IM groups, the thickness was decreased by approximately 1.2– and 2.6–fold, respectively, compared with that in the IM group.

To examine the effects of the period of tranilast release on the capsular formation, we compared the capsule thickness between the TR\_IM and PLGA\_TR\_IM groups. This comparison showed that the capsule thickness decreased by 2.2–fold in the PLGA\_TR\_IM group compared with that in the TR\_IM group at week 12 ( $P < 0.05$ ), which implies that the capsular formation was reduced to a greater extent when the period of tranilast release was longer, i.e., the expression of TGF- $\beta$  was suppressed for prolonged periods of time.

#### 4.3.3 Collagen Density

As shown in Fig. 4.9 and 4.10, we also examined the collagen density in the area adjacent to the sample using MT staining. This analysis is based on the consideration that fibrosis is characterized by the pathologic deposition of collagen (107, 108).

The collagen density was  $35.25 \pm 6.73\%$  at week 2 and  $73.89 \pm 4.13\%$  at week 12, thus showing a dramatic increase in the IM group. These results indicate that chronic inflammation occurred around the sample because of the large wounds and associated silicone implants (109, 110). Similar findings were also observed in the PLGA\_IM group; the collagen density was  $44.96 \pm 5.72\%$  at week 2 and  $84.00 \pm 4.51\%$  at week 12, representing a dramatic increase.

Of note, at week 2, the collagen density was significantly lower in the TR\_IM and PLGA\_TR\_IM groups compared with that in the IM and PLGA\_IM groups. The collagen density was  $24.42 \pm 3\%$  at week 2 and  $49.03 \pm 6.11\%$  at week 12, representing a slight increase in the TR\_IM group; both densities, however, remained significantly lower than that of the IM group ( $P < 0.05$ ). The collagen density was the lowest in the PLGA\_TR\_IM group, with a range of  $17.54 \pm 3.50\% - 23.56 \pm 0.41\%$ . Of note, at week 12, the collagen density was significantly lower in the PLGA\_TR\_IM group than in the TR\_IM group, thus confirming that the collagen density was significantly reduced when the period of TGF- $\beta$  suppression was prolonged.

#### 4.3.4 Fibroblasts

We performed a semi-quantitative analysis of the quantity of fibroblasts, a key player in the synthesis of the fibrous connective tissue during the wound healing process (109). As shown in Fig. 4.12 and 4.13, until week 12, the quantity of fibroblasts remained high in the IM and PLGA\_IM groups. This result implies that chronic inflammation was persistently present for up to 12 weeks (111, 112). In the TR\_IM and PLGA\_TR\_IM groups, however, the quantity of fibroblasts was gradually decreased during the 12-week period. Of note, at week 12, it was significantly smaller in the TR\_IM and PLGA\_TR\_IM groups compared with those of the IM group ( $P < 0.05$ ). This finding suggests that the early release of tranilast still affects the proliferation of fibroblasts even during the late stage of inflammation. We also compared the effects of the period of tranilast release on the number of fibroblasts between the TR\_IM and PLGA\_TR\_IM groups. This comparison showed a significant decrease in the PLGA\_TR\_IM group compared with that in the TR\_IM group at week 12 ( $P < 0.05$ ).

#### 4.3.5 TGF- $\beta$

As shown in Fig. 4.13 and 4.14, we evaluated the degree of expression of TGF- $\beta$ , which plays a key role in the formation of the fibrous capsule. Overall, the degree of TGF- $\beta$  expression was relatively higher in the IM and PLGA\_IM groups. However, in the TR\_IM group, even with a short release of tranilast (5-day release), the lowered TGF- $\beta$  expressions were apparent during the late stage of inflammation (at weeks 4 and 8), when the expressions were significantly different from those of the IM group ( $P < 0.05$ ). For the first 2 weeks, however, the expressions were high and were comparable to those of the IM group. The prolonged stage of acute inflammation (Fig. 4.15) appeared to continuously stimulate TGF- $\beta$  secretion until week 2 (113), and this secretion could not be suppressed in the TR\_IM group due to early completion of drug release (Fig. 4.6). At week 12, there was no significant difference in the degree of TGF- $\beta$  expression compared with the IM group ( $P > 0.05$ ). The degree of TGF- $\beta$  suppression was the highest in the PLGA\_TR\_IM group. Compared with that in the IM group, the TGF- $\beta$  suppression remained markedly lower until week 12 ( $P < 0.05$ ). Tranilast was released for up to 15 days in the PLGA\_TR\_IM group (Fig. 4.6). It also appears that the expression of TGF- $\beta$  was suppressed even during the first two

weeks, i.e., during prolonged acute inflammation. At week 2, the degree of TGF- $\beta$  expression was significantly lower in the PLGA\_TR\_IM group compared with that in the TR\_IM group.

#### 4.3.6 Monocytes/Macrophages

We performed a semi-quantitative analysis of the monocyte/macrophage quantity at the insertion site because the recruitment of monocytes and their differentiation into macrophages are highly associated with TGF- $\beta$  expression (75, 78). As shown in Fig. 4.16 and 4.17, the monocyte/macrophage quantity was higher in the IM and PLGA\_IM groups until week 12. Because of the prolonged acute inflammation (Fig. 4.15), most of the cells at week 1 should be monocytes; however, beginning in week 4, when chronic inflammation starts, most cells should be macrophages (75). Thus, macrophages may be prevalent in the IM and PLGA\_IM groups during the late stage of inflammation. In the TR\_IM and PLGA\_TR\_IM groups, however, there was a dramatic decrease in the cell quantity. At weeks 2 and 4, the cell quantity was significantly lower in the TR\_IM group compared with that in the IM group ( $P < 0.05$ ); however, there was no significant difference afterward, possibly because of a short-

term release of tranilast. In contrast, at weeks 2 – 12, the cell quantity was the lowest in the PLGA\_TR\_IM group and was significantly different compared with that in the IM group ( $P < 0.05$ ). Due to the long-term, local release of tranilast, the effect became more apparent, suggesting that the number of macrophages around PLGA\_TR\_IM was significantly lower than that around TR\_IM at week 4 and thereafter ( $P < 0.05$ ).

To obtain additional support for this conclusion, we also conducted a semi-quantitative analysis of the number of monocytes only, as shown in Fig. 4.18 and 4.19. There was a considerable decrease in monocyte number in the TR\_IM and PLGA\_TR\_IM groups compared with that in the IM group, which implied that the local release of tranilast indeed affected monocyte recruitment, especially during the early period of inflammation (week 1). The effect of the tranilast-release period was also noticeable. The monocyte number was significantly lower in the PLGA\_TR\_IM group than in the TR\_IM group ( $P < 0.05$ ) from week 1 to week 8.

#### 4.4 Discussion

Fibrotic capsule formation remains one of the most severe

complications that can occur after the insertion of silicone implants (22), and TGF- $\beta$  is known to be a key cytokine in this process. TGF- $\beta$  is involved in the recruitment and proliferation of fibroblasts and stimulates fibroblasts to secrete collagen; thus, TGF- $\beta$  plays a key role in the fibrosis associated with silicone implants (75, 78). These phenomena are mostly observed in the later stage of inflammation, *i.e.*, during the chronic inflammation stage, and are mediated by the TGF- $\beta$  released from macrophages (81). These macrophages are differentiated from the monocytes that are recruited in the early stage of inflammation (75, 114).

We therefore propose local, sustained release of tranilast around the implant to inhibit the expression of TGF- $\beta$  during the early stage of inflammation. This treatment can decrease monocyte recruitment and may subsequently reduce the differentiation of monocytes into macrophages; thus, the treatment can contribute to a reduction in the degree of TGF- $\beta$  expression during the later stage of inflammation and thereby prevent fibrosis. (115)

In our work, the capsule thickness and the collagen density at week 12 were significantly smaller and lower in the TR\_IM group than in the IM group, which served as the control group ( $P < 0.05$ ) (Fig. 4.7 and Fig. 4.9). These results indicate that the

early suppression of TGF- $\beta$  expression played a role in preventing fibrosis. Although tranilast was released only for the first five days, at week 4 and thereafter, the degree of TGF- $\beta$  expression was still significantly lower (Fig. 4.13 and Fig. 4.14). These findings might result from the significantly smaller number of macrophages observed in the TR\_IM group compared with the IM group at weeks 2 and 4 (Fig. 4.17 and Fig. 4.17). Due to the lower degree of TGF- $\beta$  expression, the number of fibroblasts was also significantly smaller in the TR\_IM group at week 12 (Fig. 4.11).

Our results also showed that the capsule thickness and the collagen density were smallest and lowest, respectively, in the PLGA\_TR\_IM group (Fig. 4.7 and Fig. 4.9). At week 12, the average capsule thickness and the collagen density were smaller and lower by 2.6 and 3.1 times, respectively, in the PLGA\_TR\_IM group compared with the IM group (Fig. 4.7 and Fig. 4.9). Moreover, the average capsule thickness and the collagen density were smaller and lower by 2.2 and 2.1 times, respectively, in the PLGA\_TR\_IM group compared with the TR\_IM group ( $P < 0.05$ ). As described herein, the recruitment of monocytes was suppressed to a greater extent with the long-term release of tranilast during prolonged acute inflammation

(Fig. 4.18 and Fig. 4.19). This suppression contributed to reducing the number of macrophages at week 2 and thereafter (Fig. 4.16). Thus, the degree of TGF- $\beta$  expression was the lowest in the PLGA\_TR\_IM group (Fig. 4.13). In association with this decrease, the number of fibroblasts was the lowest in the PLGA\_TR\_IM group to a significant extent (Fig. 4.11); therefore, less collagen was synthesized, leading to a decrease in fibrosis. In our work, the ability of long-term release of tranilast appeared to be a more important key factor to prevent capsule formation. Therefore, unlike the PLGA\_IM group, the possible effect of PLGA degradation was not evident with the PLGA\_TR\_IM group (Figs. 4.7 and 4.9).

## 4.5 Conclusion

We suggest that acute, local suppression of TGF- $\beta$ , a major profibrotic cytokine, can reduce fibrosis around silicone implants. In this work, with local, sustained release of tranilast, an inhibitory drug of TGF- $\beta$ , both implants, TR\_IM and PLGA\_TR\_IM, exhibited a significant decrease in capsule thickness and collagen density, as compared with the non-

treated intact implant. This effect was most prominent with the PLGA\_TR\_IM due to the longest period of drug release designed in this work (15 days). Suppression of TGF- $\beta$  during the early stage of inflammation can still significantly affect the formation of fibrosis, which is the later event during chronic inflammation. This can be ascribed to inhibition of monocyte recruitment mediated by early TGF- $\beta$ , resulting in a less number of macrophages differentiated from monocytes and thus, less TGF- $\beta$  secretion during chronic inflammation. In this work, even with a short period of tranilast release (5 days with the TR\_IM), a decrease in macrophage was evident at the later times, weeks 2 and 4 after insertion, giving less TGF- $\beta$  during the late-stage inflammation. With a longer period of tranilast release, therefore, the effect became more noticeable, as shown in the PLGA\_TR\_IM in this work. Overall, we conclude that acute, local release of tranilast during the early stage of inflammation can effectively reduce fibrosis capsule formation around the silicone implant.

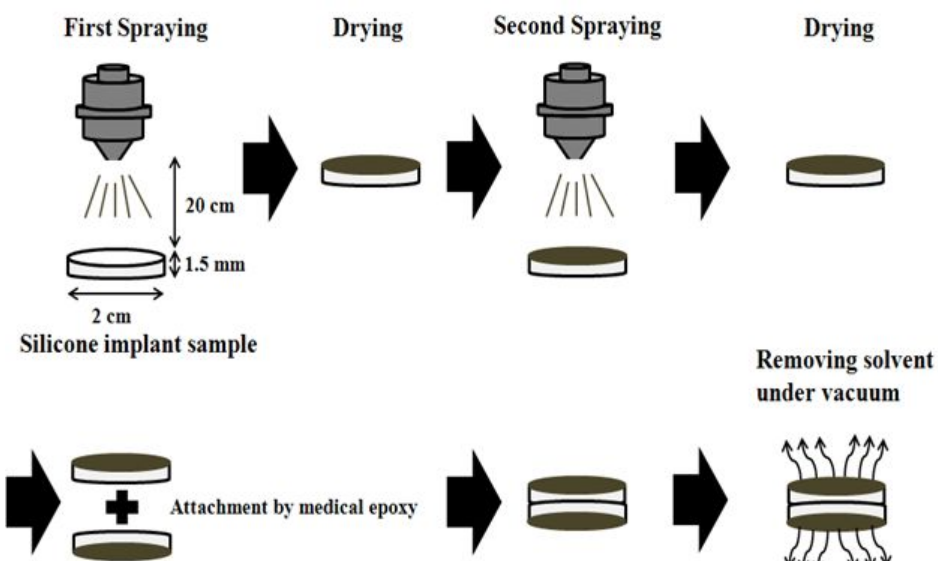


**Fig. 4.1** Schematic illustration of the coating procedure for the silicone implant

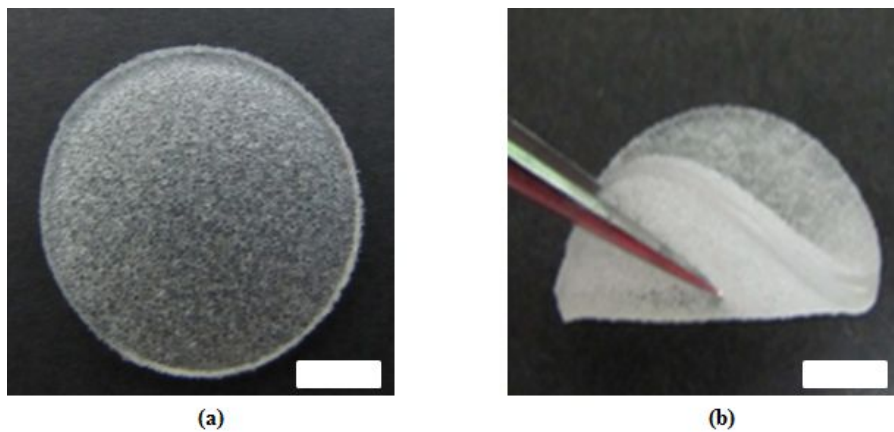


**Fig. 4.2** Optical images of the silicone implants prepared in this work. (a) Shell of a silicone implant cut into a circle, 2 cm in diameter (*i.e.*, ca. 3 cm<sup>2</sup> in area) and 1.5 mm in thickness. (b) Two of the circular shells, shown in (a), were then bonded with medical epoxy to create the implant sample used in this work. Scale bars: 5 mm.

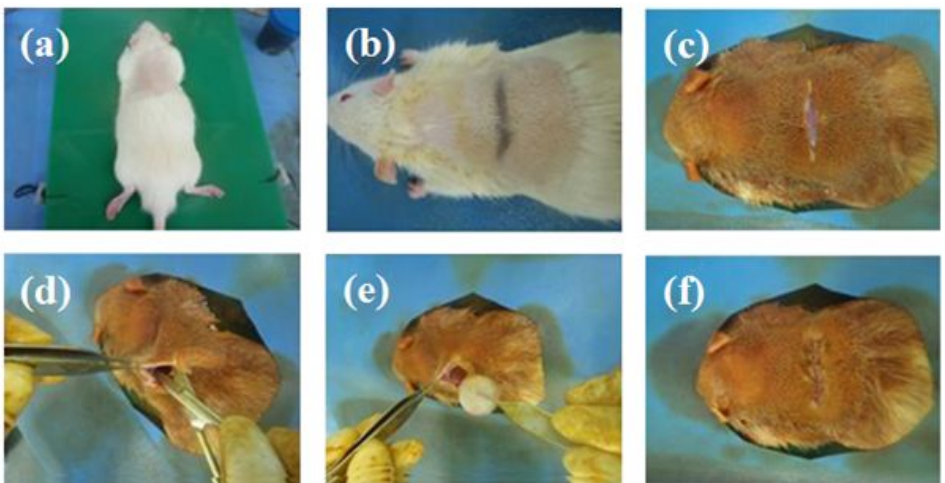


**Fig.4.3 Procedure of implantation surgery on SD rat dorsal region.** Male Sprague-Dawley rats aged 8 weeks and weighing 250-300 g were used for the *in vivo* animal experiments in the current study. The animals were maintained under a 12/12 h light/dark cycle with free access to water and food during the entire experimental period. The protocol was approved by the Institutional Animal Care and Use Committee at Seoul National University Bundang Hospital (BA1102-077/006-01). For implant insertion, (a) the animals were each anesthetized using an intraperitoneal injection of a mixture (0.1 ml/kg) of Zoletil® 50 and Rompun® (1:1 v/v). Then, the hair on the dorsal area was shaved. (b) Before incision, the surgical site was marked with a surgical pen. (c) A 2 cm incision was made along the vertebra, and (d) a pocket was made via the subpanniculus plane using a surgical scissor. (e) The sample was inserted in the pocket. (f) The incision was closed with nylon 4-0 thread (Ethicon, Cornelia, GA, USA), and the surgical site was disinfected again with Betadine.

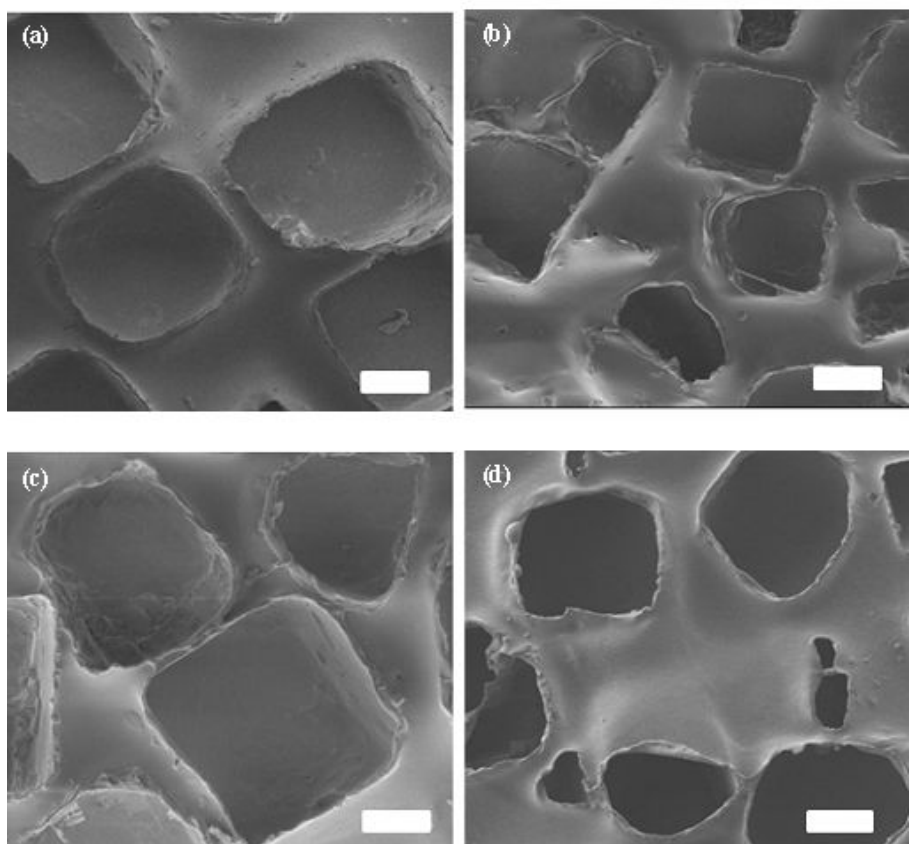


**Fig. 4.4** Scanning electron micrographs of the surfaces of (a) IM, (b) PLGA\_IM, (c) TR\_IM and (d) PLGA\_TR\_IM. The scale bars represent 100  $\mu\text{m}$ .

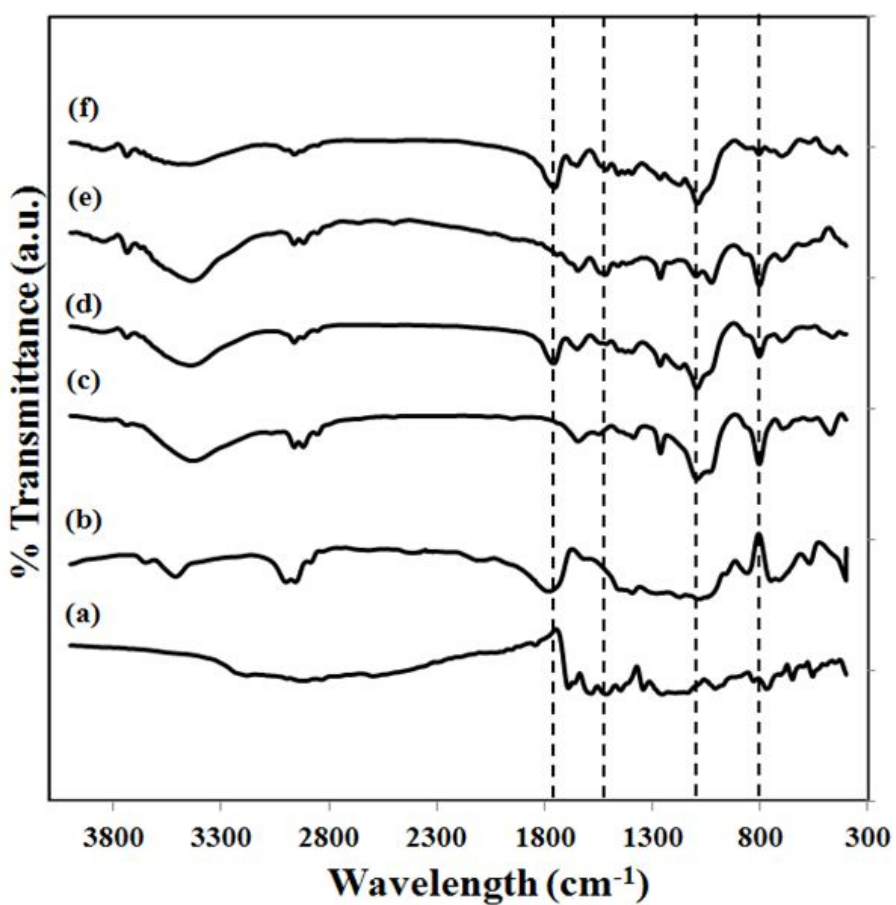


**Fig. 4.5** Fourier transform infrared (FTIR) spectra of (a) intact tranilast, (b) intact PLGA, (c) IM, (d) PLGA\_IM, (e) TR\_IM and (f) PLGA\_TR\_IM.

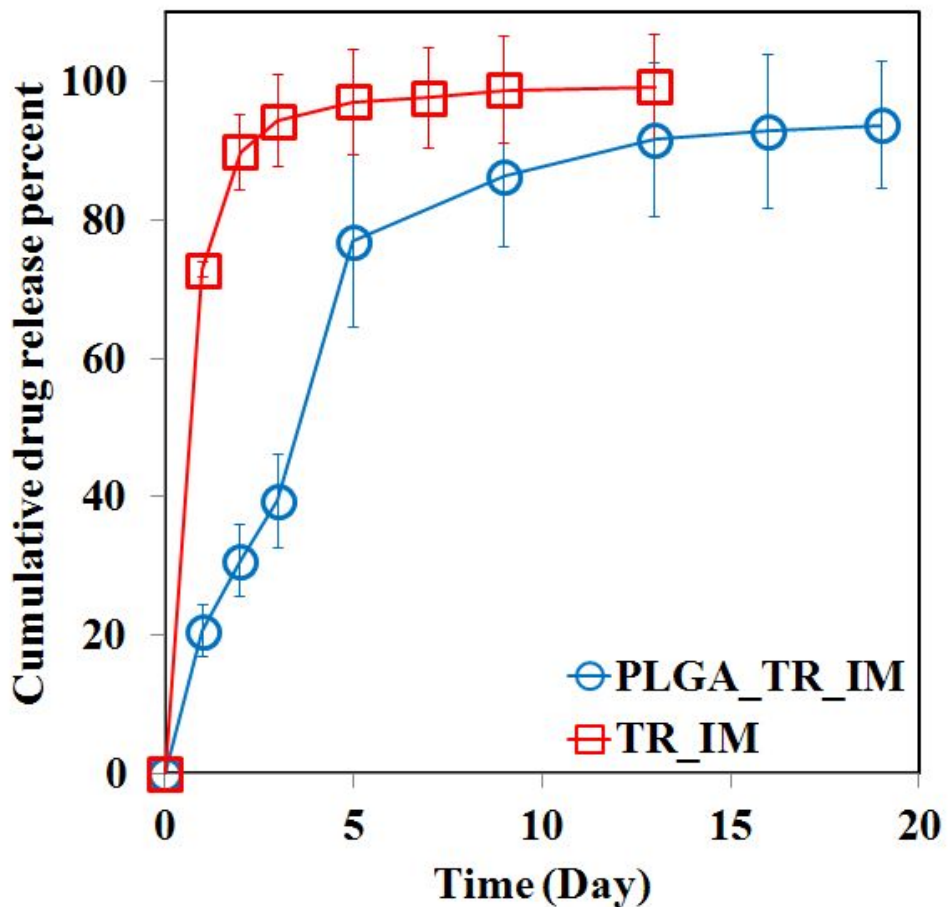


**Fig. 4.6** *In vitro* drug release profiles of the TR\_IM and PLGA\_TR\_IM.

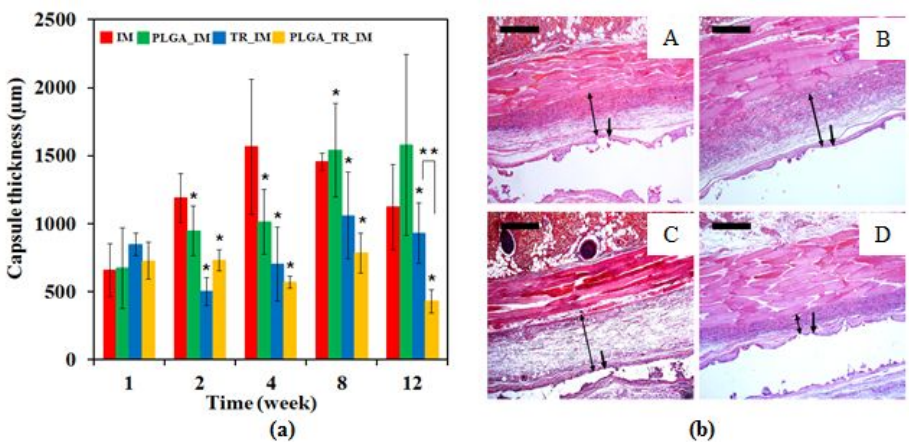
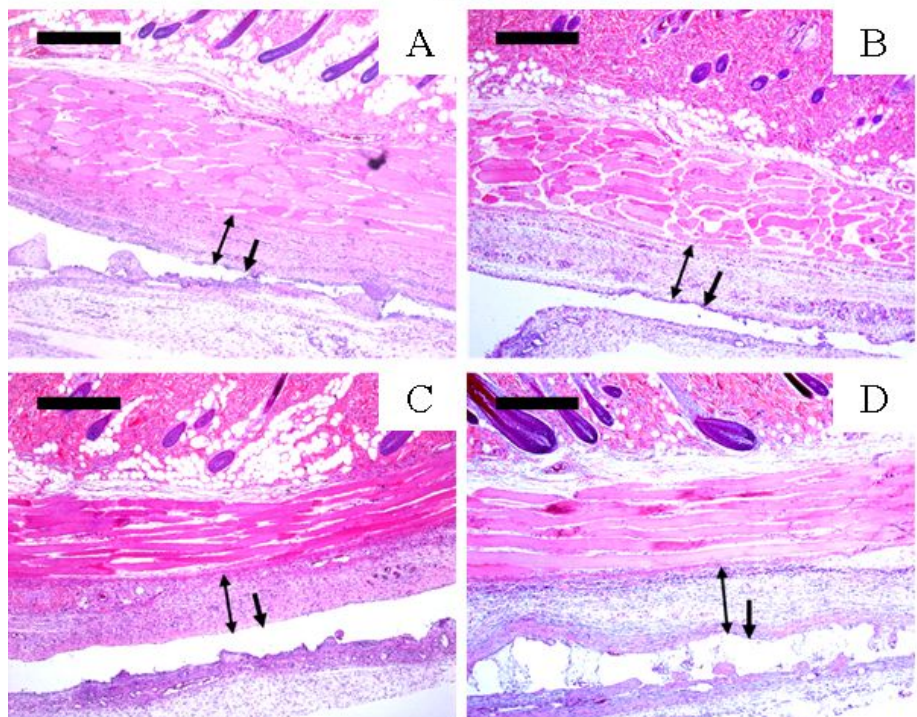
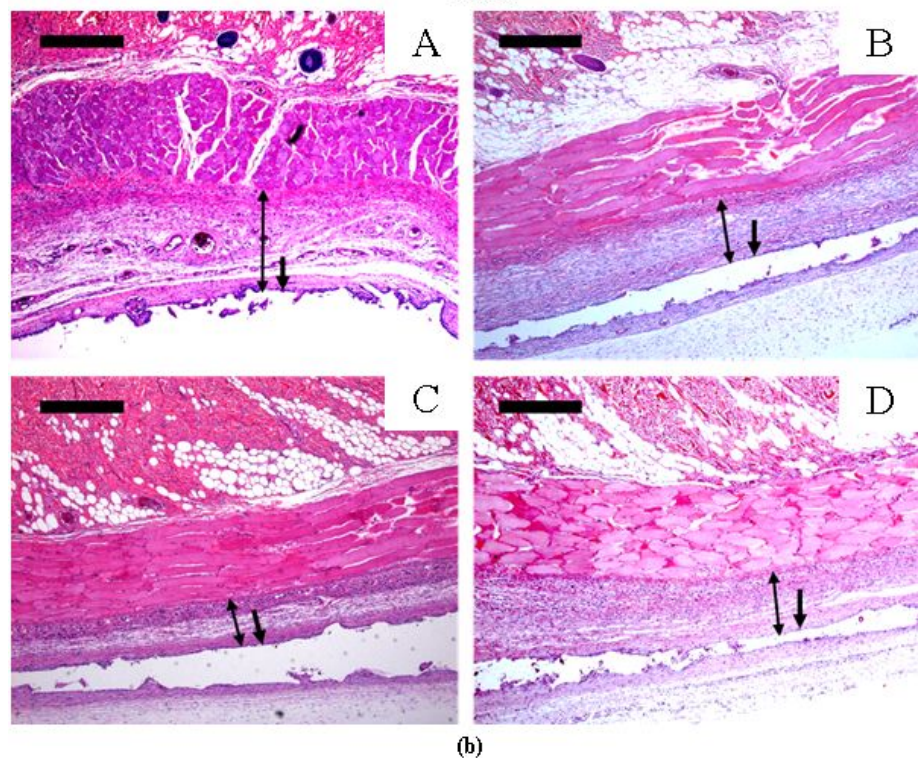


**Fig. 4.7** Evaluation of the thickness of the capsule formed around the implants. (a) Mean capsule thickness at each biopsy time and (b) representative histological images around the implants using H&E staining at week 12. Scale bars: 1 mm. The images were obtained from (A) IM, (B) PLGA\_IM, (C) TR\_IM and (D) PLGA\_TR\_IM samples. The double-sided arrow indicates the capsule thickness in the image. The single-sided arrow indicates the location of the implant in the image. The asterisk (\*) represents a significant difference compared with the IM group ( $P < 0.05$ ). Double asterisks (\*\*) represent a significant difference between the TR\_IM and PLGA\_TR\_IM

Week 1

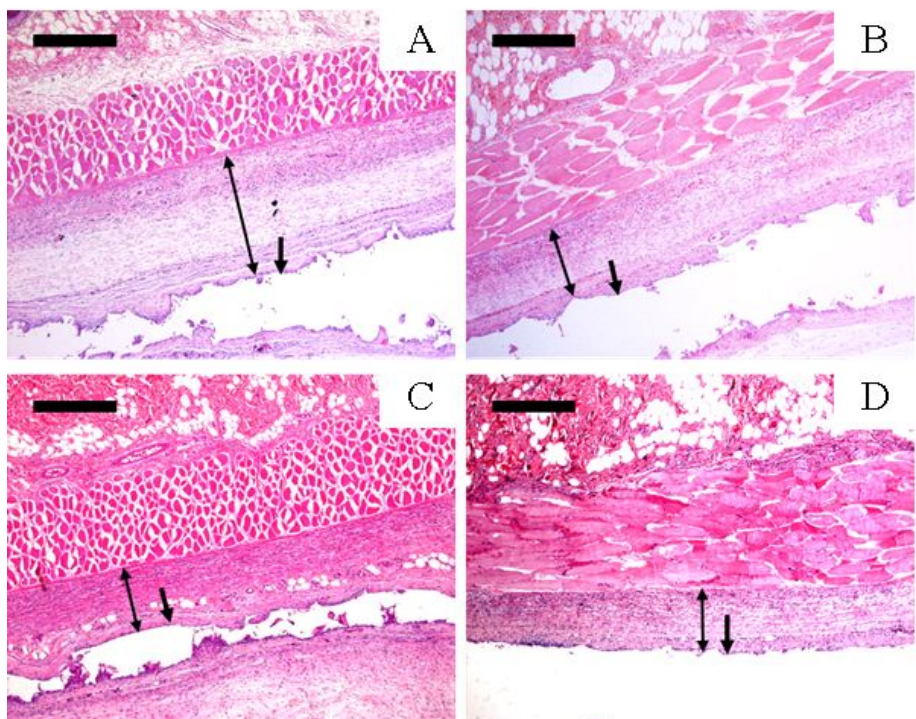


(a)  
Week 2



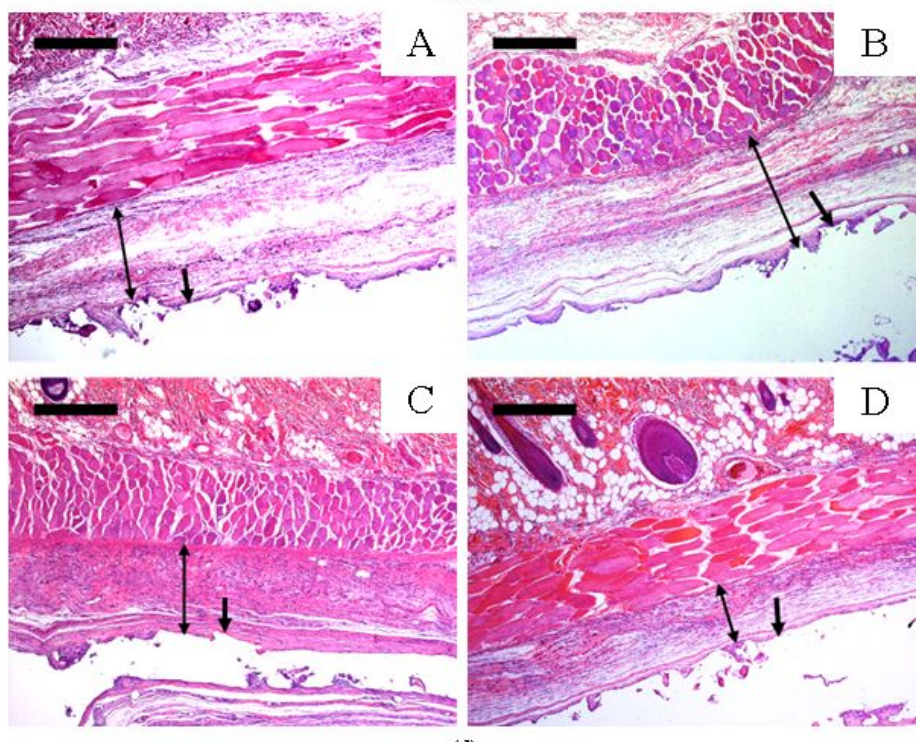
(b)

Week 4



(c)

Week 8



(d)

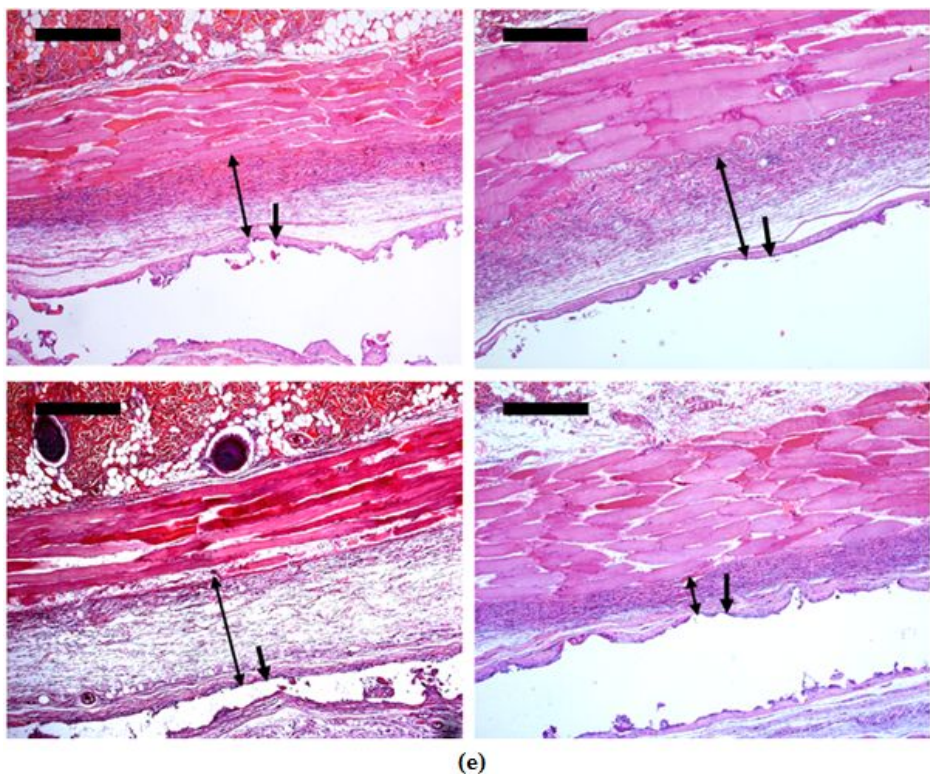


**Fig. 4.8 Representative images around the implants with H&E staining for evaluation of the capsule thickness.** The images were obtained from the (A) IM, (B) PLGA\_IM, (C) TR\_IM and (D) PLGA\_TR\_IM samples at (a) week 1, (b) week 2, (c) week 4, (d) week 8 and (e) week 12. The thinnest region from each of the sample images was chosen to measure the capsule thickness, as indicated with the double-sided arrow. The single-sided arrow indicates the location of the implant in the image. Scale bars, 1 mm.

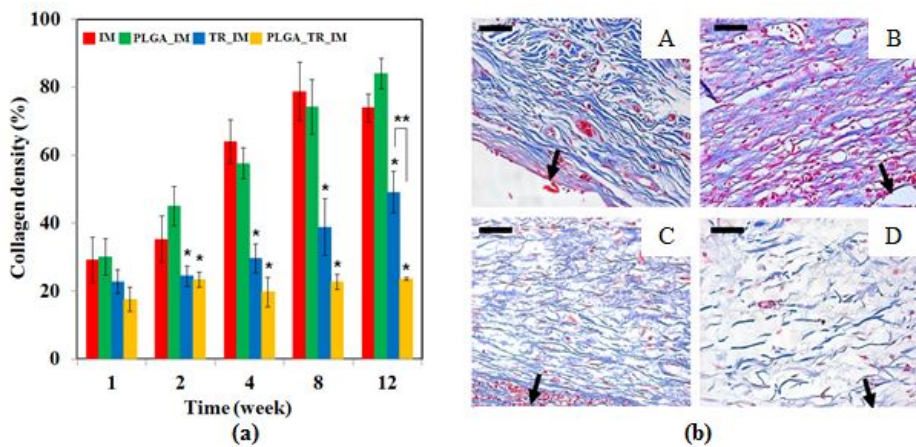
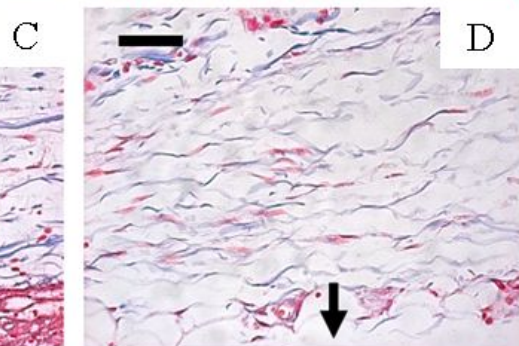
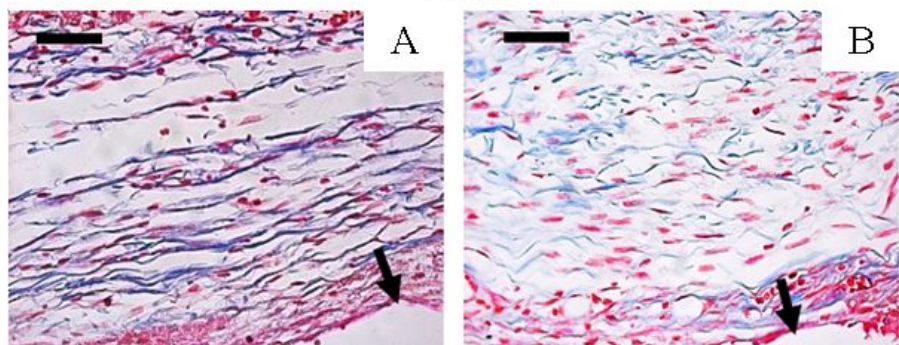
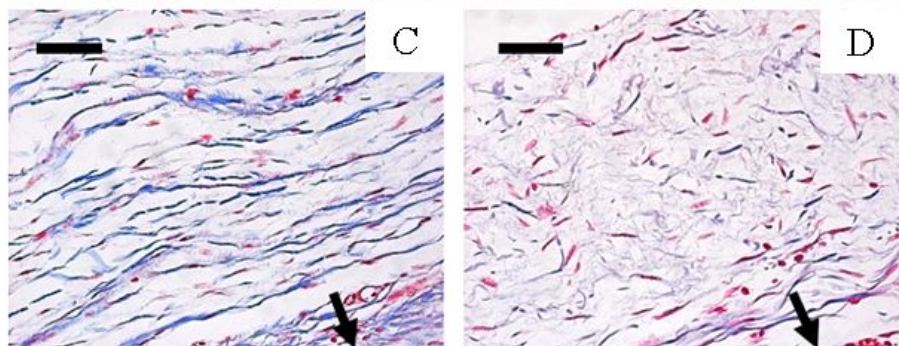
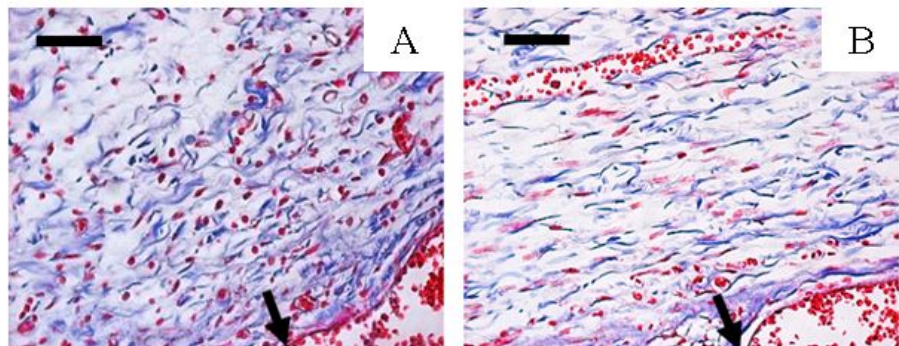


**Fig. 4.9.** Evaluation of the density of collagen deposition around the implants. (a) Mean collagen density at each biopsy time and (d) representative histological images around the implants using MT staining at week 12. Scale bars: 100  $\mu\text{m}$ . The images were obtained from (A) IM, (B) PLGA\_IM, (C) TR\_IM and (D) PLGA\_TR\_IM samples. The arrow indicates the location of the implant in the image. The asterisk (\*) represents a significant difference compared with the IM group ( $P < 0.05$ ). Double asterisks (\*\*) represent a significant difference between the TR\_IM and

Week 1

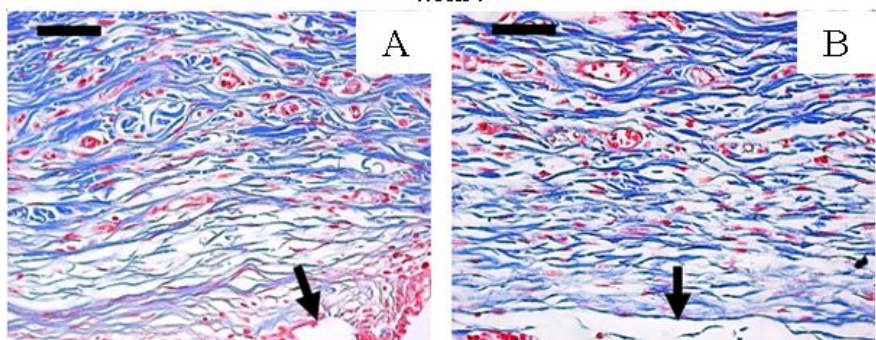


(a)  
Week 2

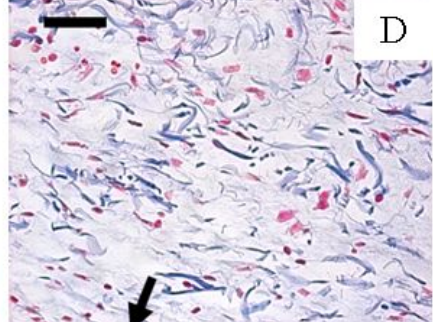


(b)

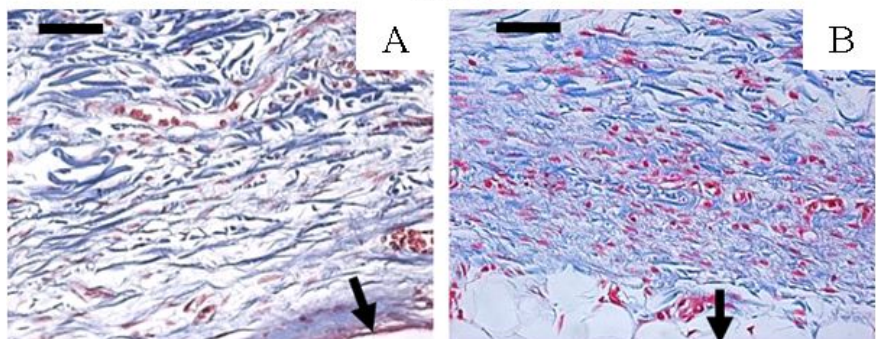
Week 4



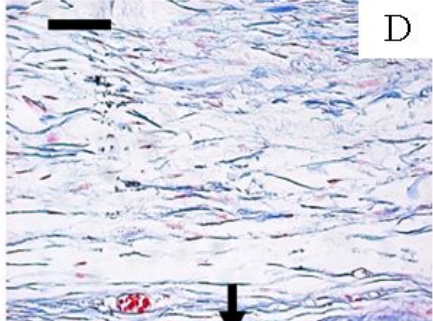
C



(c)  
Week 8



C



(d)

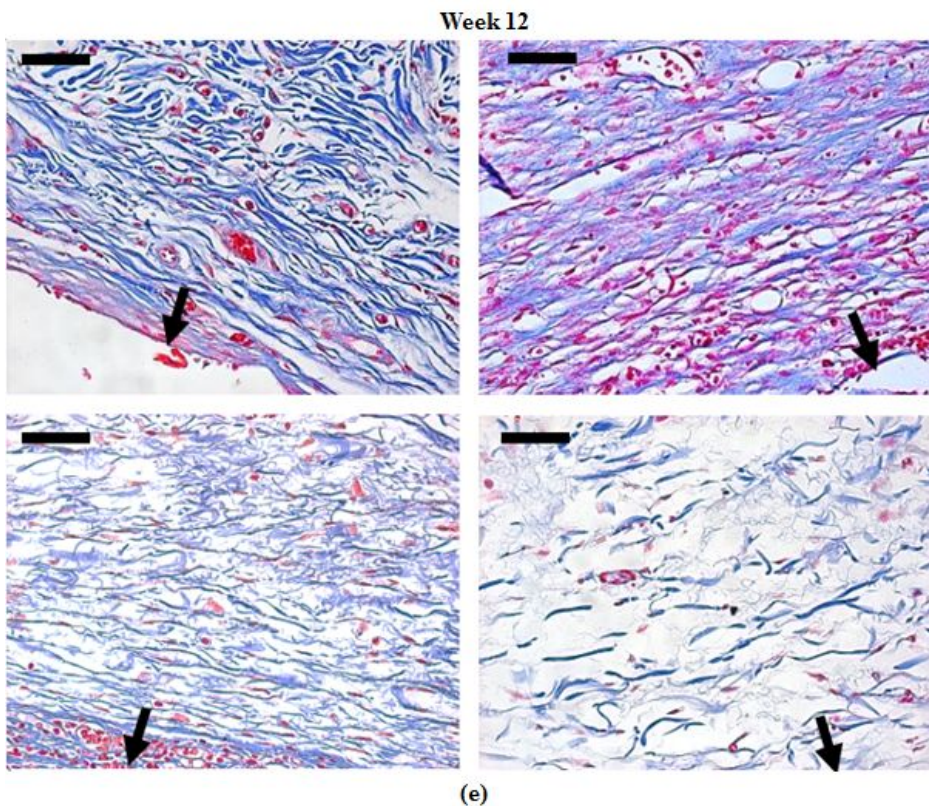


**Fig. 4.10 Representative images around the implants with MT staining for evaluation of the collagen density.** The images were obtained from the (A) IM, (B) PLGA\_IM, (C) TR\_IM and (D) PLGA\_TR\_IM samples at (a) week 1, (b) week 2, (c) week 4, (d) week 8 and (e) week 12. Scale bars: 100  $\mu\text{m}$ . The arrow indicates the location of the implant in the image.

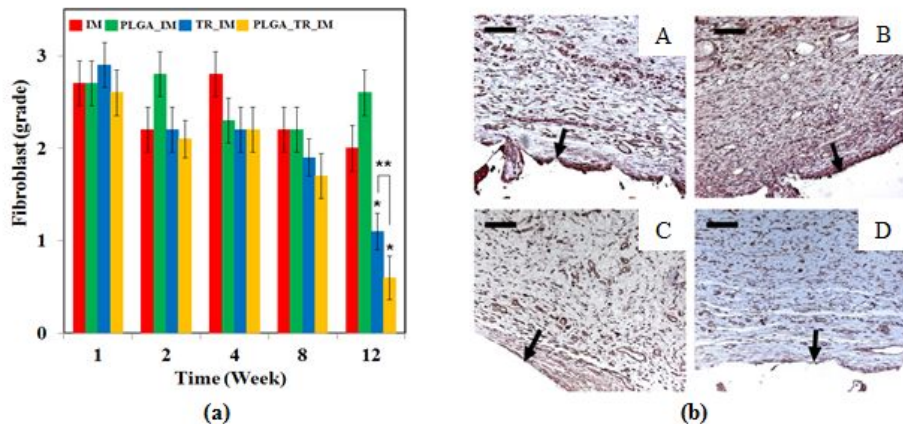
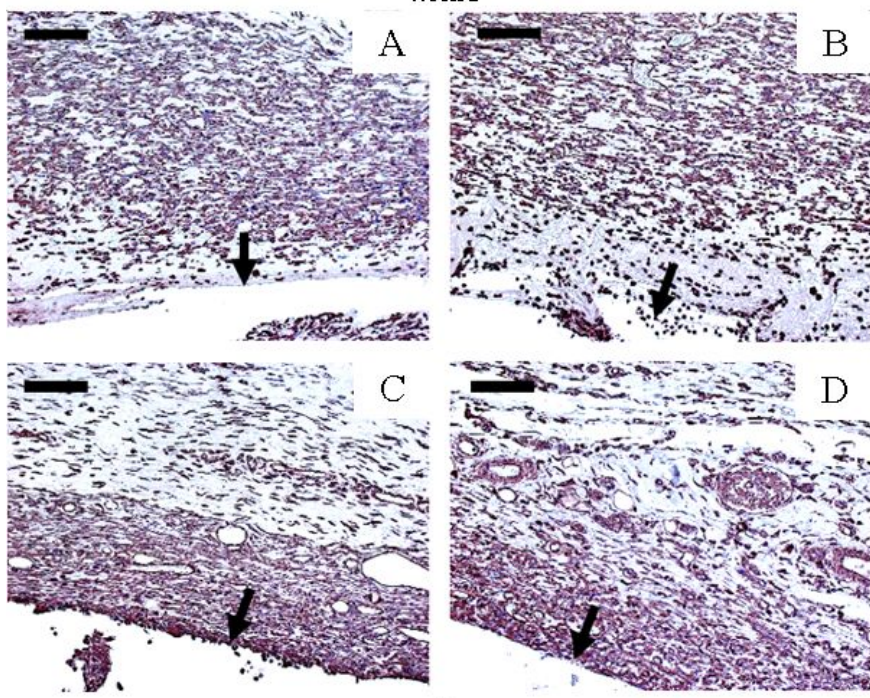


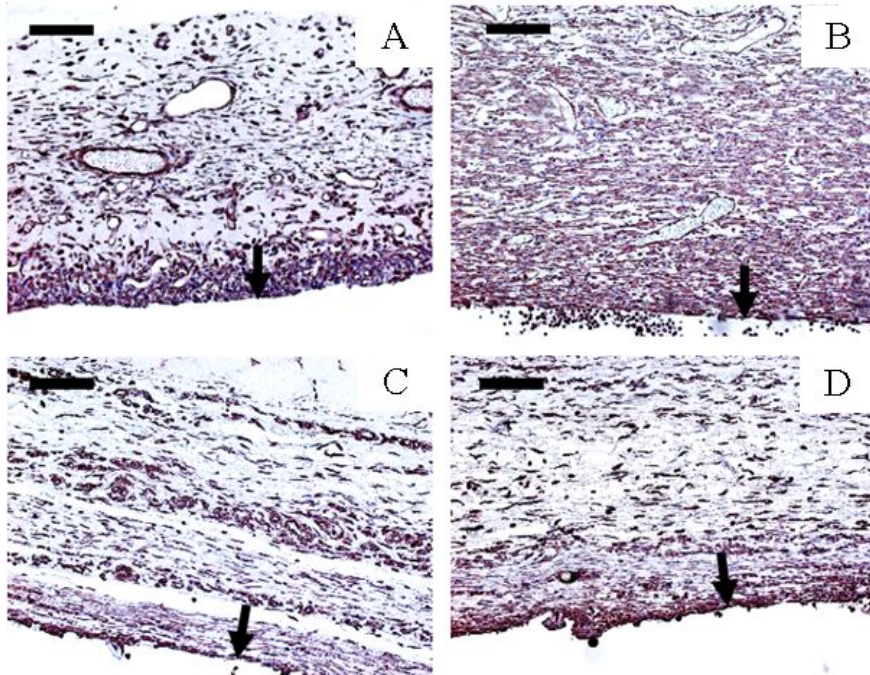
**Fig. 4.11** Evaluation of the number of fibroblasts around the implants. (a) Mean grading scores of fibroblasts at each biopsy time and (b) representative IHC images around the implants at week 12. Scale bars: 100  $\mu$ m. The images were obtained from (A) IM, (B) PLGA\_IM, (C) TR\_IM and (D) PLGA\_TR\_IM samples, and the arrow indicates the location of the implant in the image. The asterisk (\*) represents a significant difference compared with the IM group ( $P < 0.05$ ). Double asterisks (\*\*) represent a significant difference between the TR\_IM and PLGA\_TR\_IM

Week 1



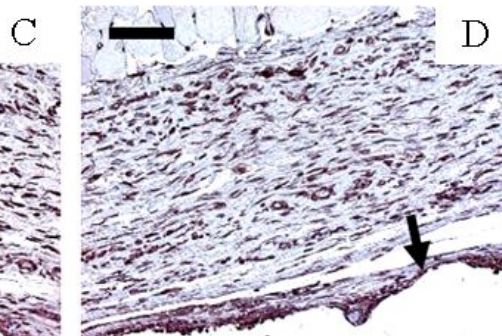
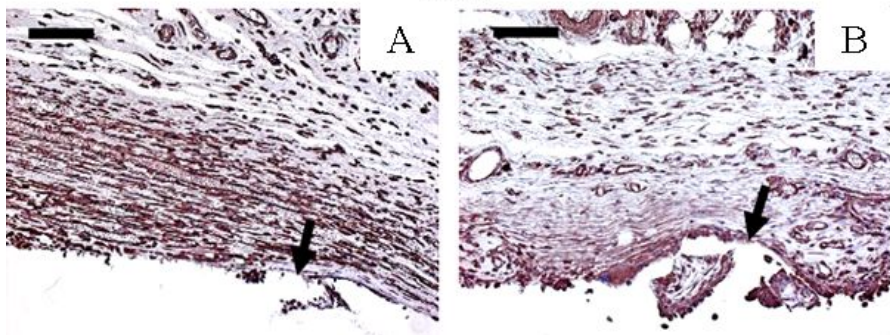
(a)

Week 2

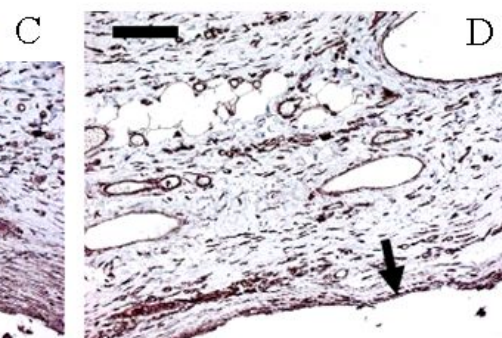
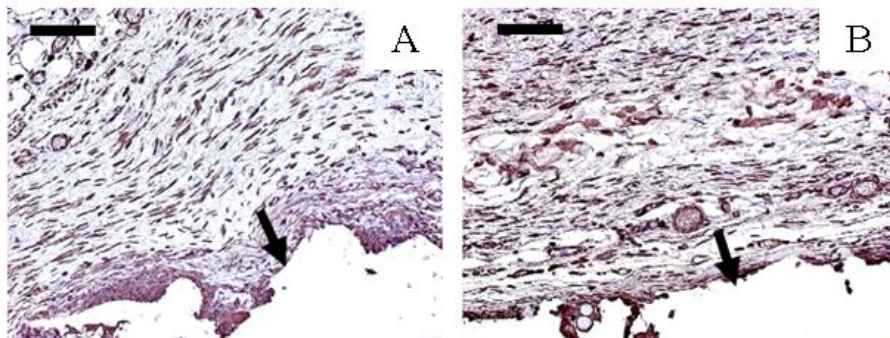


(b)

Week 4



(c)  
Week 8



(d)

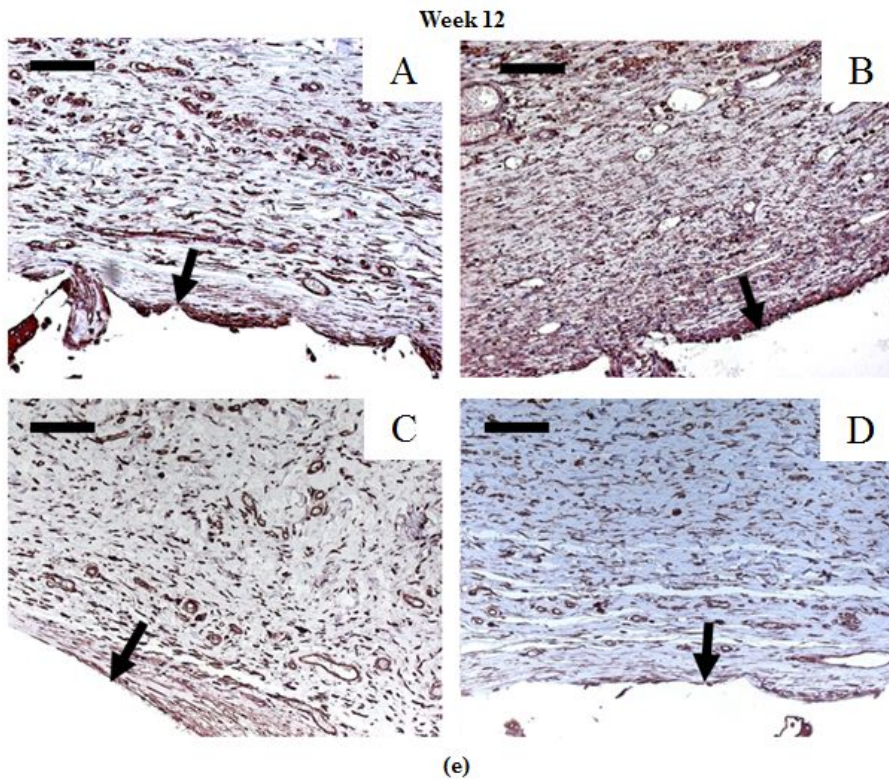


**Fig. 4.12 Representative images around the implants with IHC staining for evaluation of the fibroblast quantity.** The images were obtained from the (A) IM, (B) PLGA\_IM, (C) TR\_IM and (D) PLGA\_TR\_IM samples at (a) week 1, (b) week 2, (c) week 4, (d) week 8 and (e) week 12. Scale bars: 100  $\mu\text{m}$ . The arrow indicates the location of the implant in the image.

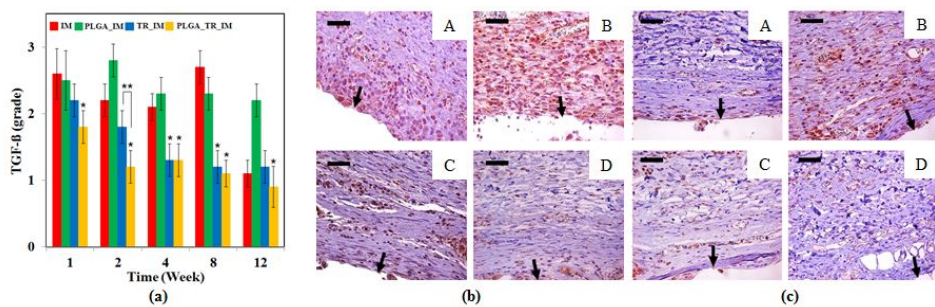
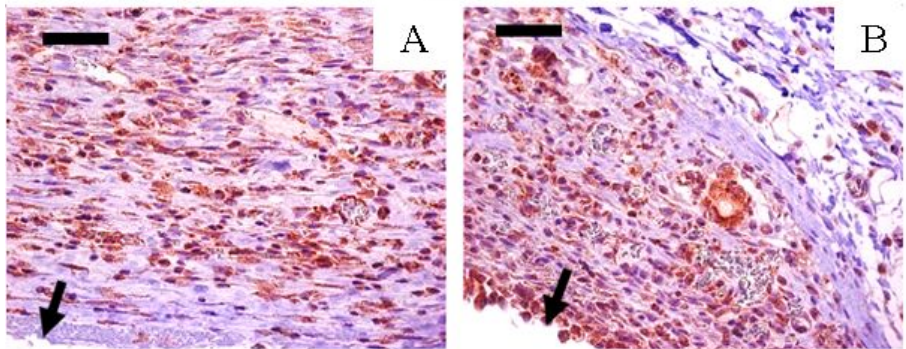


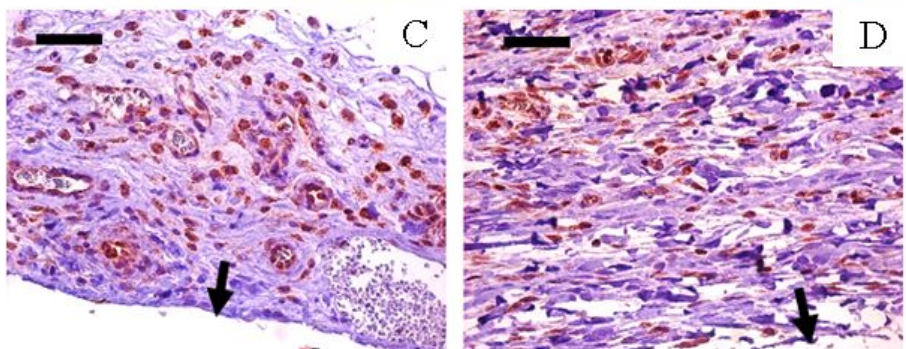
**Fig. 4.13** Evaluation of the degree of TGF- $\beta$  expression around the implants. (a) Mean grading scores of TGF- $\beta$  expression at each biopsy time and representative IHC images at (b) week 2 and (c) week 12. Scale bars: 100  $\mu\text{m}$ . The images were obtained from (A) IM, (B) PLGA\_IM, (C) TR\_IM and (D) PLGA\_TR\_IM samples, and the arrow indicates the location of the implant in the image. The asterisk (\*) represents a significant difference compared with the IM group ( $P < 0.05$ ). Double asterisks (\*\*) represent a significant difference between the TR\_IM and PLGA\_TR\_IM groups ( $P < 0.05$ ).

Week 1

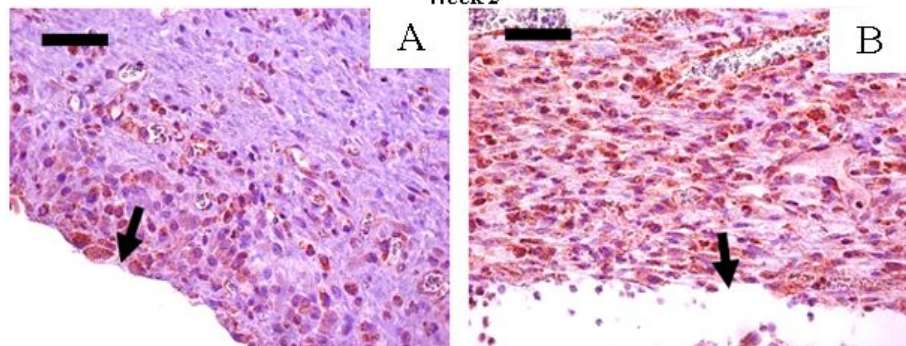


C

D

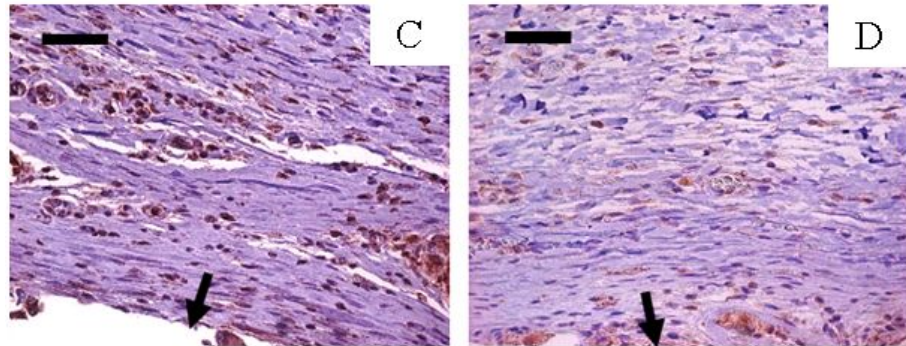


(a)  
Week 2



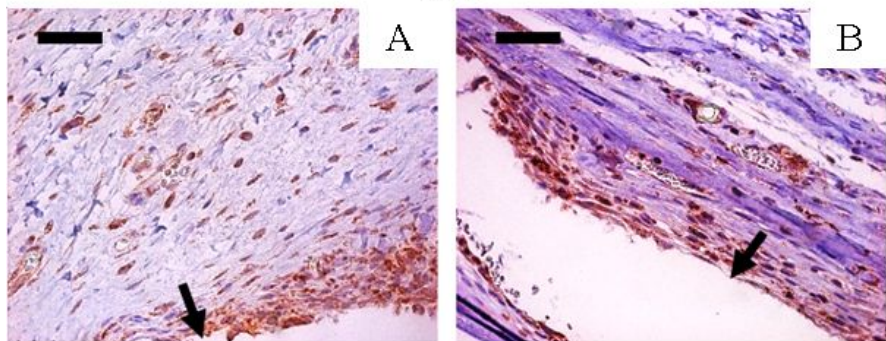
C

D

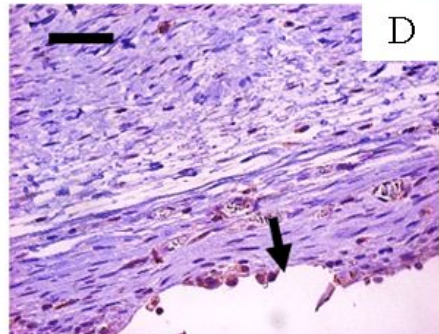


(b)

Week 4

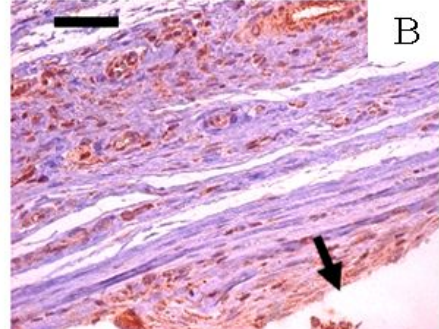


C

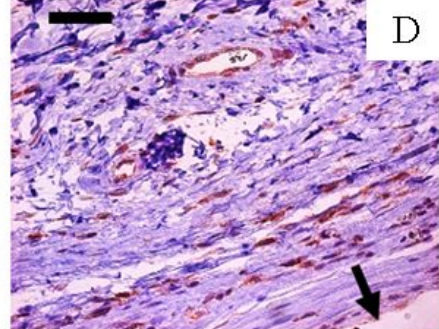


(c)  
Week 8

A



C



(d)

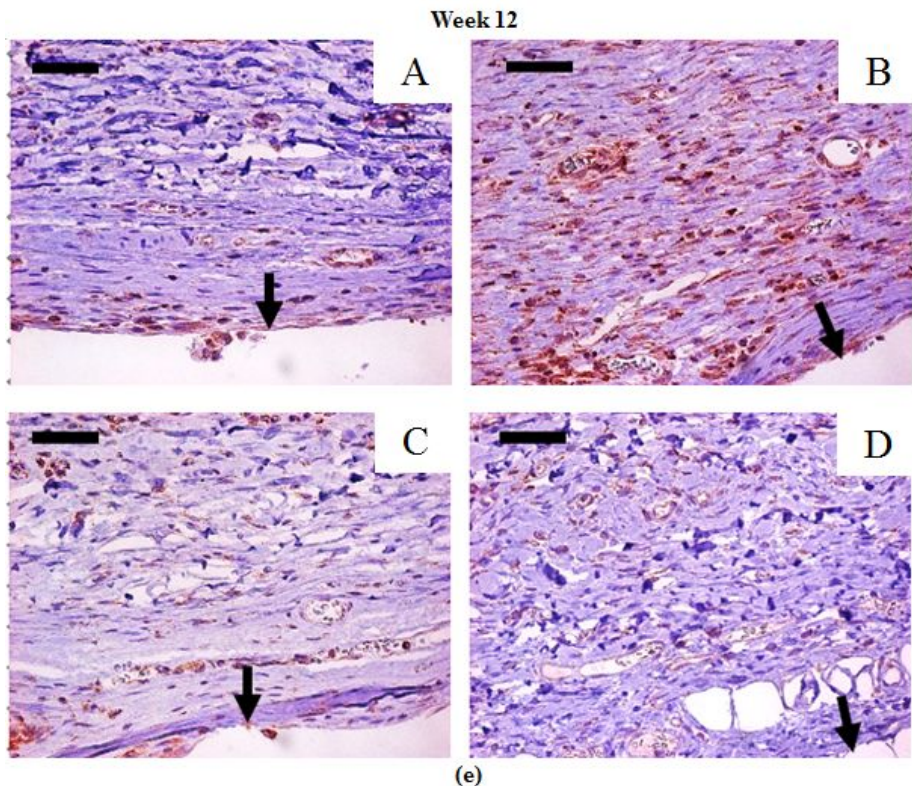
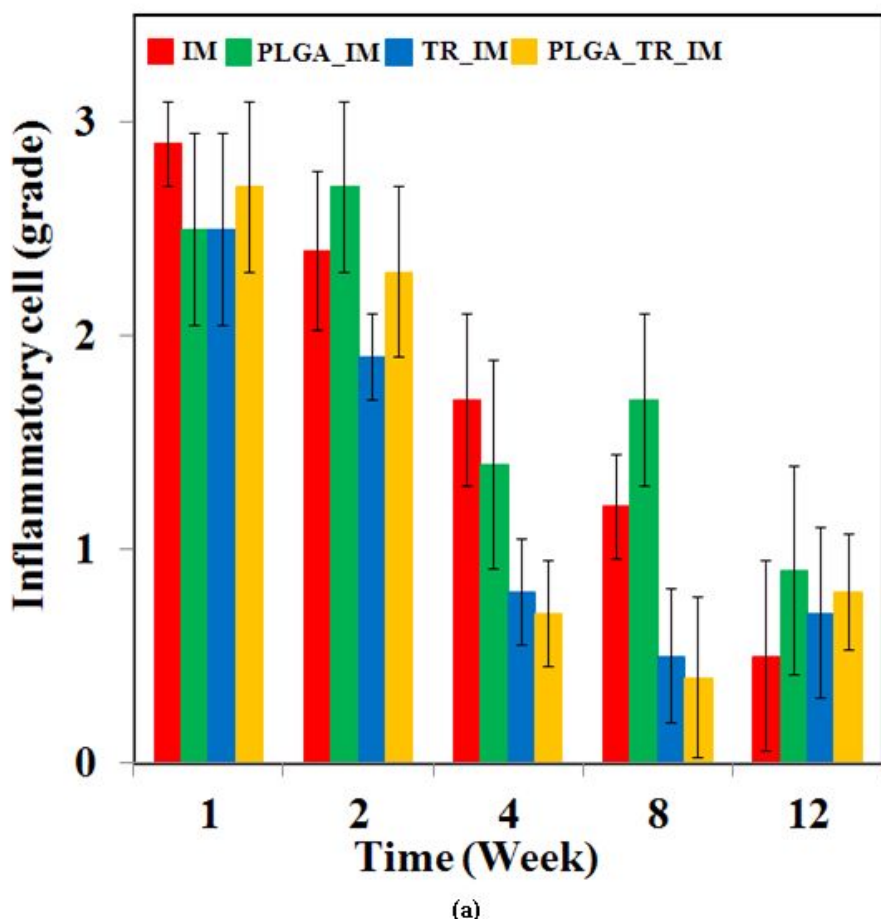
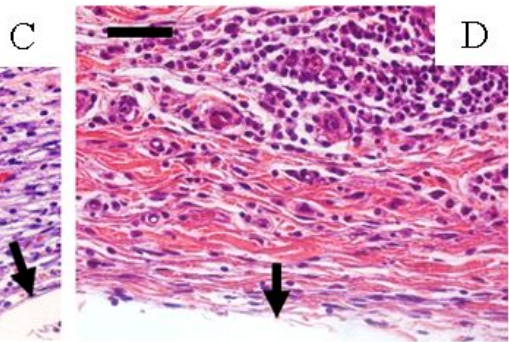
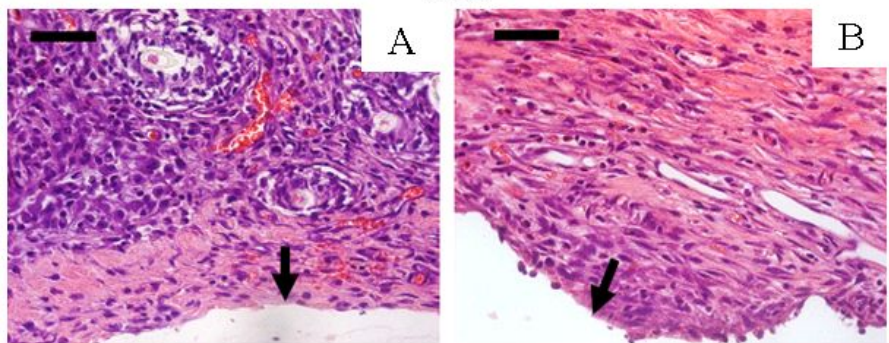


**Fig. 4.14 Representative images around the implants with IHC staining for evaluation of the TGF- $\beta$  expression.** The images were obtained from the (A) IM, (B) PLGA\_IM, (C) TR\_IM and (D) PLGA\_TR\_IM samples at (a) week 1, (b) week 2, (c) week 4, (d) week 8 and (e) week 12. Scale bars: 100  $\mu\text{m}$ . The arrow indicates the location of the implant in the image.

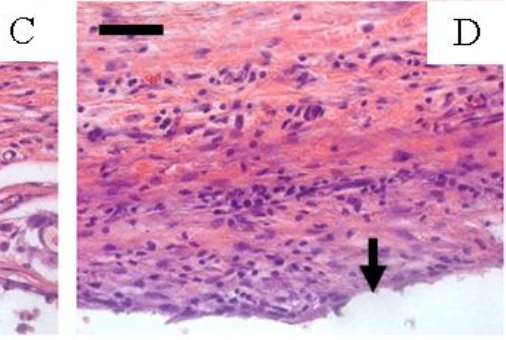
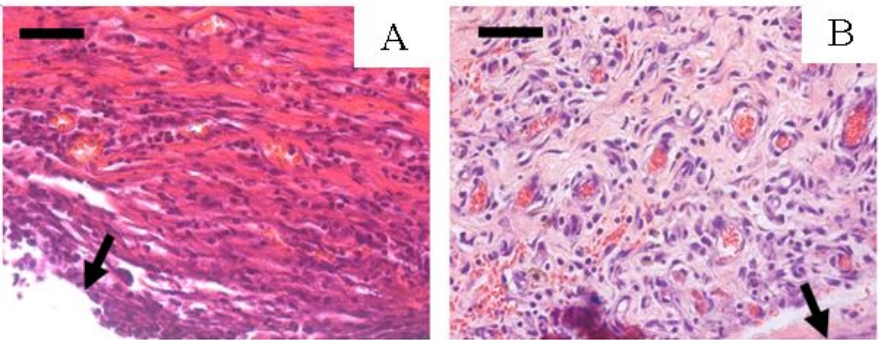


Week 1



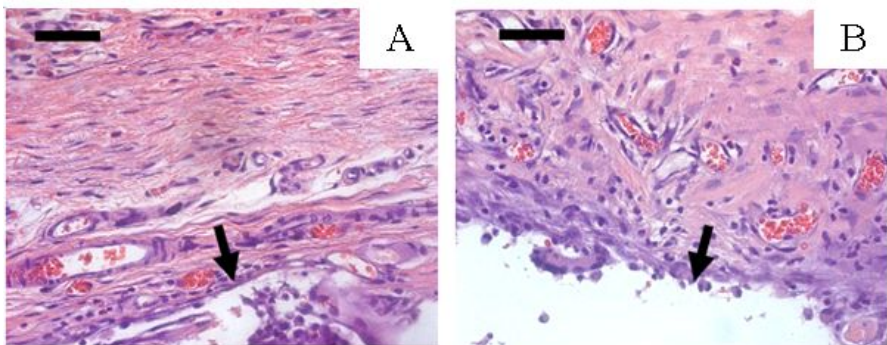
(b)

Week 2

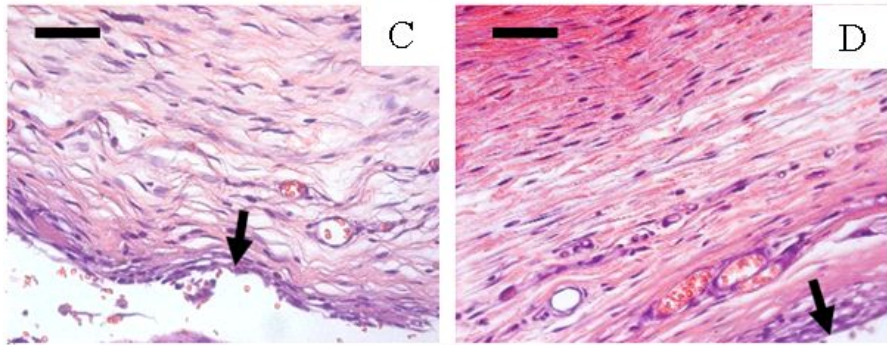


(c)

Week 4

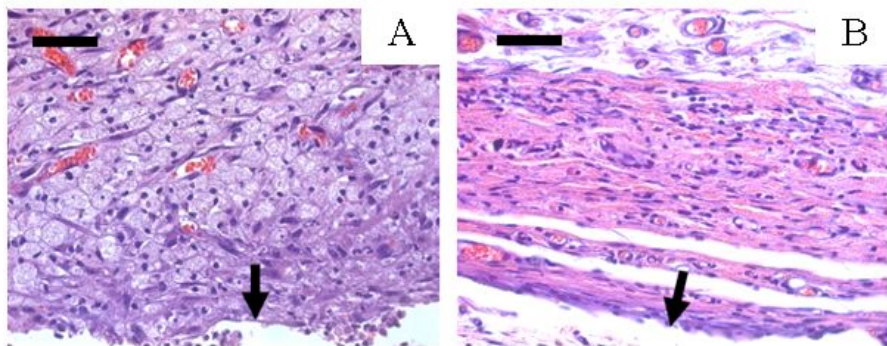


C

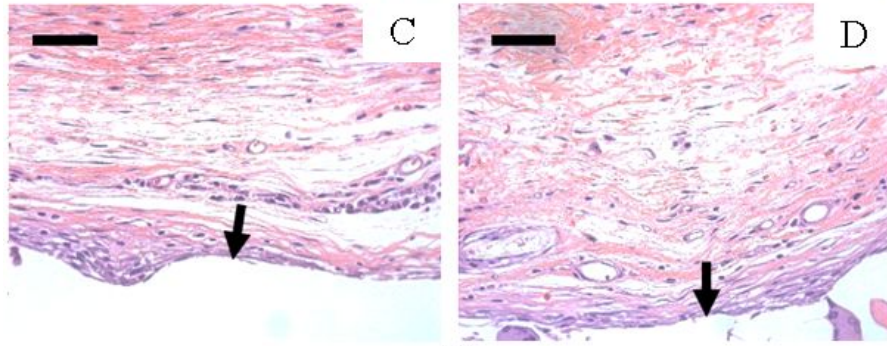


(d)  
Week 8

A



C



(e)

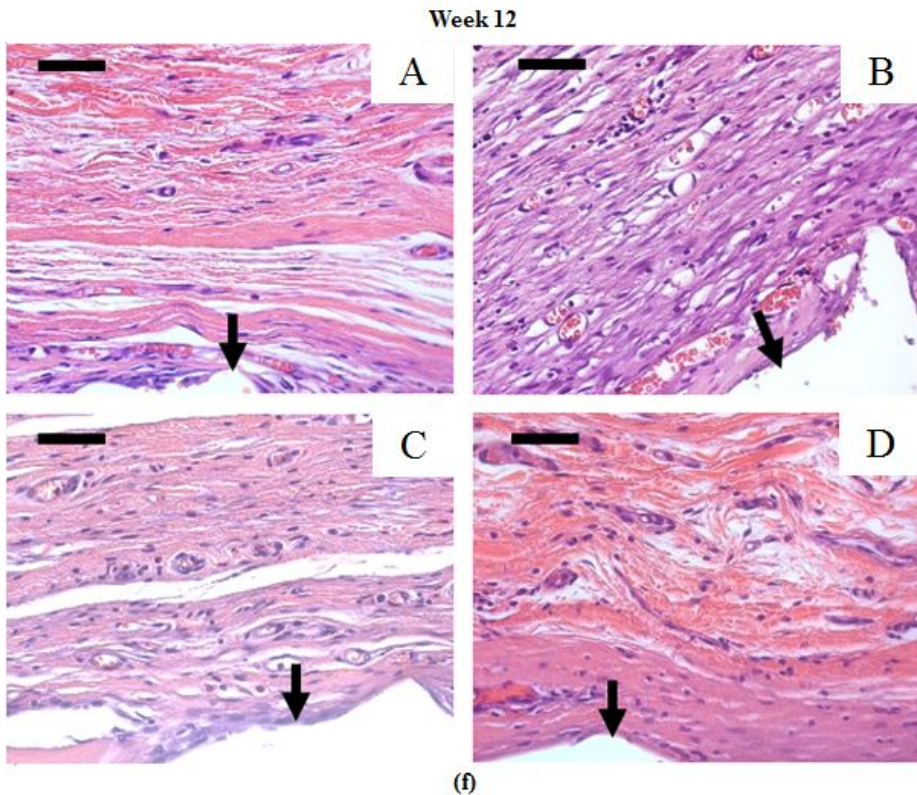


**Fig. 4.15 Evaluation of the acute inflammation around the implant with H&E staining.** (a) The degree of acute inflammation was semi-quantitatively evaluated according to the number of inflammatory cells, such as polymorphonuclear leukocytes (PMNs), with the analysis yielding the following grades: 0 (None), 1 (Mild), 2 (Moderate) and 3 (Severe). At each biopsy time and for each implant sample, five images were obtained from each of the five animals, giving a total of 25 images for statistical analysis. The representative images were obtained from the implants of (A) IM, (B) PLGA\_IM, (C) TR\_IM and (D) PLGA\_TR\_IM at (b) week 1, (c) week 2, (d) week 4, (e) week 8 and (f) week 12. Scale bars: 100  $\mu\text{m}$ . The arrow indicates the location of the implant in the image.

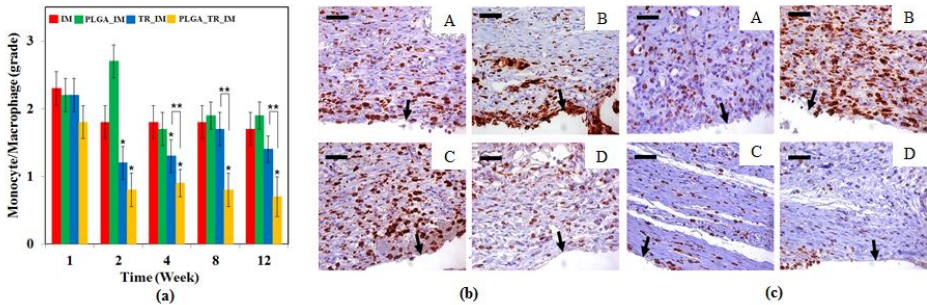
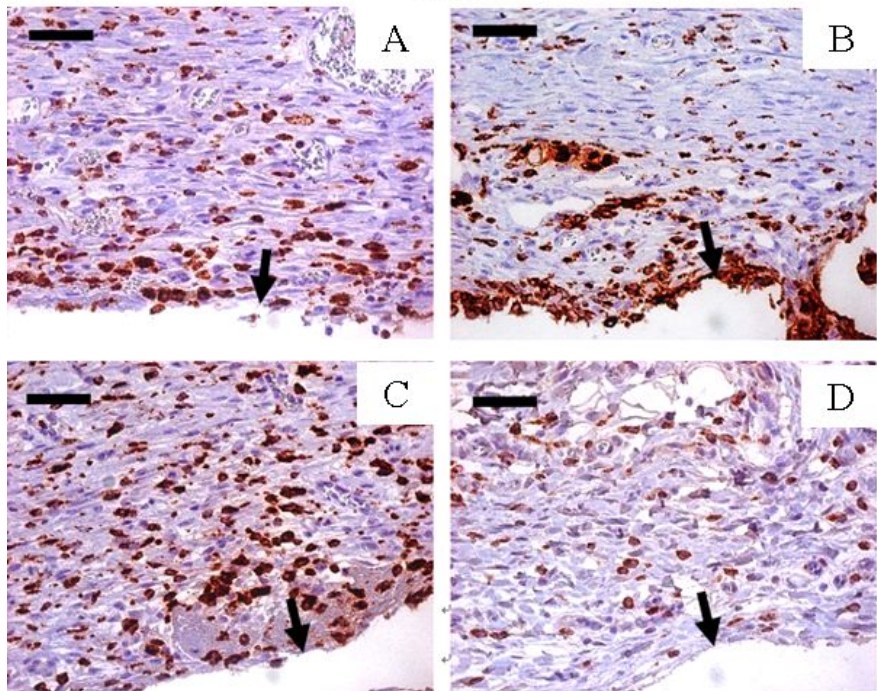
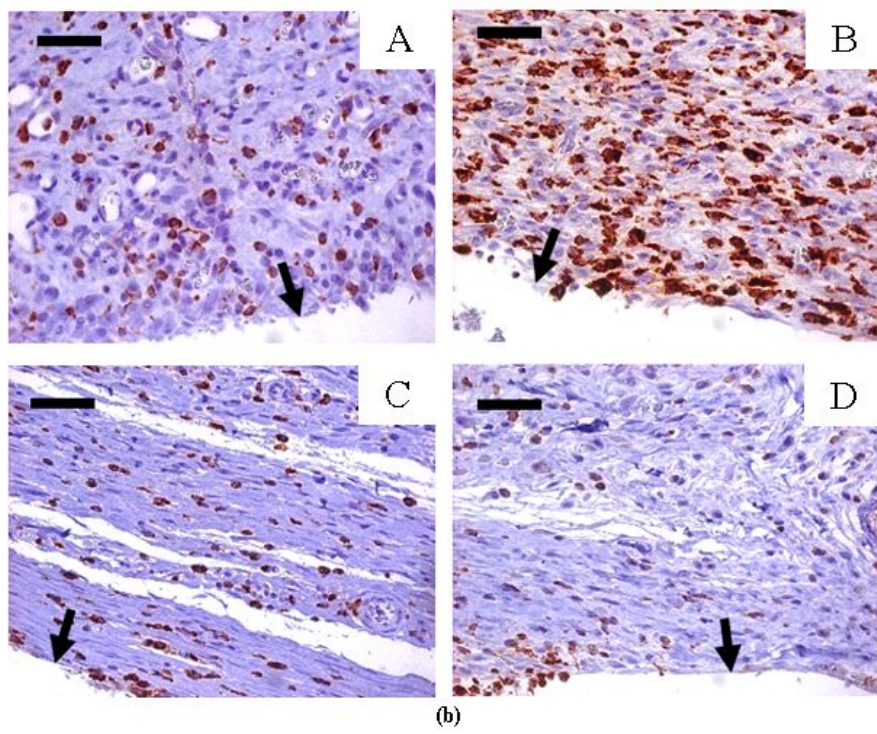


**Fig. 4.16** Evaluation of monocyte and macrophage quantity. (a) Mean grading scores of monocyte/macrophage quantity at each biopsied time and representative IHC images at (b) week 8 and (c) week 12. Scale bars: 100  $\mu\text{m}$ . The images were obtained from (A) IM, (B) PLGA\_IM, (C) TR\_IM and (D) PLGA\_TR\_IM samples, and the arrow indicates the location of the implant on the image. The asterisk (\*) represents a significant difference compared with the IM group ( $P < 0.05$ ). Double asterisks (\*\*) represent a significant difference between the TR\_IM and PLGA\_TR\_IM groups ( $P < 0.05$ ).

Week 1

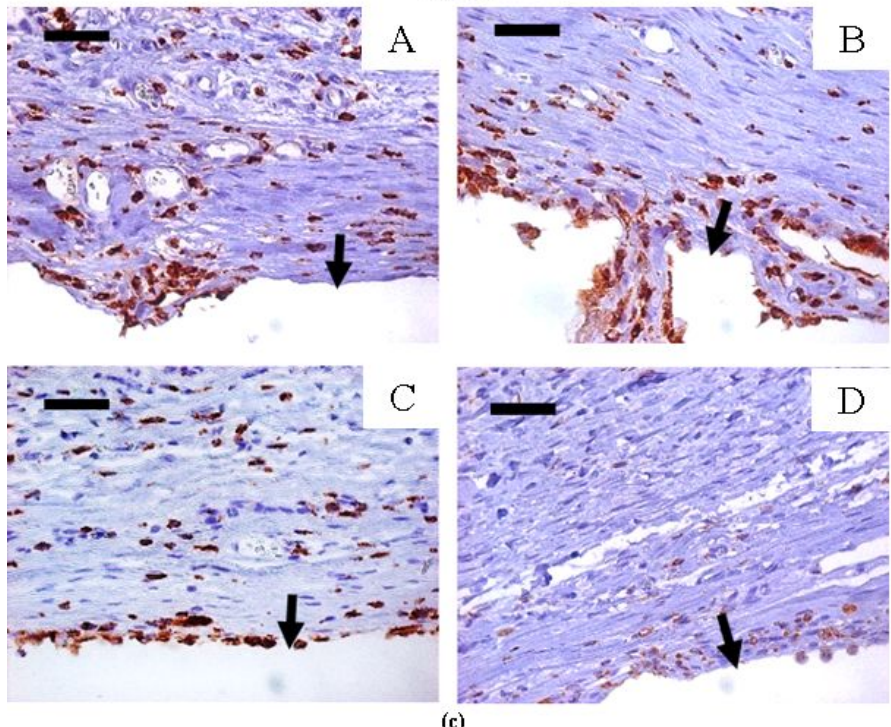


(a)  
Week 2

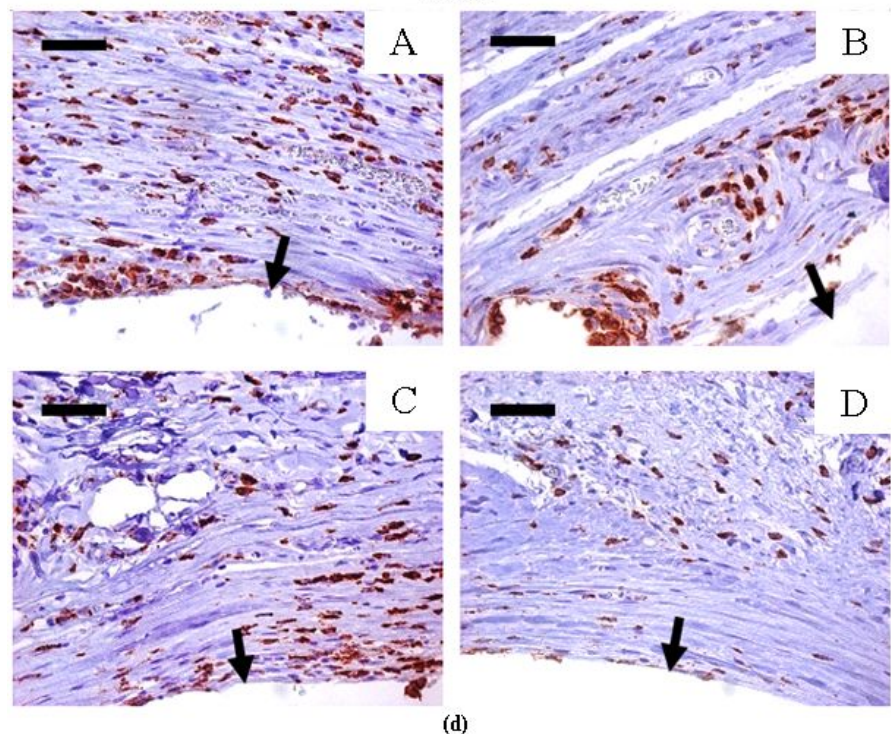


(b)

Week 4



Week 8



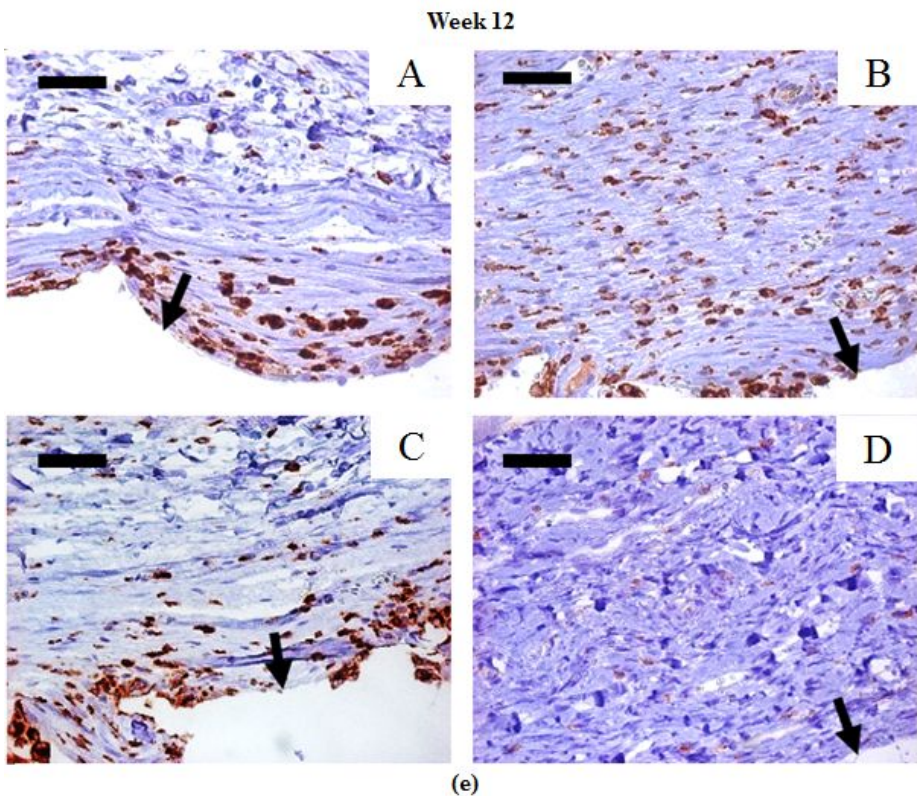


**Fig. 4.17 Representative images around the implants with IHC staining for evaluation of the monocyte/macrophage quantity.** The images were obtained from the (A) IM, (B) PLGA\_IM, (C) TR\_IM and (D) PLGA\_TR\_IM samples at (a) week 1, (b) week 2, (c) week 4, (d) week 8 and (e) week 12. Scale bars: 100  $\mu$ m. The arrow indicates the location of the implant in the image.

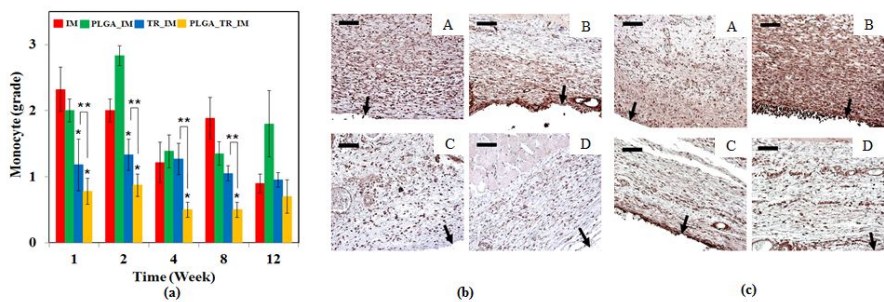
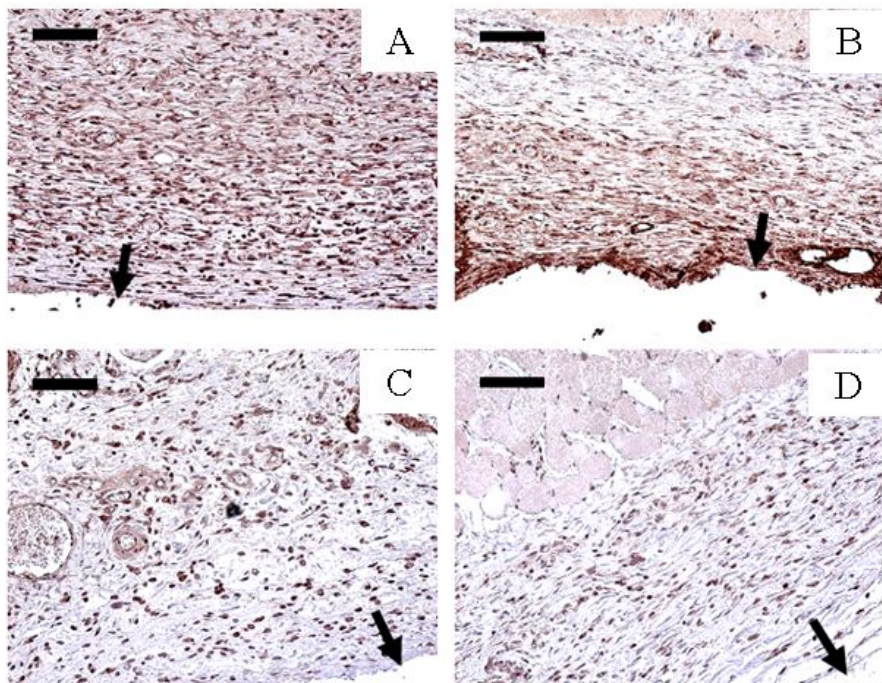
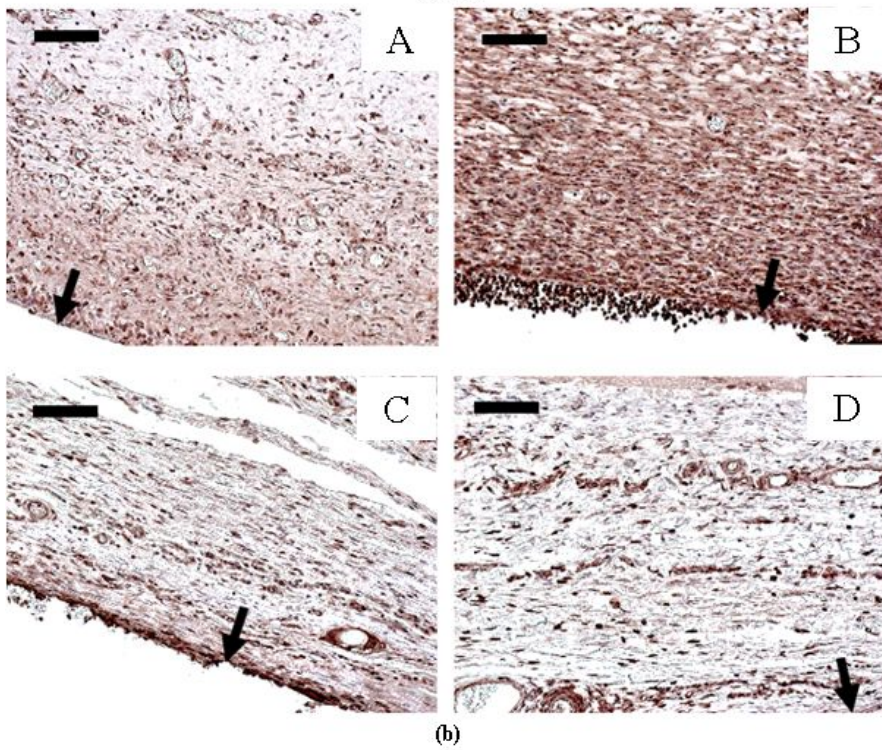


**Fig. 4.18** Evaluation of monocyte quantity. (a) Mean grading scores of monocyte quantity at each biopsied time and representative IHC images at (b) week 1 and (c) week 2. Scale bars: 100  $\mu$ m. The images were obtained from (A) IM, (B) PLGA\_IM, (C) TR\_IM and (D) PLGA\_TR\_IM samples, and the

Week 1

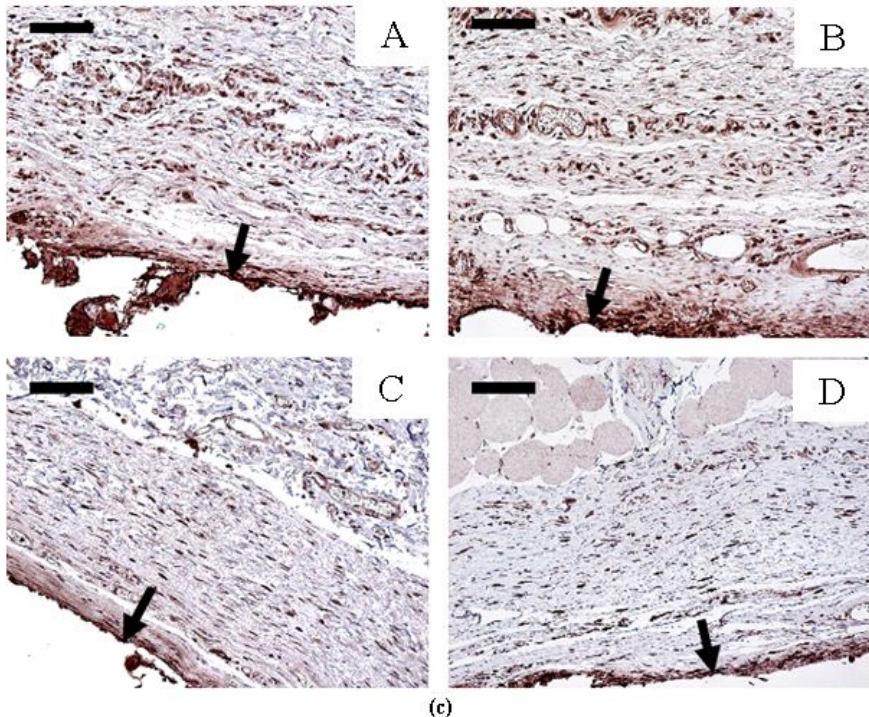


(a)  
Week 2



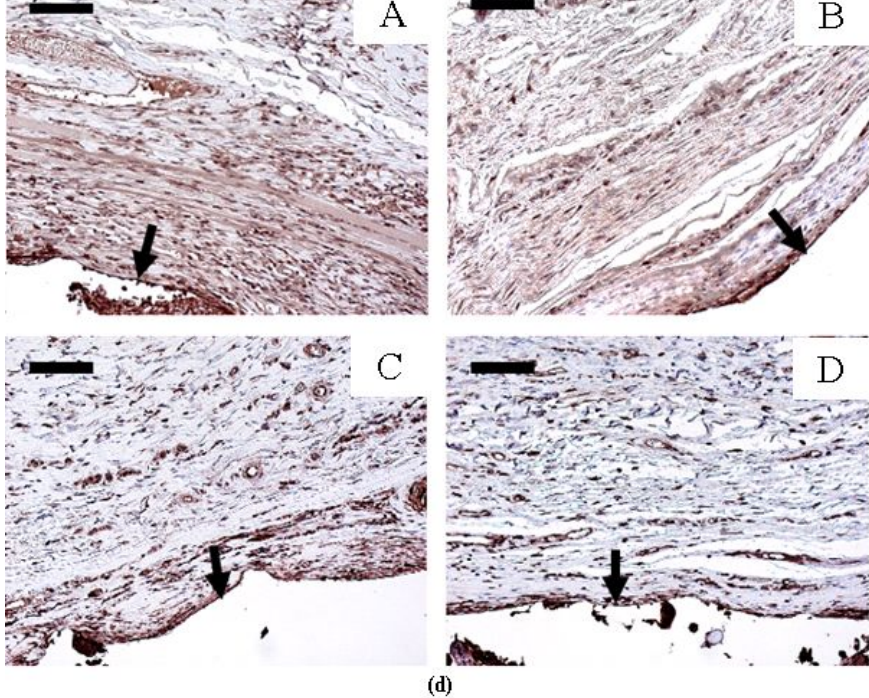
(b)

Week 4



(c)

Week 8



(d)

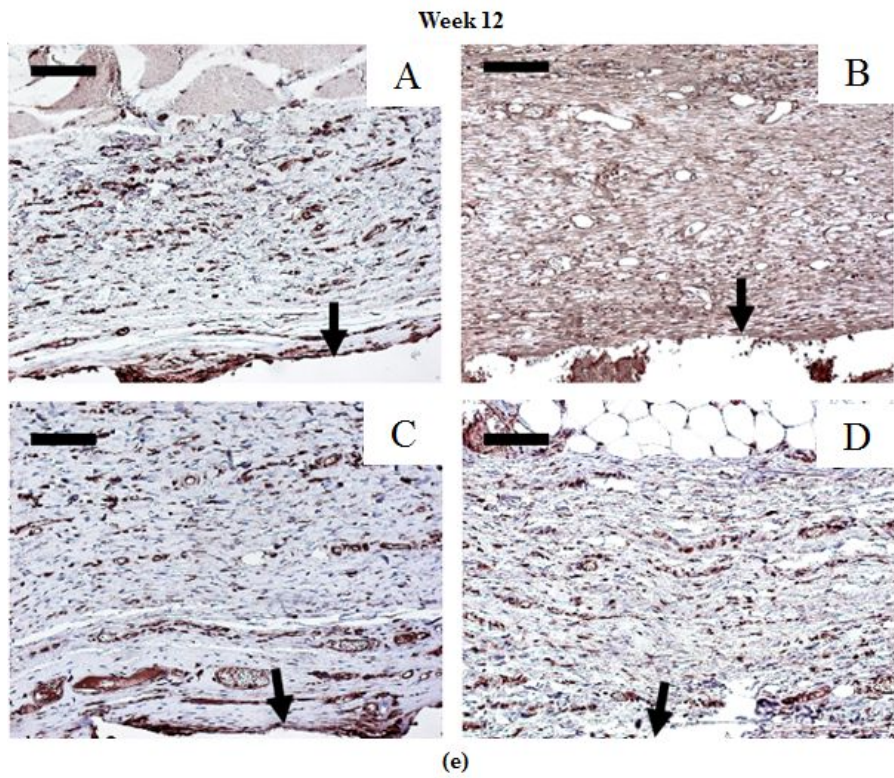


**Fig. 4.19 Representative images around the implants with IHC staining for evaluation of the monocyte quantity.** The images were obtained from the (A) IM, (B) PLGA\_IM, (C) TR\_IM and (D) PLGA\_TR\_IM samples at (a) week 1, (b) week 2, (c) week 4, (d) week 8 and (e) week 12. Scale bars: 100  $\mu$ m. The arrow indicates the location of the implant in the image.

# Chapter 5

## Bioabsorbable Bone Plates Enabled with Local, Sustained Delivery of Alendronate for Bone Regeneration

### 5.1 Introduction

Bone fixation systems made of biodegradable polymers, such as poly (lactic–co–glycolic acid) (PLGA), poly (lactic acid) (PLA) or poly (glycolic acid) (PGA), have attracted a great deal of interest as they would not need a secondary removal surgery

due to biodegradability (1, 116). The major compartments of the bone fixation systems are plates and screws, where the plate is positioned and fixed on a fractured bone by screws. In this way, the undesired motion of the fracture bone can be prevented until complete healing.

However, the bone fixation systems currently in clinical use do not have the functionality for treatment of the patients with bone diseases, such as osteoporosis. The osteoporotic patients often show low bone density, hence delayed bone healing (117). Because of this, failure of bone fixation systems is problematic with osteoporotic patients, causing severe complications, such as microfracture, malunion or loosening of the fixation system (7, 118). It has been reported that failure of bone fixation systems occur in 2 % to 10 % of fractures related to osteoporosis (7, 119). In this aspect, a strategy to facilitate bone healing is needed to properly treat fractured bone of the osteoporotic patients without failure of fixation system (13).

In this sense, alendronate can be a good candidate therapeutic agent to prevent failure of fixation system for osteoporotic patients. Alendronate has been already widely used for treatment of bone diseases, such as osteoporosis, Patget's disease or inflammation-related bone loss (120–122). The drug

is a significant potent inhibitor of bone resorption by preventing the recruitment and differentiation of osteoclasts (122, 123). Moreover, it is recently reported that the drug can improve the recruitment, differentiation and bone-remodeling activity of osteoblasts, thereby expediting bone repair (124–126). By these, the drug has been shown to increase bone mineral density, especially effective for treatment of osteoporosis(127).

Alendronate is often administered orally or via injection; however, when being orally administered, alendronate may induce irritation in the gastrointestinal (GI) tract, as well as abdominal pain and nausea (128). Given these, local delivery of alendronate can be a promising way of therapy. In a sense that a bone fixation system needs to be placed locally onto a fractured bone, a combined entity of bone fixation and drug delivery should be more advantageous. In addition, a sustained delivery of alendronate can benefit from continuous inhibition of bone resorption during bone healing (129–131), hence better improvement of bone density.

In this work, therefore, we prepared a bone fixation plate with the added functionality of local, sustained delivery of alendronate. For this, we employed a bone plate already in clinical use (PLT-1031, Inion, Finland) and coated it with 4-azidobenzoic acid-

modified chitosan (i.e., Az-CH) loaded with alendronate. Az-CH could be crosslinked via UV irradiation to serve as drug diffusion barrier for sustained delivery of alendronate (42, 132). In addition, crosslinked Az-CH can form covalent bonds with poly(lactic acid), one of the major constituents of the Inion plate (133, 134) and thus, the Az-CH based coating could be stably attached on the surface of the Inion plate. Az-CH is also proven to be biocompatible to a large extent (134, 135).

We characterized the coating with X-ray diffractometry (XRD) and Fourier transform infra-red spectroscopy (FTIR), and its morphology was examined by scanning electron microscopy (SEM). We also performed the *in vitro* drug release study in phosphate buffered saline (PBS; pH 7.4) at 37 °C with the plate coated with both Az-CH and alendronate. For *in vivo* evaluation, the plates were fixed on a craniotomy defect, 8 mm in diameter, created on the skull of living rats (136). The degree of reconstructed bone volume was quantitatively measured using microcomputed tomography (micro-CT) at predetermined schedules for 8 weeks following implantation. The histopathologic analyses were also carried out with the tissue including the implanted plate at 8 weeks after implantation on hematoxylin and eosin (H&E) staining.

## 5.2 Materials and Methods

### 5.2.1 Materials

4-azidobenzoic acid was obtained from Tokyo Chemical Industry (Tokyo, Japan). Chitosan (Mw; < 200 kDa, degree of deacetylation; 75~85%), N,N,N ,N -Tetramethylethylenediamine (TEMED), 1-ethyl-3-(3-dimethylaminopropyl)-carbodiimide (EDC), alendronate sodium trihydrate, acetic acid solution, O-Phthaldialdehyde (OPA), 2-Mercaptoethanol (2ME) and egg-white lysozyme were all purchased from Sigma-Aldrich (MO, USA). Phosphate buffered saline (PBS, pH 7.4) was obtained from the Seoul National University Hospital Biomedical Research Institute. Bioabsorbable bone fixation plates (PLT-1031) were purchased from Inion (Finland). Zolazepam and tiletamine (0.3 ml/kg; Zoletil®) were supplied from Virbac (France). xylazine (0.1 ml/kg; Rompun®) was obtained from Bayer (Germany). Betadine was obtained from Hyundai Pharm (Korea). The absorbable sutures (Vicryl 3-0; 6-0) used for animal surgery were supplied from Ethicon (NJ, USA).

### **5.2.2 Synthesis of an Azidobenzoic Acid–Modified Chitosan (Az–CH)**

Az–CH was synthesized as described in a previous study (135). In brief, a chitosan solution was first prepared with 200 mg chitosan dissolved in 15 ml distilled water adjusted to pH 4.75 using acetic acid solution. N,N,N ,N – Tetramethylethylenediamine (TEMED) (116.2 mg) was dissolved in 1 ml distilled water, which was then added to the chitosan solution. To this resulting solution, a mixed solution of 70 mg 1–ethyl–3–(3–dimethylaminopropyl)–carbodiimide (EDC) in 1 ml distilled water and 40 mg 4–azidobenzoic acid in 1 ml dimethyl sulfoxide was then added. After adjusting the pH at 5 with 1 M HCl, the reaction was carried out at room temperature overnight. The solution was filtered via a 0.22  $\mu$ m–pore filter (GSPW04700, Millipore, Bedford, MA), which was then freeze–dried for 3 days to give a dry powder of Az–CH.

### **5.2.3 Preparation of Bone Plate Samples**

We prepared the three different types of bone plate samples in

this work:

- (1) The IP : intact bone plates with no treatment
- (2) The Az-CH\_P: bone plates coated with Az-CH only
- (3) The AL-Az-CH\_P: bone plates coated with Az-CH and alendronate

As shown in Fig. 5.1, we first cut a whole piece of an Inion bone plate (PLT-1031) into the square-shaped pieces (6 mm x 6 mm), each with a screw hole at the center. These pieces were each used as IP sample without further treatment. To prepare the coated sample, i.e., Az-CH\_P or AL-Az-CH\_P, the coating solution was first prepared: 20 mg Az-CH or a blend of 20 mg Az-CH and 25 mg alendronate was dissolved in 1 ml of 2 % v/v acetic acid solution, respectively. Then, four drops of the coating solution (3  $\mu$ l per drop) were added on top of the intact plate around the screw hole at the center, as described in Fig 5.1(A). The coated samples were each placed under UV irradiation (100 W; 365nm, Black-Ray, UVP, USA) for 5 min to crosslink Az-CH, which were then dried at room temperature for 24 h in darkroom (Fig. 5.1(B)). For *in vivo* experiments and mechanical property evaluation, we cut the Inion plate with a piece containing three screw holes, as depicted in Fig. 5.2. The outer two holes were

used to suture and fix the plate on a bone for *in vivo* experiments or employed as sites for clamping for mechanical property evaluation. Thus, the coatings were made in the same way as described above, only around the screw hole in the middle.

#### 5.2.4 Characterizations of Az-CH

To confirm the formation of Az-CH with the method employed in this work (135), we performed spectrophotometric analysis. For this, the solutions of Az-CH, chitosan and 4-azidobenzoic acid were each prepared: 20 mg Az-CH or 20 mg chitosan was completely dissolved in 1 ml of 2% acetic acid solution, respectively and 4-azidobenzoic acid (4 mg) was dissolved in 1 ml methanol. Then, we obtained the UV spectra of the resulting three solutions at the wavelengths from 250 nm to 400 nm (UV-1800, Shimadzu, Japan). To further confirm the formation of Az-CH, we also performed Fourier transform infrared (FTIR) analysis. For this, Az-CH, chitosan and 4-azidobenzoic acid were each milled with potassium bromide (KBr) to produce a fine power, which was then compressed into a thin pellet.

### **5.2.5 Plate Characterizations**

The surface of the coating on the plate samples (i.e., AL-Az-CH\_P) was examined and compared with that of the noncoated, intact surface, using a scanning electron microscope (SEM; 7501F, Jeol, Japan). Prior to imaging, the sample was placed on the SEM specimen mount and sputter coated with platinum for 5 min. (208HR, Cressington Scientific, England). We also conducted FTIR analysis (JASCO 6100, Japan). To do this, each plate sample was milled with potassium bromide (KBr) to produce a fine powder and then compressed into a thin pellet for analyses. The intact Az-CH and alendronate were also analyzed for comparison.

### **5.2.6 Mechanical Property Evaluation**

To examine the mechanical property after coating, we measured the ultimate tensile strength (UTS) of the plate samples, i.e., IP, Az-CH\_P and AL-Az-CH\_P (Fig. 5.2). The plate samples were each loaded in a universal testing machine (UTM; Instron-5543, MA, USA) equipped with a load cell of 71 kN, where both ends of the sample were clamped and pulled at a rate of 3 mm/min

until break (137).

### 5.2.7 Measurement of Drug–Loading Amount

The amount of alendronate in the coating was measured, following the method as previously employed (138). In brief, 50 mg O–Phthaldialdehyde (OPA) was fully dissolved in 5 ml of an aqueous solution of 0.05 M NaOH, where 250  $\mu$ l of 2–Mercaptoethanol (2ME) was added. Then, the solution was transferred to 50 ml volumetric flask, which was then fully filled with a 0.05 M NaOH solution to give a derivatizing reagent solution (OPA/2ME). The coating was completely scratched off from the AL–Az–CH\_P, which was then immersed in 2 ml of a lysozyme solution (4 mg/ml) at 37° C while being agitated at 50 rpm for 72 h to fully disintegrate Az–CH. To this 2 ml solution, a mixture of the derivatizing reagent solution (OPA/2ME; 0.8 ml) and NaOH solution (0.05 M; 7.2 ml) was added. After 60 min, the absorbance of the resulting solution was measured spectrophotometrically (UV–1800, Shimadzu, Japan) at a wavelength of 333 nm. The experiments were performed in triplicate.

### **5.2.8 *In vitro* Drug Release Study**

The AL-Az-CH\_P was immersed in 2 ml of phosphate buffered saline (PBS, pH 7.4) at 37° C, which was continuously agitated at 125 rpm in a shaking incubator (SI-300, JEO TECH, Korea). At scheduled times for 77 days, a whole 2 ml release medium was collected and an equal amount of the same fresh medium was added back. The sampled media were each measured by the spectrophotometric method as described above. The experiments were performed in triplicate.

### **5.2.9 *In Vitro* Cell Cytotoxicity Evaluation**

The L929 mouse fibroblasts cell line (Korean Cell Line Bank, Korea) was used to assess the cytotoxicity of the plate samples prepared in this work. The fibroblasts were grown in RPMI-1640 medium (WelGENE, Korea) supplemented with 10 % fetal bovine serum (Gibco, Life Technologies, UK) and 1 % antibiotic (penicillin, 10,000 U ml<sup>-1</sup>; Gibco, Life Technologies, UK) in an atmosphere of 5 % CO<sub>2</sub> in air and 100 % relative humidity. All samples were sterilized prior to the test using ethylene oxide gas. The samples were each placed in a 24-well cell culture

plate where the L929 fibroblasts were prepared at a density of  $2.0 \times 10^4$  cells/well. After incubation in a humidified atmosphere with 5 % CO<sub>2</sub> at 37 °C for 24 h (HERAcell 150i, Thermo Scientific, USA), the samples were each washed with distilled water to fully remove the non-adhered cells. Afterwards, the adhered cells on the coating were quantitatively investigated with the EZ-Cytotoxicity Cell viability assay kit, following the manufacturer's instruction (No. EZ-1000, DAEILAB SERVICE co., Ltd, Korea) (139). The absorbance was measured at 450 nm using a microplate reader (VERSA max, Molecular Devices, USA).

#### **5.2.10 *In Vivo Animal Study***

For *in vivo* evaluation of the plate samples, we used 8-week-old male SD rats weighing 250 – 300 g (Koatech, Keung-Ki, Pyong-Taek, Korea). The rats were cared and housed, following the protocol approved by the Institutional Animal Care and Use Committee (IACUC No. 13-0100) at Seoul National University Hospital. The rats were provided with food and water ad libitum. To examine the bone regeneration effect, we first created the calvarial bone defect in rats as previously reported (140).

Anesthesia was performed by intramuscular injection of a cocktail of zolazepam and tiletamine (0.3 ml/kg; Zoletil®, Virbac, France), and xylazine (0.1 ml/kg; Rompun®, Bayer, Germany). Then, the hair on the head was clearly shaved, followed by cleaning with Betadine® (Hyundai Pharm, Korea) and the calvarial bone was exposed through a skin incision, 5 cm in length. A craniotomy defect, 8 mm in diameter, was created with a trephine (TPHB-B8, Osung, Korea). To fix the plate in place, two holes for suturing, 10 mm in diameter, were also made by drilling, each of which was located 2 mm away from the boundary of a defect. The surgical area was washed with saline to fully remove bone debris. The plate sample was placed on the calvarial bone defect with the coated side facing on the defect. Then, the plate was fixed with bioabsorbable suture (Vicryl 3–0, Ethicon, NJ, USA) through the outer two holes made for suturing (Fig. S1). Then, the incised skin was closed with bioabsorbable suture (Vicryl 3–0, Ethicon, New Jersey, USA) and a post-operative dressing was applied with Betadine®.

According to the types of the implanted samples, the animals were divided into four groups.

- (1) The no treatment group: the animals without the plate
- (2) The IP group: the animals implanted with the IP

(3) The Az-CH\_P group: the animals implanted with the Az-CH\_P

(4) The AL-Az-CH\_P group: the animals implanted with the AL-Az-CH\_P

At least five animals were employed for each of the implant groups. To evaluate new bone formation after implantation, the image from the bone defect was obtained via micro-computed tomography (micro-CT; NFR Polaris-G90, In-vivo Micro-CT, NanoFocusRay, Korea) at schedule times for 56 days: the scanner with a voltage of 20–90 kV and the current of 180  $\mu$ A were used and the voxel size after reconstruction was 9  $\mu$ m. At the time for imaging, the animal was sedated with an intramuscular injection of Zoletil® (0.3 mg/ml). From each of the micro-CT images, the new bone volume percent was calculated by dividing the volume of newly formed bone by that of the initially created defect, using the AMIRA software (Version 5.4, ZIB & Visage Imaging, Germany).

### 5.2.11 Histopathologic Evaluation

At 8 week after plate implantation, the animal was sacrificed with carbon dioxide and the specimen including the bone defect

and plate sample was biopsied. The specimen was fixed in 10 % (v/v) buffered neutral formalin for 3 days, which was then embedded with resin, sectioned into 30 – 40  $\mu\text{m}$ -thick slides (BS-3000N, EXAKT, Germany) and stained with hematoxylin and eosin (H&E). The slides were examined under an optical microscope (BX53F, OLYMPUS, Japan) with X40 and X100 magnifications for histopathologic evaluation by a professional pathologist.

### 5.2.12 Statistics

Mean percentages of new bone volumes among the four different animal groups were statistically analyzed with one-way ANOVA with  $\alpha = 0.05$  followed by pairwise comparisons using a Tukey's post hoc test (GraphPad Prism, version 5.01, USA).  $P < 0.05$  was considered statistically significant.

## 5.3 Results

### 5.3.1 Characterizations of Az-CH

To confirm the formation of Az-CH, we assessed the UV spectra of Az-CH, chitosan and 4-azidobenzoic acid, as shown in Fig. 5.3(A). For 4-azidobenzoic acid, an apparent peak at 266 nm was ascribed to the N<sub>3</sub> group. This peak was also observed for Az-CH with a shift to 272 nm although the chitosan did not show any characteristic peaks in the spectrum (133). This indicated that the reaction between a free amino group of the chitosan and a carboxyl group of 4-azidobenzoic acid indeed occurred to introduce the N<sub>3</sub> group to the chitosan (134). To further confirm this, we also assessed the FTIR spectra. As shown in Fig. 5.3(B), a characteristic peak at 2127 cm<sup>-1</sup> was observed with 4-azidobenzoic acid due to the N<sub>3</sub> group. This peak was not seen with chitosan but appeared with Az-CH, indicating again the introduction of the N<sub>3</sub> group to the chitosan, giving Az-CH.

### 5.3.2 Characterizations of Plate Samples

Fig. 5.4 showed the scanning electron micrographs of the noncoated and coated surfaces of the AL-Az-CH\_P. The noncoated, intact surface was observed to be smooth with almost no micro-cracks or -defects (Fig. 5.4(A)). On the other hand,

the rough, wrinkled surface was observed on a coated surface (Fig. 5.4(B)), which appeared to be created while the coating solution was dried to leave the dry Az-CH. The surface morphology was not very different regardless of the presence of alendronate.

We also evaluated the FTIR spectra of the plate samples to investigate the presence of either alendronate or Az-CH in the coating, as shown in Fig. 5.5. For the IP, the double bands near  $2960\text{ cm}^{-1}$  and  $3000\text{ cm}^{-1}$  were ascribed to the C-H stretching in methane group (141). For Az-CH, the characteristic peaks were seen at wavelengths of  $1320\text{ cm}^{-1}$  and  $2127\text{ cm}^{-1}$ , which were due to the C-O-N and N<sub>3</sub> group (134, 142), respectively. For alendronate, the characteristic peak at  $1022\text{ cm}^{-1}$  was due to an asymmetric vibration of the P-OH group (143). On the FTIR spectrum of the coated plate sample, i.e., the Az-CH\_P or AL-Az-CH\_P, the characteristic peaks from each of the constituents, i.e., the IP and Az-CH, or the IP, Az-CH and alendronate, respectively, were observed to be overlapped without a major peak shift, implying the presence of all constituents without particular interactions among them.

The mechanical strength of the bone plate is important; the plate is designed to be strong enough to fix a fractured bone

until healing (144). Therefore, we sought to compare the ultimate tensile strength (UTS) of the plate, already approved in clinical use (i.e., the IP) with that of the coated plates (i.e., Az-CH\_P and AL-Az\_CH\_P). As shown in Fig. 5.6 and Table 5.1, the UTS did almost not vary after coating, suggesting that the inherent mechanical property of the bone plate could be retained even after coating with the method employed in this work.

### 5.3.3 *In Vitro* Drug Release Profile

For the AL-Az-CH\_P, the loading amount of alendronate was measured to be  $293.84 \pm 8.04 \mu\text{g}$  per plate (i.e.,  $73.46 \pm 2.01 \mu\text{g}$  per coating). According to the *in vitro* drug release study, the drug was released in a sustained manner for 63 days (Fig. 5.7). Drug release was relatively fast during the first seven days with an approximate rate of  $15.56 \mu\text{g}/\text{day}$ , which slowed down to the rate of  $2.6 \mu\text{g}/\text{day}$  for the rest 56 days.

### 5.3.4 Cytotoxicity

To evaluate the cytotoxicity of the coatings, we quantitatively analyzed the number of cells adhering to the surface of the plate

samples, as shown in Fig. 6. The amount of adhered cells was not significantly different among the plate samples of the IP, Az-CH\_P and AL-Az-CH\_P. Considering that the IP, an Inion bone plate in clinical use, is already proven to be safe to a large extent, the result suggested that the coatings prepared in this work be also not cytotoxic.

### 5.3.5 *In Vivo* New Bone Formation

To examine the efficacy of the alendronate-release coating, we investigated the degree of *in vivo* new bone formation within the calvarial bone defect, using micro-CT (Fig. 5.9). For all animal groups, the average value of new bone volume percent increased as the time elapsed. However, the degree of new bone formation was slow with the animal groups without alendronate (i.e., the no treatment, IP, Az-CH\_P groups), where the new bone volume percent increased to at most 14 – 24 % at 8 weeks and at all schedule times of imaging, their values were not statistically significantly different. In contrary, the increase in new bone was evident with the AL-Az-CH\_P group. At 4 weeks, the new bone volume percent was  $36.39 \pm 5.58\%$ , which increased further to  $52.78 \pm 6.84\%$  at 8 weeks. Notably, the average value of new

bone volume percent was statistically significantly higher with the AL-Az-CH\_P group from 4 weeks than those with the other different animal groups ( $p<0.05$ ).

### 5.3.6 Histopathologic Evaluation

We performed histological evaluation of the tissue in the calvarial bone defect on H&E staining at 8 week after implantation, as shown in Fig. 5.10. In the no treatment group, only a few new bone tissues were observed at the center and edge of the calvarial bone defect. With the IP and Az-CH\_P groups, fibrous tissues were seen to be formed around the plate samples while newly formed bone tissues were scarce. In contrast, in the AL-Az-CH\_P group, the new bone tissues were observed to cover most of the surface of the plate sample, lining through both center and edges of the calvarial bone defect.

## 5.4 Discussion

In this work, we suggested a bone plate enabled with a therapeutic ability potentially advantageous for treatment of osteoporosis. For this, we prepared a proof-of-principle device,

i.e., a bone plate coated with Az-CH loaded with a drug, alendronate. Alendronate is known to stimulate the recruitment and differentiation of osteoblasts as well as inhibits bone resorption, thereby facilitating new bone formation (120, 125). In this reason, local, sustained delivery of alendronate could be a promising way to expedite bone reconstruction. In this work, the AL-Az-CH\_P showed sustained drug release from the coating for 63 days at an average rate of about 4.0 µg/day (Fig. 5.7), the dose of which should be therapeutically effective in bone regeneration as many previous studies reported (145–147). As a result, for the bone defect animal models herein, the *in vivo* new bone formation was shown to be enhanced with the AL-Az-CH\_P, as compared with the plate samples without alendronate (Fig. 5.9 and Fig. 5.10).

In this work, we employed a modified form of chitosan, i.e., Az-CH as coating material. For the chitosan-based materials, to properly serve as drug diffusion barrier, chemical crosslinking is often incorporated, using an agent, such as glutaraldehyde (148). However, this process requires a comparably long-time reaction in an aqueous environment, which may degenerate the mechanical property of the bone plate, originally needed for bone fixation. Unlike this, the Az-CH could form a crosslinked

network via UV irradiation in a short period of time (5 min) to achieve prolonged delivery of alendronate (132, 148, 149). This could be ascribed to the fact that a combination of the relatively strong hydrogen bonding and the electrostatic interaction between alendronate and chitosan led to release of the drug in a sustained manner (130, 150). Thus, the plate did not need to be exposed to an aqueous environment for a long time. Because of this, the plates herein appeared to retain their mechanical property even after coating (Table 5.1. and Fig. 5.6). Moreover, the Az-CH was shown to be not cytotoxic in this work (Fig. 5.8), which could be supported by many previous reports (133, 135)

Alendronate is usually prescribed for oral administration (151); however, it has been reported that a long-term use of alendronate could induce adverse gastrointestinal side effects and thus, there is a recommended daily dose limitation (152). Previously, the systems for local delivery of alendronate have been suggested in forms of scaffold (130), graft (153) and particles (131, 154) and evaluated to be effective to a large extent. However, for treatment of bone fracture, those may require an additional procedure to apply the system to the defected bone before or after implanting the bone fixation system during surgery. In this sense, a combined entity of the

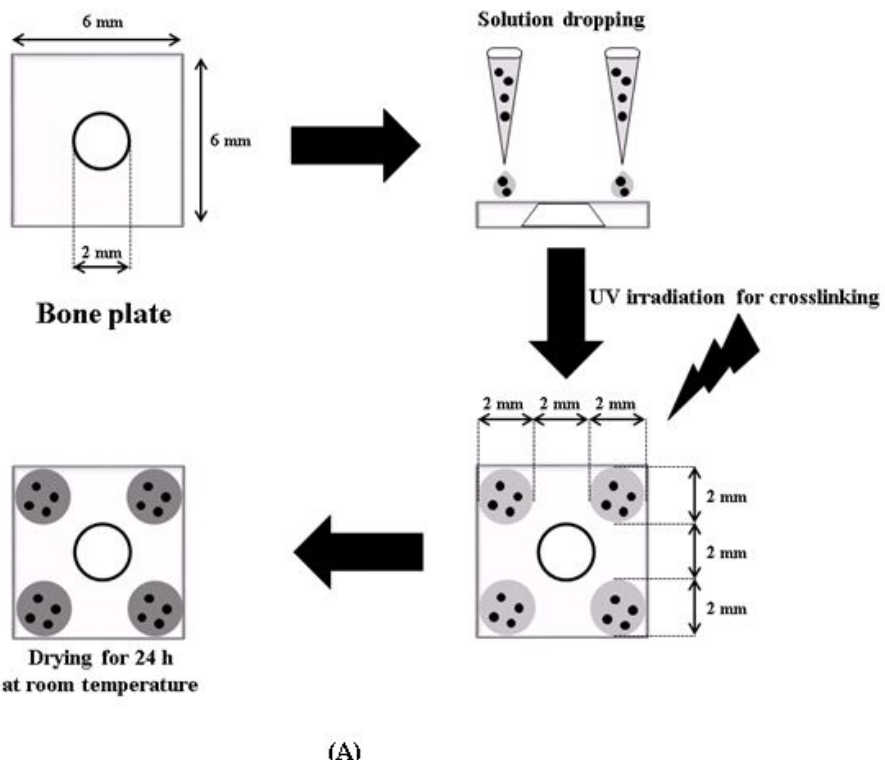
bone plate and drug delivery coating suggested in this work could be considered practically advantageous.

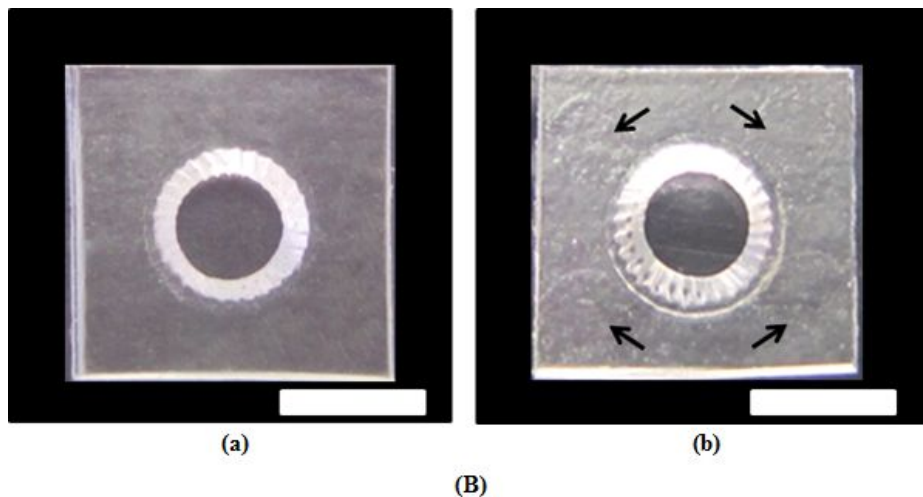
## 5.5 Conclusion

In this work, we suggest a bone plate enabled with therapeutic functionality of expedited bone regeneration. To realize this, a bone plate already in clinical use was coated with photo-crosslinked Az-CH loaded with a drug, alendronate. In this work, the drug could be released from the coating for about 63 days in a sustained manner, maintaining a therapeutically effective drug level. Therefore, when this alendronate-delivery plate was fixed on a cranial critical size defect *in vivo*, a statistically significantly higher volume of newly formed bone was observed than those with the plates without the drug. The alendronate-delivery plate also exhibited good *in vivo* biocompatibility, similar to the Inion plate already in clinical use. Therefore, we conclude that a bone plate enabled with sustained, local delivery of alendronate can be a promising system for both bone fixation and its expedited repair.

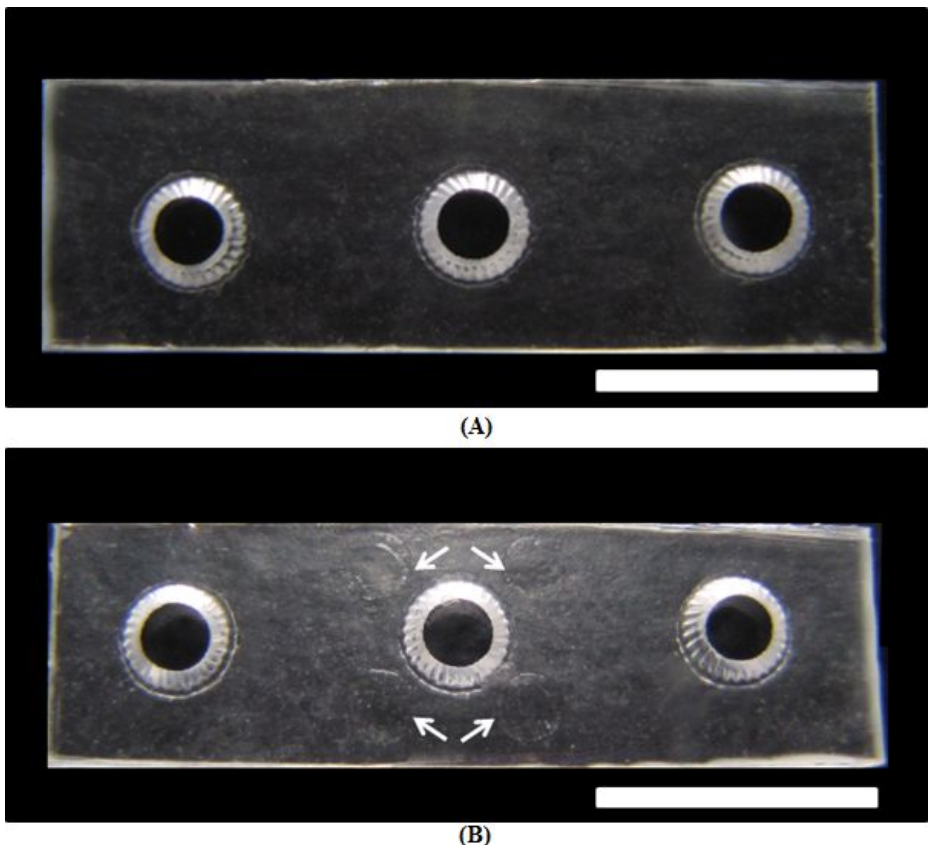
Sample Types	Ultimate Tensile Strength (MPa)
IP	20.24 ± 2.11
Az-CH_P	19.78 ± 1.78
AL-AZ-CH_P	20.27 ± 1.22

**Table 5.1** Mechanical property of the plate samples prepared in this work.

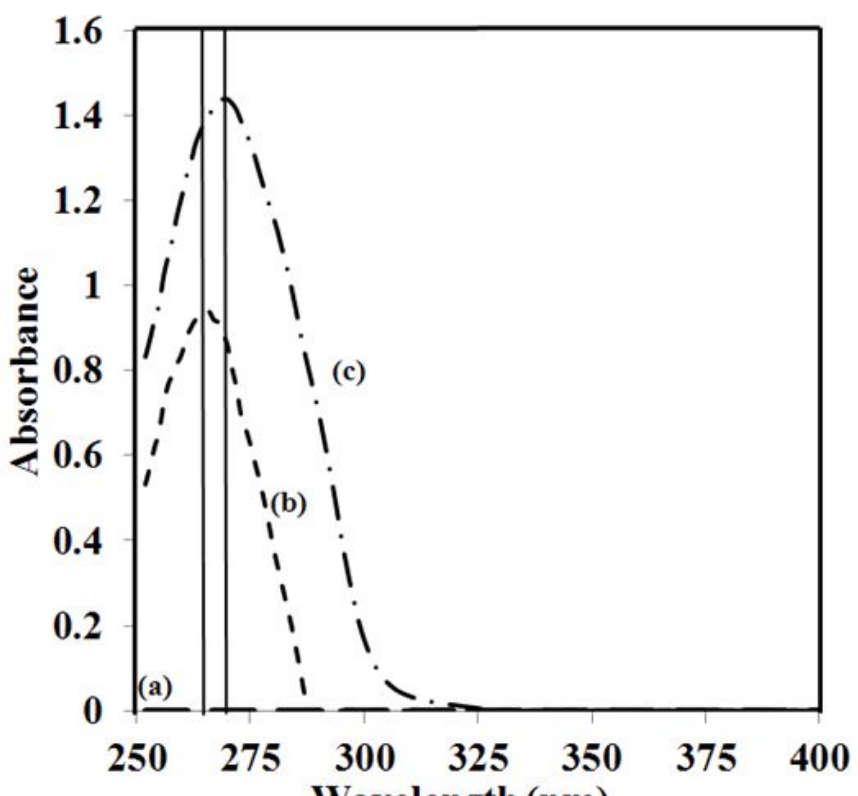




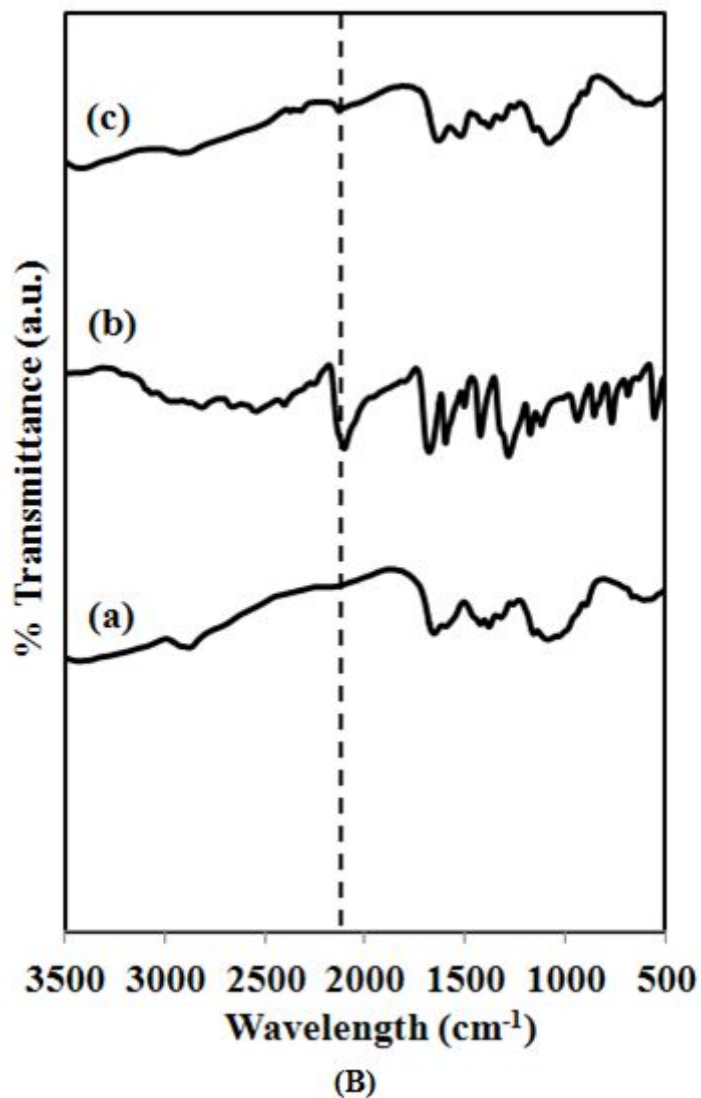
**Fig. 5.1** (A) Schematic illustration of coating procedure. The coating solution was prepared by dissolving Az-CH or a blend of Az-CH and alendronate in an aqueous acetic acid solution (2% v/v) for preparation of the Az-CH\_P or AL\_Az-CH\_P, respectively. (B) Optical images of the plate samples (a) without and (b) with the coating. The arrows indicate the locations of the coatings. The scale bars represent 3 mm.



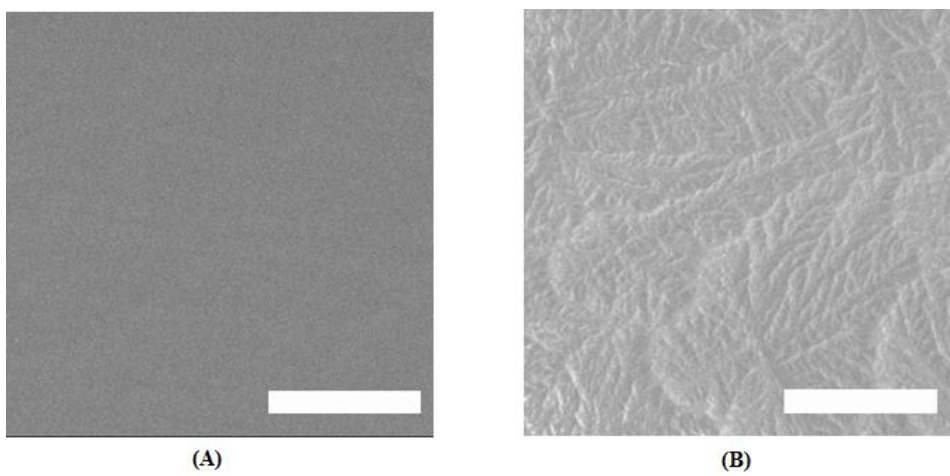
**Fig. 5.2** Optical images of the plate samples (A) without and (B) with the coating used for evaluation of mechanical property and in vivo bone regeneration. The arrows indicate the locations of the coatings. The scale bars are 5 mm.



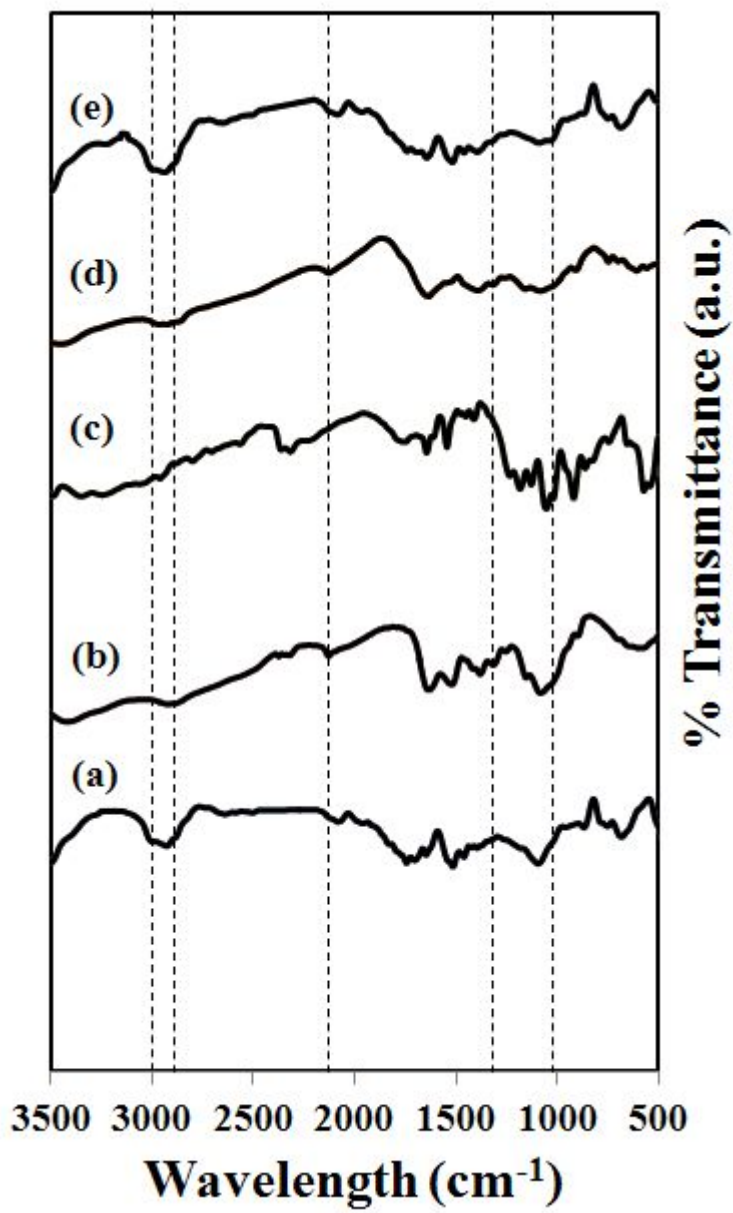
(A)



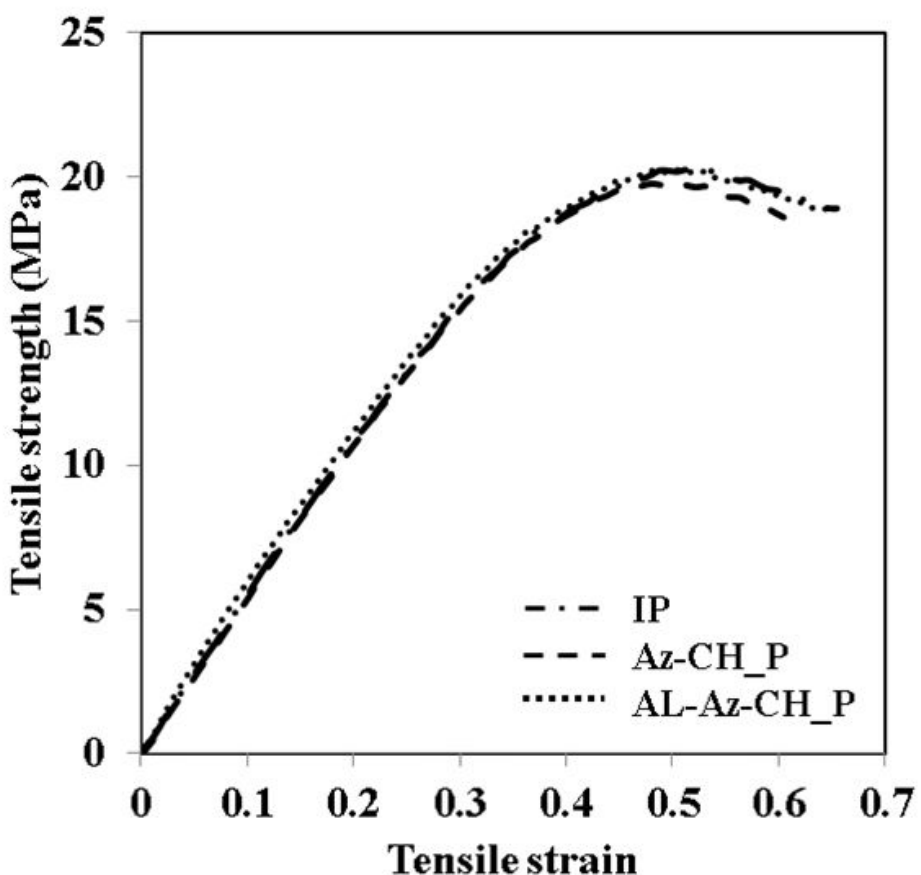
**Fig. 5.3** (A) UV spectra of (a) chitosan, (b) 4-azidobenzoic acid, and (c) Az-CH. (B) FTIR spectra of (a) chitosan, (b) 4-azidobenzoic acid and (c) Az-CH, respectively.



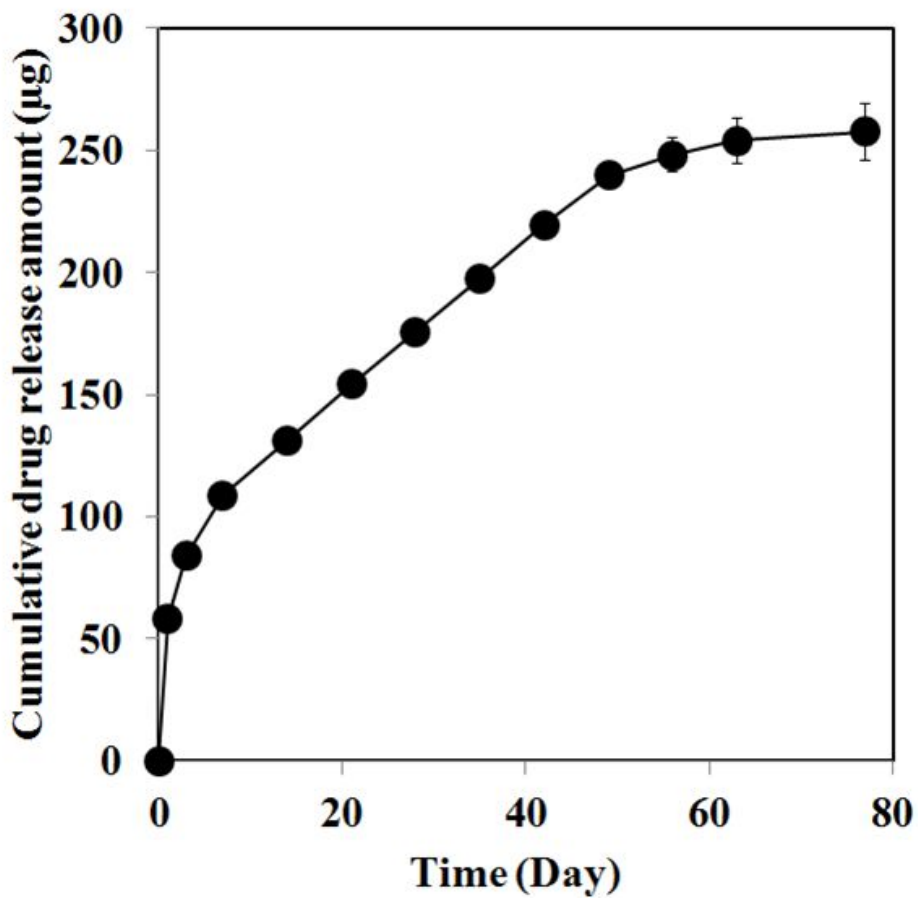
**Fig. 5.4** Scanning electron micrographs of the surfaces (A) without and (B) with the coating on the AL-Az-CH\_P. The scale bars represent 100  $\mu\text{m}$ .



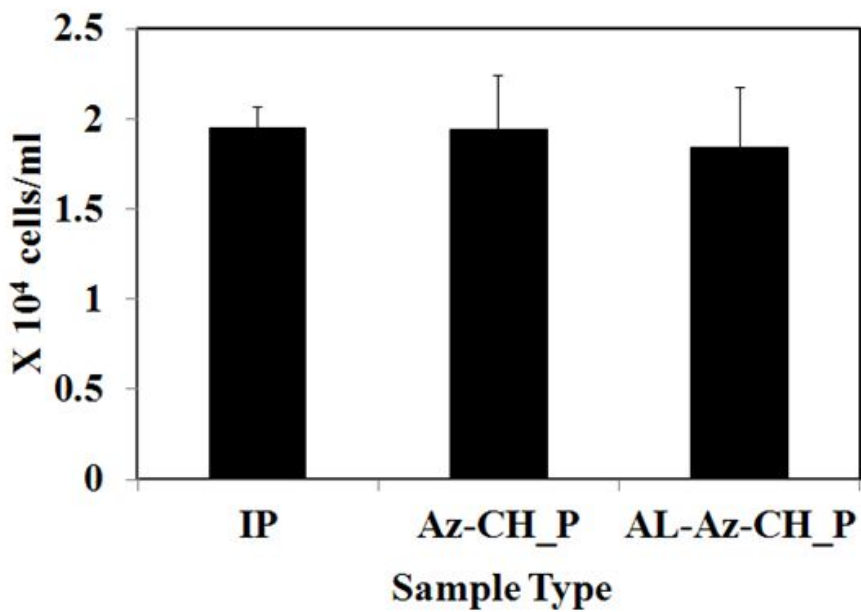
**Fig. 5.5** FTIR spectra of (a) IP, (b) Az-CH, (c) alendronate, (d) Az-CH\_P and (e) AL-Az-CH\_P. The dashed lines indicate the major peaks from IP, Az-CH and alendronate, respectively.



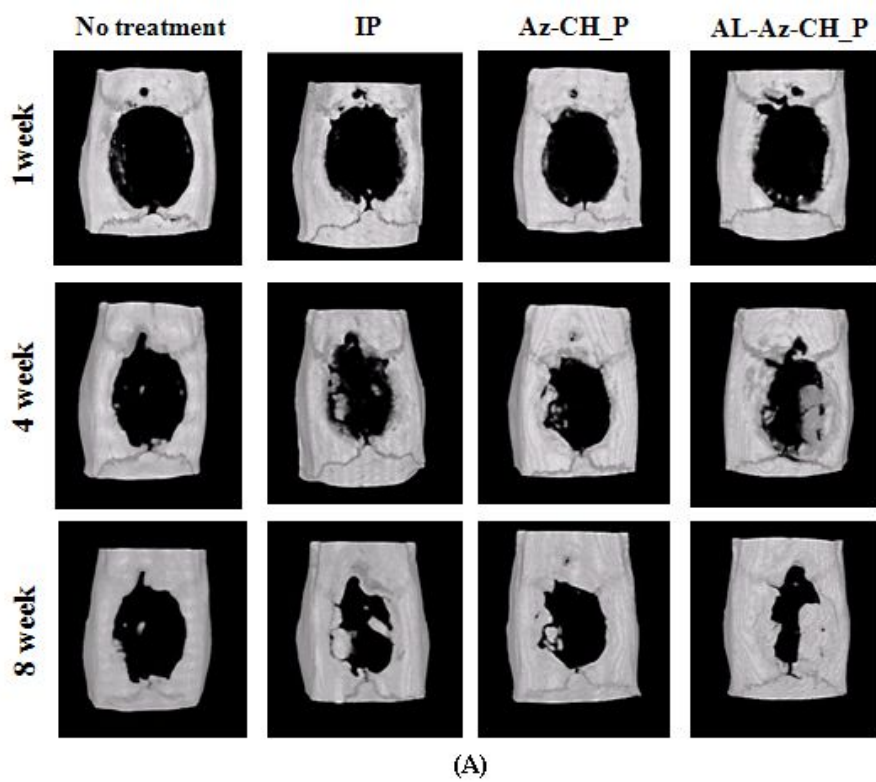
**Fig. 5.6** Stress-strain curve obtained from the plate samples prepared in this work using a universal-testing machine (UTM; Instron-5543, MA, USA) equipped with a load cell of 71 kN, where both ends of the sample were clamped and pulled at a rate of 3 mm/min until break.



**Fig. 5.7** *In vitro* drug release profiles of the AL-Az-CH\_P



**Fig. 5.8** Cytotoxicity evaluation of the plate samples. The number of L929 fibroblasts adhering to the surfaces of the IP, Az-CH\_P and AL-Az-CH\_P were assessed.



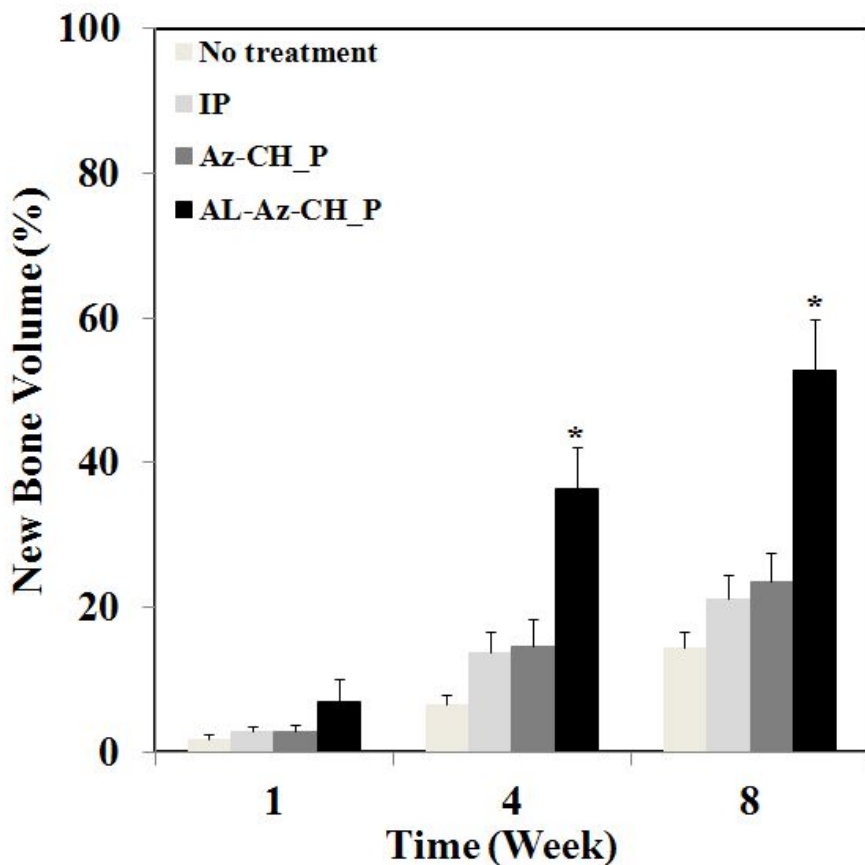


**Fig. 5.9** Micro-CT image analysis on new bone formation in cranial defects of the animal group with no treatment and the ones fixed with the IP, Az-CH\_P and AL-Az-CH\_P at 1, 4 and 8 weeks after implantation. (A) Micro-CT images and (B) new bone volume percent around the cranial defects. \*At 4 and 8 weeks, the AL-Az-CH\_P group was statistically significantly different from the no treatment group. ( $p < 0.05$ ).

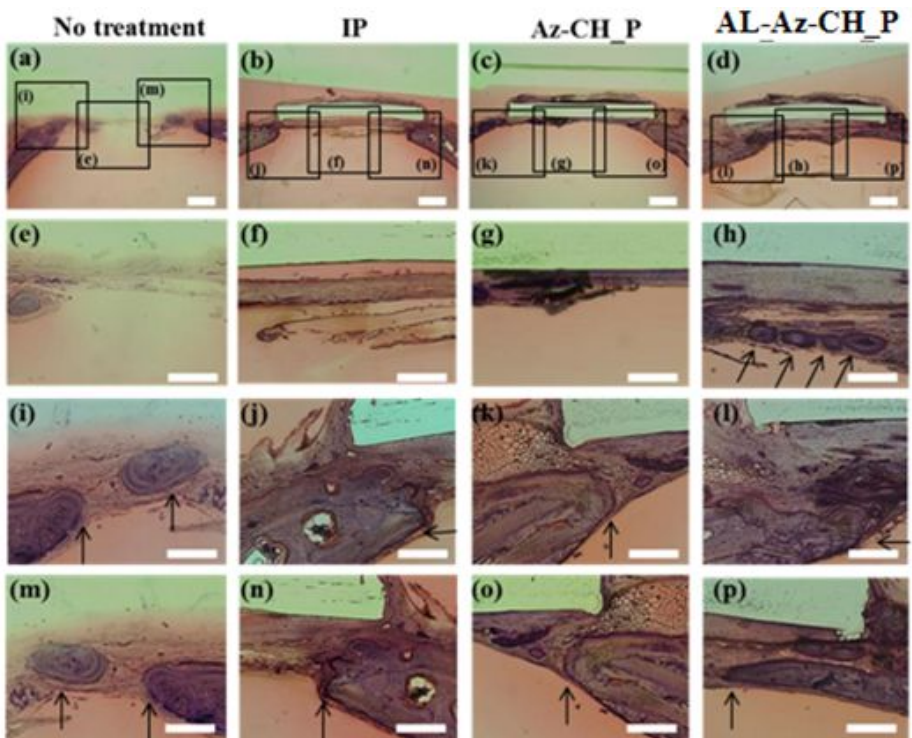


**Fig. 5.10** Histological images from the tissue around the cranial defect obtained at 8 week after implantation of the plate samples. The arrows indicate the specific locations of new bone formation. The scale bars

# Chapter 6

## General Conclusion

A variety of implantable medical devices have been significantly developed for clinical use until now. However, due to their low biocompatibility, there have still been drawbacks such as corrosion, capsular contracture or loosening of bone fixation systems. To overcome these problems, the author suggested various surface coatings of the implantable medical devices to enhance biocompatibility, based on polymeric formulation.

In chapter 3, controlled corrosion of magnesium is critical for their clinical application to orthopedic devices. For this purpose, the author coated the surface of Mg with a biodegradable polymer, polycaprolactone (PCL) and pursued to control the Mg

corrosion with varied coating thickness in a reproducible manner.

In chapter 4, the author proposes the acute, local suppression of transforming growth factor beta (TGF- $\beta$ ), a major profibrotic cytokine, to reduce fibrosis around silicone implants. To this end, the author prepared silicone implants that were able to release tranilast, a TGF- $\beta$  inhibitor, in a sustained manner for 5 days or 15 days. The author performed histologic and immunohistochemical analyses for 12 weeks after the implantation of the implants in living rats. The capsule thicknesses and collagen densities significantly decreased compared with those around the non-treated silicone implants. Notably, early suppression of TGF- $\beta$  affected the fibrogenesis that actually occurs at the late stage of wound healing. This change may be ascribed to the decrease in monocyte recruitment mediated by early TGF- $\beta$  during the acute inflammatory reaction. Thus, a significant decrease in differentiated macrophages was observed along with a decrease in the quantity of TGF- $\beta$  and fibroblasts during the subsequent inflammation stage; these changes led to a diminished fibrotic capsule formation.

In chapter 5, the author prepared a bone plate enabled with local, sustained release of alendronate, which is a drug known to inhibit osteoclast-mediated bone resorption and also expedite

bone-remodeling activity of osteoblasts. For this, the author coated a bone plate already in clinical use (PLT-1031, Inion, Finland) with a blend of alendronate and a biocompatible polymer, azidobenzoic acid-modified chitosan (i.e., Az-CH) photo-crosslinked by UV irradiation. As the author performed the *in vitro* drug release study, the drug was released from the coating at a rate of  $4.03 \mu\text{g}/\text{day}$  for 63 days in a sustained manner. To examine the effect on bone regeneration, the plate was fixed on an 8 mm cranial critical size defect in living rats and a newly formed bone volume was quantitatively evaluated by micro-computed tomography (micro-CT) at schedule times for 8 weeks. At 8 week, the group implanted with the plate enabled with sustained delivery of alendronate showed a significantly higher volume of newly formed bone ( $52.78 \pm 6.84 \%$ ) than the groups implanted with the plates without drug ( $23.6 \pm 3.81 \%$ ) ( $p < 0.05$ ). The plate enabled with alendronate delivery also exhibited good biocompatibility on H&E staining, which was comparable to the Inion plate already in clinical use. Therefore, the author suggests that a bone plate enabled with local, sustained delivery of alendronate can be a promising system of a combined functionality of bone fixation and its expedited repair.

## References

- 1.Ambrose CG, Clanton TO. Bioabsorbable implants: review of clinical experience in orthopedic surgery. *Annals of biomedical engineering.* 2004;32(1):171-7.
- 2.Kramer DB, Xu S, Kesselheim AS. Regulation of medical devices in the United States and European Union. *New England Journal of Medicine.* 2012;366(9):848-55.
- 3.Zuckerman DM, Brown P, Nissen SE. Medical device recalls and the FDA approval process. *Archives of internal medicine.* 2011;171(11):1006-11.
- 4.Uhthoff HK, Poitras P, Backman DS. Internal plate fixation of fractures: short history and recent developments. *Journal of Orthopaedic Science.* 2006;11(2):118-26.
- 5.Cornell CN. Internal fracture fixation in patients with osteoporosis. *Journal of the American Academy of Orthopaedic Surgeons.* 2003;11(2):109-19.
- 6.Goodrich JT, Sandler AL, Tepper O. A review of reconstructive materials for use in craniofacial surgery bone fixation materials, bone substitutes, and distractors. *Child's Nervous System.* 2012;28(9):1577-88.
- 7.Giannoudis P, Schneider E. Principles of fixation of osteoporotic fractures. *Journal of Bone & Joint Surgery, British Volume.* 2006;88(10):1272-8.
- 8.Uhthoff HK, Bardos DI, Liskova-Kiar M. The advantages of titanium alloy over stainless steel plates for the internal fixation of fractures. An experimental study in dogs. *Journal of Bone & Joint Surgery, British Volume.* 1981;63(3):427-84.
- 9.Leenslag JW, Pennings AJ, Bos RR, Rozema FR, Boering G. Resorbable materials of poly (L-lactide). VI. Plates and screws for internal fracture fixation. *Biomaterials.* 1987;8(1):70-3.
- 10.Uchida A, Nade S, McCARTNEY ER, Ching W. The use of ceramics for bone replacement. A comparative study of three different porous ceramics. *Journal of Bone & Joint Surgery, British Volume.* 1984;66(2):269-75.
- 11.Goodman S, Fornasier V, Kei J. The effects of bulk versus particulate ultra-high-molecular-weight polyethylene on bone. *The Journal of arthroplasty.* 1988;3:S41-S6.
- 12.Cooper C, Melton LJ. Epidemiology of osteoporosis. *Trends in Endocrinology & Metabolism.* 1992;3(6):224-9.
- 13.Stromsoe K. Fracture fixation problems in osteoporosis. *Injury.* 2004;35(2):107-13.
- 14.Perren SM. Evolution of the internal fixation of long bone fractures. *JOURNAL OF BONE AND JOINT SURGERY-BRITISH VOLUME-.* 2002;84(8):1093-110.
- 15.Reifenrath J, Bormann D, Meyer-Lindenberg A. Magnesium Alloys as Promising Degradable Implant Materials in Orthopaedic Research.

- Magnesium Alloys—Corrosion and Surface Treatments. 2011.
16. Staiger MP, Pietak AM, Huadmai J, Dias G. Magnesium and its alloys as orthopedic biomaterials: a review. *Biomaterials*. 2006;27(9):1728–34.
17. Kirkland N, Lespagnol J, Birbilis N, Staiger M. A survey of bio-corrosion rates of magnesium alloys. *Corrosion Science*. 2010;52(2):287–91.
18. Quinn KJ, Courtney JM. Silicones as biomaterials. *British polymer journal*. 1988;20(1):25–32.
19. Bondurant S, Ernster V, Herdman R. Safety of silicone breast implants. Committee on the Safety of Silicone Breast Implants, Division of Health Promotion and Disease Prevention, Institute of Medicine. Washington, DC: National Academy Press; 2000.
20. Stevens WG, Pacella SJ, Gear AJ, Freeman ME, McWhorter C, Tenenbaum MJ, et al. Clinical experience with a fourth-generation textured silicone gel breast implant: a review of 1012 Mentor MemoryGel breast implants. *Aesthetic Surgery Journal*. 2008;28(6):642–7.
21. Valencia-Lazcano AA, Alonso-Rasgado T, Bayat A. Physico-chemical characteristics of coated silicone textured versus smooth breast implants differentially influence breast-derived fibroblast morphology and behaviour. *Journal of the mechanical behavior of biomedical materials*. 2014;40:140–55.
22. Siggelkow W, Klosterhalfen B, Klinge U, Rath W, Faridi A. Analysis of local complications following explantation of silicone breast implants. *The Breast*. 2004;13(2):122–8.
23. Handel N, Cordray T, Gutierrez J, Jensen JA. A long-term study of outcomes, complications, and patient satisfaction with breast implants. *Plastic and reconstructive surgery*. 2006;117(3):757–67.
24. Araco A, Caruso R, Araco F, Overton J, Gravante G. Capsular contractures: a systematic review. *Plastic and reconstructive surgery*. 2009;124(6):1808.
25. Murata H, Chang B-J, Prucker O, Dahm M, Rühe J. Polymeric coatings for biomedical devices. *Surface science*. 2004;570(1):111–8.
26. Gray J, Luan B. Protective coatings on magnesium and its alloys—a critical review. *Journal of alloys and compounds*. 2002;336(1):88–113.
27. Scriven L, editor. Physics and applications of dip coating and spin coating1988: Cambridge Univ Press.
28. Park M, Lee JE, Park CG, Lee SH, Seok HK, Choy YB. Polycaprolactone coating with varying thicknesses for controlled corrosion of magnesium. *Journal of Coatings Technology and Research*. 2013;10(5):695–706.
29. Middleton JC, Tipton AJ. Synthetic biodegradable polymers as orthopedic devices. *Biomaterials*. 2000;21(23):2335–46.
30. Pillai O, Panchagnula R. Polymers in drug delivery. *Current opinion in chemical biology*. 2001;5(4):447–51.
31. Uhrich KE, Cannizzaro SM, Langer RS, Shakesheff KM. Polymeric systems for controlled drug release. *Chemical reviews*. 1999;99(11):3181–98.

- 32.Soppimath KS, Aminabhavi TM, Kulkarni AR, Rudzinski WE. Biodegradable polymeric nanoparticles as drug delivery devices. *Journal of Controlled Release*. 2001;70(1):1–20.
- 33.Makadia HK, Siegel SJ. Poly lactic-co-glycolic acid (PLGA) as biodegradable controlled drug delivery carrier. *Polymers*. 2011;3(3):1377–97.
- 34.Langer R, Chasin M. Biodegradable polymers as drug delivery systems. Marcel Dekker, New York; 1990.
- 35.Chen Y, Song Y, Zhang S, Li J, Zhao C, Zhang X. Interaction between a high purity magnesium surface and PCL and PLA coatings during dynamic degradation. *Biomedical Materials*. 2011;6(2):025005.
- 36.Zhang E, Xu L, Yu G, Pan F, Yang K. In vivo evaluation of biodegradable magnesium alloy bone implant in the first 6 months implantation. *Journal of Biomedical Materials Research Part A*. 2009;90(3):882–93.
- 37.Anderson JM, Shive MS. Biodegradation and biocompatibility of PLA and PLGA microspheres. *Advanced drug delivery reviews*. 2012;64:72–82.
- 38.Davis SS, Illum L. Polymeric microspheres as drug carriers. *Biomaterials*. 1988;9(1):111–2, IN5, 3–5.
- 39.Hickey T, Kreutzer D, Burgess D, Moussy F. Dexamethasone/PLGA microspheres for continuous delivery of an anti-inflammatory drug for implantable medical devices. *Biomaterials*. 2002;23(7):1649–56.
- 40.Behravesh E, Yasko A, Engel P, Mikos A. Synthetic biodegradable polymers for orthopaedic applications. *Clinical orthopaedics and related research*. 1999;367:S118–S29.
- 41.Rinaudo M. Chitin and chitosan: properties and applications. *Progress in polymer science*. 2006;31(7):603–32.
- 42.Bhattarai N, Gunn J, Zhang M. Chitosan-based hydrogels for controlled, localized drug delivery. *Advanced drug delivery reviews*. 2010;62(1):83–99.
- 43.Ravi Kumar MN. A review of chitin and chitosan applications. *Reactive and functional polymers*. 2000;46(1):1–27.
- 44.Dodane V, Vilivalam VD. Pharmaceutical applications of chitosan. *Pharmaceutical Science & Technology Today*. 1998;1(6):246–53.
- 45.Niinomi M. Recent metallic materials for biomedical applications. *Metallurgical and materials transactions A*. 2002;33(3):477–86.
- 46.Shikinami Y, Okuno M. Bioresorbable devices made of forged composites of hydroxyapatite (HA) particles and poly-lactide (PLLA). Part II: practical properties of miniscrews and miniplates. *Biomaterials*. 2001;22(23):3197–211.
- 47.Zhang S, Zhang X, Zhao C, Li J, Song Y, Xie C, et al. Research on an Mg–Zn alloy as a degradable biomaterial. *Acta biomaterialia*. 2010;6(2):626–40.
- 48.Gu XN, Zheng YF. A review on magnesium alloys as biodegradable materials. *Frontiers of Materials Science in China*. 2010;4(2):111–5.
- 49.Wang H, Shi Z. In vitro biodegradation behavior of magnesium and magnesium alloy. *Journal of Biomedical Materials Research Part B*:

- Applied Biomaterials. 2011;98(2):203–9.
- 50.Yamamoto A, Hiromoto S. Effect of inorganic salts, amino acids and proteins on the degradation of pure magnesium in vitro. Materials Science and Engineering: C. 2009;29(5):1559–68.
- 51.Saris NEL, Mervaala E, Karppanen H, Khawaja JA, Lewenstam A. Magnesium:: An update on physiological, clinical and analytical aspects. Clinica Chimica Acta. 2000;294(1–2):1–26.
- 52.Vormann J. Magnesium: nutrition and metabolism. Molecular Aspects of Medicine. 2003;24(1–3):27–37.
- 53.Witte F, Kaese V, Haferkamp H, Switzer E, Meyer-Lindenberg A, Wirth C, et al. In vivo corrosion of four magnesium alloys and the associated bone response. Biomaterials. 2005;26(17):3557–63.
- 54.Song G. Control of biodegradation of biocompatible magnesium alloys. Corrosion Science. 2007;49(4):1696–701.
- 55.Fan Y, Wu G, Zhai C. Influence of cerium on the microstructure, mechanical properties and corrosion resistance of magnesium alloy. Materials Science and Engineering: A. 2006;433(1):208–15.
- 56.Song G, StJohn D. The effect of zirconium grain refinement on the corrosion behaviour of magnesium–rare earth alloy MEZ. Journal of Light Metals. 2002;2(1):1–16.
- 57.Gu X, Zheng Y, Lan Q, Cheng Y, Zhang Z, Xi T, et al. Surface modification of an Mg–1Ca alloy to slow down its biocorrosion by chitosan. Biomedical Materials. 2009;4:044109.
- 58.Ng W, Wong M, Cheng F. Stearic acid coating on magnesium for enhancing corrosion resistance in Hanks' solution. Surface and coatings technology. 2010;204(11):1823–30.
- 59.Li J, Cao P, Zhang X, Zhang S, He Y. In vitro degradation and cell attachment of a PLGA coated biodegradable Mg–6Zn based alloy. Journal of materials science. 2010;1–8.
- 60.Chen Y, Song Y, Zhang S, Li J, Zhao C, Zhang X. Interaction between a high purity magnesium surface and PCL and PLA coatings during dynamic degradation. Biomedical Materials. 2011;6:025005.
- 61.Lee JY, Han G, Kim YC, Byun JY, Jang J, Seok HK, et al. Effects of impurities on the biodegradation behavior of pure magnesium. Metals and Materials International. 2009;15(6):955–61.
- 62.Wong HM, Yeung KWK, Lam KO, Tam V, Chu PK, Luk KDK, et al. A biodegradable polymer-based coating to control the performance of magnesium alloy orthopaedic implants. Biomaterials. 2010;31(8):2084–96.
- 63.Gray-Munro JE, Seguin C, Strong M. Influence of surface modification on the in vitro corrosion rate of magnesium alloy AZ31. Journal of Biomedical Materials Research Part A. 2009;91(1):221–30.
- 64.Tan C, Blackwood D. Corrosion protection by multilayered conducting polymer coatings. Corrosion Science. 2003;45(3):545–57.
- 65.Bautista A. Filiform corrosion in polymer-coated metals. Progress in organic coatings. 1996;28(1):49–58.
- 66.Cha Y, Pitt C. The biodegradability of polyester blends. Biomaterials. 1990;11(2):108–12.

- 67.Yang J, Cui F, Lee IS. Surface Modifications of Magnesium Alloys for Biomedical Applications. *Annals of biomedical engineering*. 2011;1-15.
- 68.Van Zele D, Heymans O. Breast implants. A review. *Acta Chirurgica Belgica*. 2004(2):158-65.
- 69.Wynn TA, Ramalingam TR. Mechanisms of fibrosis: therapeutic translation for fibrotic disease. *Nature Medicine*. 2012;18(7):1028-40.
- 70.Anderson JM, Rodriguez A, Chang DT, editors. Foreign body reaction to biomaterials. *Seminars in immunology*; 2008: NIH Public Access.
- 71.Serhan CN, Chiang N, Van Dyke TE. Resolving inflammation: dual anti-inflammatory and pro-resolution lipid mediators. *Nature Reviews Immunology*. 2008;8(5):349-61.
- 72.Anderson JM. Mechanisms of inflammation and infection with implanted devices. *Cardiovascular Pathology*. 1993;2(3):33-41.
- 73.Geissmann F, Manz MG, Jung S, Sieweke MH, Merad M, Ley K. Development of monocytes, macrophages, and dendritic cells. *Science*. 2010;327(5966):656-61.
- 74.Serhan CN, Savill J. Resolution of inflammation: the beginning programs the end. *Nature immunology*. 2005;6(12):1191-7.
- 75.Johnston Jr RB. Monocytes and macrophages. *New England Journal of Medicine*. 1988;318(12):747-52.
- 76.Santibanez JF, Quintanilla M, Bernabeu C. TGF-beta/TGF-beta receptor system and its role in physiological and pathological conditions. *Clinical Science*. 2011;121(6):233-51.
- 77.Rappolee DA, Mark D, Banda MJ, Werb Z. Wound macrophages express TGF-alpha and other growth factors in vivo: analysis by mRNA phenotyping. *Science*. 1988;241(4866):708-12.
- 78.Ashcroft GS. Bidirectional regulation of macrophage function by TGF- $\beta$ . *Microbes and infection*. 1999;1(15):1275-82.
- 79.Nathan C. Points of control in inflammation. *Nature*. 2002;420(6917):846-52.
- 80.Sporn MB, Roberts AB, Wakefield LM, Assoian RK. Transforming growth factor-beta: biological function and chemical structure. *Science*. 1986;233(4763):532-4.
- 81.Wahl S, McCARTNEY-FRANCIS N, Allen J, Dougherty E, Dougherty S. Macrophage Production of TGF- $\beta$  and Regulation by TGF- $\beta$ . *Annals of the New York Academy of Sciences*. 1990;593(1):188-96.
- 82.Mustoe TA, Pierce GF, Thomason A, Gramates P, Sporn MB, Deuel TF. Accelerated healing of incisional wounds in rats induced by transforming growth factor-beta. *Science*. 1987;237(4820):1333-6.
- 83.Martin J, Kelly DJ, Mifsud SA, Zhang Y, Cox AJ, See F, et al. Tranilast attenuates cardiac matrix deposition in experimental diabetes: role of transforming growth factor- $\beta$ . *Cardiovascular research*. 2005;65(3):694-701.
- 84.Ikeda H, Inao M, Fujiwara K. Inhibitory Effect of Tranilast on Activation and Transforming Growth Factor [beta] 1 Expression in Cultured Rat Stellate Cells. *Biochemical and biophysical research communications*. 1996;227(2):322-7.
- 85.Prud'homme GJ. Pathobiology of transforming growth factor  $\beta$  in

- cancer, fibrosis and immunologic disease, and therapeutic considerations. *Laboratory investigation*. 2007;87(11):1077–91.
- 86.Suzawa H, Kikuchi S, Arai N, Koda A. The mechanism involved in the inhibitory action of tranilast on collagen biosynthesis of keloid fibroblasts. *Japanese journal of pharmacology*. 1992;60(2):91.
- 87.Kelly DJ, Zhang Y, Gow R, Gilbert RE. Tranilast attenuates structural and functional aspects of renal injury in the remnant kidney model. *Journal of the American Society of Nephrology*. 2004;15(10):2619–29.
- 88.Bonnet F, Cao Z, Cooper M, Cox A, Kelly D, Gilbert R. Tranilast attenuates vascular hypertrophy, matrix accumulation and growth factor overexpression in experimental diabetes. *Diabetes & metabolism*. 2003;29(4):386–92.
- 89.Mori T, Kawara S, Shinozaki M, Hayashi N, Kakinuma T, Igarashi A, et al. Role and interaction of connective tissue growth factor with transforming growth factor- $\beta$  in persistent fibrosis: A mouse fibrosis model. *Journal of cellular physiology*. 1999;181(1):153–9.
- 90.Qi W, Chen X, Twigg S, Polhill T, Gilbert R, Pollock C. Tranilast attenuates connective tissue growth factor-induced extracellular matrix accumulation in renal cells. *Kidney international*. 2006;69(6):989–95.
- 91.Oshima T, Kurosaka D, Kato K, Kurosaka H, Mashima Y, Tanaka Y, et al. Tranilast inhibits cell proliferation and collagen synthesis by rabbit corneal and Tenon's capsule fibroblasts. *Current eye research*. 2000;20(4):283–6.
- 92.Kagitani S, Ueno H, Hirade S, Takahashi T, Takata M, Inoue H. Tranilast attenuates myocardial fibrosis in association with suppression of monocyte/macrophage infiltration in DOCA/salt hypertensive rats. *Journal of hypertension*. 2004;22(5):1007.
- 93.Freiberg S, Zhu X. Polymer microspheres for controlled drug release. *International Journal of Pharmaceutics*. 2004;282(1):1–18.
- 94.Shasteen C, Choy YB. Controlling degradation rate of poly (lactic acid) for its biomedical applications. *Biomedical Engineering Letters*. 2011;1(3):163–7.
- 95.Zeplin PH, Larena-Avellaneda A, Schmidt K. Surface modification of silicone breast implants by binding the antifibrotic drug halofuginone reduces capsular fibrosis. *Plastic and reconstructive surgery*. 2010;126(1):266.
- 96.Ruiz-de-Erenchun R, de las Herreras JD, Hontanilla B. Use of the Transforming Growth Factor- $\beta$ 1 Inhibitor Peptide in Periprosthetic Capsular Fibrosis: Experimental Model with Tetraglycerol Dipalmitate. *Plastic and reconstructive surgery*. 2005;116(5):1370–8.
- 97.Ward MR, Kanellakis P, Ramsey D, Funder J, Bobik A. Eplerenone suppresses constrictive remodeling and collagen accumulation after angioplasty in porcine coronary arteries. *Circulation*. 2001;104(4):467–72.
- 98.De Albuquerque DA, Saxena V, Adams DE, Boivin GP, Brunner HI, Witte DP, et al. An ACE inhibitor reduces Th2 cytokines and TGF- $\beta$ 1 and TGF- $\beta$ 2 isoforms in murine lupus nephritis. *Kidney international*. 2004;65(3):846–59.

- 99.Baeten D, Demetter P, Cuvelier CA, Kruithof E, Van Damme N, De Vos M, et al. Macrophages expressing the scavenger receptor CD163: a link between immune alterations of the gut and synovial inflammation in spondyloarthropathy. *The Journal of pathology*. 2002;196(3):343–50.
- 100.Spano A, Palmieri B, Nava M. Reduction of capsular thickness around silicone breast implants by zafirlukast in rats. *European Surgical Research*. 2008;41(1):8–14.
- 101.Pavia D, Lampman G, Kriz G, Vyvyan J. *Introduction to spectroscopy*: Cengage Learning; 2008.
- 102.Paragkumar N T, Edith D, Six J-L. Surface characteristics of PLA and PLGA films. *Applied Surface Science*. 2006;253(5):2758–64.
- 103.Lu L, Garcia CA, Mikos AG. In vitro degradation of thin poly (DL-lactic-co-glycolic acid) films. *Journal of biomedical materials research*. 1999;46(2):236–44.
- 104.Lodish H, Berk A, Zipursky SL, Matsudaira P, Baltimore D, Darnell J. *Molecular cell biology*. New York. 2000.
- 105.Jones KS, editor. *Effects of biomaterial-induced inflammation on fibrosis and rejection*. Seminars in immunology; 2008: Elsevier.
- 106.Kamath S, Bhattacharyya D, Padukudru C, Timmons RB, Tang L. Surface chemistry influences implant-mediated host tissue responses. *Journal of Biomedical Materials Research Part A*. 2008;86(3):617–26.
- 107.Khalil N, Bereznay O, Sporn M, Greenberg A. Macrophage production of transforming growth factor beta and fibroblast collagen synthesis in chronic pulmonary inflammation. *The Journal of experimental medicine*. 1989;170(3):727–37.
- 108.Dolores W, Christian R, Harald N, Hildegunde P, Georg W. Cellular and molecular composition of fibrous capsules formed around silicone breast implants with special focus on local immune reactions. *Journal of autoimmunity*. 2004;23(1):81–91.
- 109.Diegelmann RF, Evans MC. Wound healing: an overview of acute, fibrotic and delayed healing. *Front Biosci*. 2004;9(1):283–9.
- 110.Lawrance IC, Maxwell L, Doe W. Inflammation location, but not type, determines the increase in TGF- $\beta$ 1 and IGF-1 expression and collagen deposition in IBD intestine. *Inflammatory bowel diseases*. 2001;7(1):16–26.
- 111.Roche W. Fibroblasts and fibrosis. *Clinical & Experimental Allergy*. 1991;21(5):635–6.
- 112.Chi KL, Claman HN. Mast cells, fibroblasts, and fibrosis. *Immunologic research*. 1987;6(3):145–52.
- 113.Anderson JM. Biological responses to materials. *Annual Review of Materials Research*. 2001;31(1):81–110.
- 114.Shi C, Pamer EG. Monocyte recruitment during infection and inflammation. *Nature Reviews Immunology*. 2011;11(11):762–74.
- 115.Friedman SL, Sheppard D, Duffield JS, Violette S. Therapy for fibrotic diseases: nearing the starting line. *Science translational medicine*. 2013;5(167):167sr1–sr1.
- 116.Maurus PB, Kaeding CC. Bioabsorbable implant material review. *Operative Techniques in Sports Medicine*. 2004;12(3):158–60.

- 117.Rodríguez JP, Garat S, Gajardo H, Pino AM, Seitz G. Abnormal osteogenesis in osteoporotic patients is reflected by altered mesenchymal stem cells dynamics. *Journal of cellular biochemistry*. 1999;75(3):414–23.
- 118.Liu J, Xu X. [Stress shielding and fracture healing]. *Zhonghua yi xue za zhi*. 1994;74(8):483–5, 519.
- 119.Stover M. Distal femoral fractures: current treatment, results and problems. *Injury*. 2001;32:3–13.
- 120.Orwoll E, Ettinger M, Weiss S, Miller P, Kendler D, Graham J, et al. Alendronate for the treatment of osteoporosis in men. *New England Journal of Medicine*. 2000;343(9):604–10.
- 121.Drake MT, Clarke BL, Khosla S, editors. *Bisphosphonates: mechanism of action and role in clinical practice*. Mayo Clinic Proceedings; 2008: Elsevier.
- 122.Rodan GA, Fleisch HA. Bisphosphonates: mechanisms of action. *Journal of Clinical Investigation*. 1996;97(12):2692.
- 123.Moon H-J, Yun Y-P, Han C-W, Kim MS, Kim SE, Bae MS, et al. Effect of heparin and alendronate coating on titanium surfaces on inhibition of osteoclast and enhancement of osteoblast function. *Biochemical and biophysical research communications*. 2011;413(2):194–200.
- 124.Im G-I, Qureshi SA, Kenney J, Rubash HE, Shanbhag AS. Osteoblast proliferation and maturation by bisphosphonates. *Biomaterials*. 2004;25(18):4105–15.
- 125.Garcia-Moreno C, Serrano S, Nacher M, Farre M, Diez A, Marinoso M, et al. Effect of alendronate on cultured normal human osteoblasts. *Bone*. 1998;22(3):233–9.
- 126.Reinholz GG, Getz B, Pederson L, Sanders ES, Subramaniam M, Ingle JN, et al. Bisphosphonates directly regulate cell proliferation, differentiation, and gene expression in human osteoblasts. *Cancer research*. 2000;60(21):6001–7.
- 127.Bone HG, Hosking D, Devogelaer J-P, Tucci JR, Emkey RD, Tonino RP, et al. Ten years' experience with alendronate for osteoporosis in postmenopausal women. *New England Journal of Medicine*. 2004;350(12):1189–99.
- 128.Aki S, Eskiyurt N, Akarirmakz I-I, Tiiziinz F, Eryavuzz M, Alperz S, et al. Gastrointestinal Side Effect Profile Due to the Use of Alendronate in the Treatment of Osteoporosis. *Yonsei medical journal*. 2003;44(6):961–7.
- 129.Jindong Z, Hai T, Junchao G, Bo W, Li B, Qiang WB. Evaluation of a novel osteoporotic drug delivery system in vitro: alendronate-loaded calcium phosphate cement. *Orthopedics*. 2010;33(8):561.
- 130.Kim SE, Suh DH, Yun Y-P, Lee JY, Park K, Chung J-Y, et al. Local delivery of alendronate eluting chitosan scaffold can effectively increase osteoblast functions and inhibit osteoclast differentiation. *Journal of Materials Science: Materials in Medicine*. 2012;23(11):2739–49.
- 131.Shi X, Wang Y, Ren L, Gong Y, Wang D-A. Enhancing alendronate release from a novel PLGA/hydroxyapatite microspheric system for

- bone repairing applications. *Pharmaceutical research*. 2009;26(2):422–30.
- 132.Obara K, Ishihara M, Ozeki Y, Ishizuka T, Hayashi T, Nakamura S, et al. Controlled release of paclitaxel from photocrosslinked chitosan hydrogels and its subsequent effect on subcutaneous tumor growth in mice. *Journal of Controlled Release*. 2005;110(1):79–89.
- 133.Zhu A, Zhang M, Wu J, Shen J. Covalent immobilization of chitosan/heparin complex with a photosensitive hetero-bifunctional crosslinking reagent on PLA surface. *Biomaterials*. 2002;23(23):4657–65.
- 134.Aiba S-i, Minoura N, Taguchi K, Fujiwara Y. Covalent immobilization of chitosan derivatives onto polymeric film surfaces with the use of a photosensitive hetero-bifunctional crosslinking reagent. *Biomaterials*. 1987;8(6):481–8.
- 135.Yeo Y, Burdick JA, Highley CB, Marini R, Langer R, Kohane DS. Peritoneal application of chitosan and UV-cross-linkable chitosan. *Journal of Biomedical Materials Research Part A*. 2006;78(4):668–75.
- 136.Lutolf MP, Weber FE, Schmoekel HG, Schense JC, Kohler T, Müller R, et al. Repair of bone defects using synthetic mimetics of collagenous extracellular matrices. *Nature biotechnology*. 2003;21(5):513–8.
- 137.Buijs GJ, van der Houwen EB, Stegenga B, Bos RR, Verkerke GJ. Mechanical strength and stiffness of biodegradable and titanium osteofixation systems. *Journal of Oral and Maxillofacial Surgery*. 2007;65(11):2148–58.
- 138.Al Deeb SK, Hamdan II, Al Najjar SM. Spectroscopic and HPLC methods for the determination of alendronate in tablets and urine. *Talanta*. 2004;64(3):695–702.
- 139.Huang Z, Lee H, Lee E, Kang S-K, Nam J-M, Lee M. Responsive nematic gels from the self-assembly of aqueous nanofibres. *Nature communications*. 2011;2:459.
- 140.Spicer PP, Kretlow JD, Young S, Jansen JA, Kasper FK, Mikos AG. Evaluation of bone regeneration using the rat critical size calvarial defect. *Nature protocols*. 2012;7(10):1918–29.
- 141.Ma Y, Zheng Y, Liu K, Tian G, Tian Y, Xu L, et al. Nanoparticles of poly (lactide-co-glycolide)-da-tocopheryl polyethylene glycol 1000 succinate random copolymer for cancer treatment. *Nanoscale research letters*. 2010;5(7):1161–9.
- 142.Fernandes LL, Resende CX, Tavares DS, Soares GA, Castro LO, Granjeiro JM. Cytocompatibility of chitosan and collagen-chitosan scaffolds for tissue engineering. *Polímeros*. 2011;21(1):1–6.
- 143.Wang CY, Xiao XF, Mao D, Tang HZ, Liu RF. The study of using TiO<sub>2</sub> nanotube arrays as a drug delivery for alendronate. *Advanced Materials Research*. 2011;335:1469–72.
- 144.Daniels A, Chang MK, Andriano KP, Heller J. Mechanical properties of biodegradable polymers and composites proposed for internal fixation of bone. *Journal of Applied Biomaterials*. 1990;1(1):57–78.
- 145.Wang C-Z, Chen S-M, Chen C-H, Wang C-K, Wang G-J, Chang J-K, et al. The effect of the local delivery of alendronate on human adipose-derived stem cell-based bone regeneration. *Biomaterials*.

- 2010;31(33):8674–83.
- 146.Meraw SJ, Reeve CM, Wollan PC. Use of alendronate in peri-implant defect regeneration. *Journal of periodontology*. 1999;70(2):151–8.
- 147.Cottrell JA, Vales FM, Schachter D, Wadsworth S, Gundlapalli R, Kapadia R, et al. Osteogenic activity of locally applied small molecule drugs in a rat femur defect model. *BioMed Research International*. 2010;2010.
- 148.Shu X, Zhu K, Song W. Novel pH-sensitive citrate cross-linked chitosan film for drug controlled release. *International Journal of Pharmaceutics*. 2001;212(1):19–28.
- 149.Ishihara M, Fujita M, Obara K, Hattori H, Nakamura S, Nambu M, et al. Controlled releases of FGF-2 and paclitaxel from chitosan hydrogels and their subsequent effects on wound repair, angiogenesis, and tumor growth. *Current drug delivery*. 2006;3(4):351–8.
- 150.Rinaudo M, Pavlov G, Desbrieres J. Influence of acetic acid concentration on the solubilization of chitosan. *Polymer*. 1999;40(25):7029–32.
- 151.Bone HG, Adami S, Rizzoli R, Favus M, Ross PD, Santora A, et al. Weekly administration of alendronate: rationale and plan for clinical assessment. *Clinical therapeutics*. 2000;22(1):15–28.
- 152.Van den Wyngaert T, Huizing MT, Vermorken JB. Osteonecrosis of the jaw related to the use of bisphosphonates. *Current opinion in oncology*. 2007;19(4):315–22.
- 153.Srisubut S, Teerakapong A, Vattraphodes T, Taweechaisupapong S. Effect of local delivery of alendronate on bone formation in bioactive glass grafting in rats. *Oral Surgery, Oral Medicine, Oral Pathology, Oral Radiology, and Endodontology*. 2007;104(4):e11–e6.
- 154.Kim CW, Yun Y-P, Lee HJ, Hwang Y-S, Kwon IK, Lee SC. In situ fabrication of alendronate-loaded calcium phosphate microspheres: Controlled release for inhibition of osteoclastogenesis. *Journal of Controlled Release*. 2010;147(1):45–53.

## Abstract in Korean

## 국문 초록

이 학위논문은 골접합용 의료기기 및 실리콘 임플란트 같은 이식형 의료기기에 향상된 치료기능을 부가하기 위한 목적을 위해 수행한 임플란트 표면 코팅을 위한 재료, 디자인, 공정방법, 분석 및 평가에 관한 것이다. 현재까지 이식형 의료기기가 임상분야에서 널리 개발되고 사용되고 있지만, 여전히 증강된 치료기능의 부족으로 인하여 단점들을 가지고 있다. 이러한 단점들을 해결하기 위하여, 이식형 의료기기가 가지고 있는 본래의 기능은 유지하면서, 증강된 치료 기능을 부가함으로써 다기능성 이식형 의료기기를 제안하고자 한다.

첫째로, 골접합용 소재 중 하나인 마그네슘(magnesium)의 부식속도를 제어하기 위하여, 생분해성 고분자인 폴리카프로락톤을 마그네슘 표면에 코팅을 하고자, 널리 사용되고 있는 딥코팅(dip-coating)이 가능한 코팅장치를 개발하여 코팅하였으며, 특히 이를 이용하여 코팅 두께를 다양화 하였다. 여기서, 폴리카프로락톤은 강한 소수성 성질 및 생체 내 환경에서 매우 느린 분해 속도로 인하여 수분 투과에 대한 방해벽 역할을 하였다. 코팅 두께를 0  $\mu\text{m}$  부터 13.31 ± 0.36  $\mu\text{m}$ 으로 증가시키심에 따라서 마그네슘의 부식속도를 의미하는 부식에 의한 수소가스 발생량 및 마그네슘의 이온 양을 측정한 결과, 수소가스 발생량은 0.57  $\text{ml}/\text{cm}^2/\text{day}$ 에서 0.20  $\text{ml}/\text{cm}^2/\text{day}$ 으로, 마그네슘 이온 양은 0.55  $\text{mg}/\text{day}$ 에서 0.26  $\text{mg}/\text{day}$ 으로 절반 정도까지 감소한 결과를 얻을 수 있었다. 이러한

결과를 바탕으로, 코팅 두께가 두꺼워질수록 마그네슘 표면에 수분의 침투를 더욱 방해할 수 있었고, 이를 통하여 부식속도를 억제할 수 있음을 알 수 있었다.

둘째로, 파골세포의 활동성을 억제하고, 조골세포의 골형성을 촉진하는 약물로 알려진 알렌드로네이트(alendronate)의 국소적이고 서방전달이 가능한 정형외과용 골접합 본플레이트를 개발하고자 하였다. 이를 위하여 약물과 생체 적합한 고분자인 아지도벤조익 엑시드(azidobenzoic acid)으로 개질된 키토산(chitosan)을 혼합하여 이를 실제 임상에서 사용되고 있는 본플레이트(PLT-1031, Inion, Finland) 표면에 코팅한 후, 자외선 조사를 통하여 광파교를 시켰다. 그 후, *in vitro* 약물 방출실험을 통하여 약물이 약 63일 동안  $4.03 \mu\text{g}/\text{day}$ 의 방출 속도로 방출됨을 확인하였다. 이를 바탕으로 골형성 촉진에 효과를 내는지 확인하기 위하여, 제작한 샘플을 살아 있는 동물(rat) 모델의 두개골 내에 지름 8 mm 크기의 구멍을 낸 bone defect위에 이식한 후, 새롭게 형성되는 뼈의 양을 마이크로시티(micro-CT)를 이용하여 8주 동안 측정하였다. 8주 후에 약물이 탑재되어 있지 않은 플레이트를 이식한 그룹은 새롭게 형성된 뼈의 양은 약  $23.6 \pm 3.81 \%$ 임에 반해, 약물이 탑재된 플레이트를 이식한 그룹에서는  $52.78 \pm 6.84 \%$ 으로 약 2 배 이상 뼈가 더 빠르게 형성된 것을 확인할 수 있었다. 이러한 결과를 바탕으로 알렌드로네이트의 국소적이고 서방형 전달이 가능한 본플레이트는 그 자체의 본래의 기능과 골형성을 촉진하는 치료기능이 결합된 시스템이라고 할 수 있었다.

마지막으로, 실리콘 임플란트를 이식 후, 그 주변으로 발생하는 섬유형성(fibrosis)를 감소시키기 위하여 파이브로시스를 유발하는 가장 중요한 사이토카인(cytokine)으로 알려진 티지에프-

베타(TGF- $\beta$ ) 을 염증초기에 국소적으로 억제하고자 하였다. 이를 구현하기 위하여, TGF- $\beta$ 의 억제제(inhibitor)로써 알려진 약물인 트라닐라스트(tranilast)를 5일 그리고 15일 동안 방출할 수 있는 실리콘 임플란트를 제작하였다. 그리고 나서, 살아 있는 동물(rat)모델에 이식하여, 12주 동안 조직학적 분석을 수행하였다. 분석 결과, 12주 후에 약물이 들어 있지 않은 샘플이 이식된 그룹에 비하여 약물이 들어 있는 샘플이 이식된 그룹에서 파이브로우스 캡슐(fibrous capsule)의 두께 및 콜라겐 밀도(collagen density)가 통계적으로 유의하게 감소한 것을 확인할 수 있었다. 이러한 차이는 초기 염증(acute inflammation) 기간 동안 티지에프-베타의 초기 억제에 의한 단핵백혈구(monocyte)의 실리콘 임플란트 주변으로 리크루트먼트(recruitment)의 감소로 비롯된다고 설명될 수 있다. 이러한 현상을 통해 대식세포(macrophage)의 수도 감소하게 되고, 이어서 섬유아세포(fibroblast)의 수도 감소하게 되는 것이다. 그러므로, 최종적으로 염증기간의 후반부에 나타나는 섬유화(fibrous capsule)가 줄어들게 되는 것이다.

---

**핵심어:** 생체고분자, 골접합용 시스템, 코팅, 부식, 섬유화, 실리콘  
임플란트

Student Number : 2012-30967

# APPENDIX

## EDUCATION

- Ph. D. Sep. 2012–Feb. 2015  
Interdisciplinary Program in Bioengineering,  
College of Engineering, Seoul National University  
Supervisor: Professor Young Bin Choy  
Dissertation Topic: SURFACE COATING OF IMPLANTABLE MEDICAL DEVICES FOR ADDING ENHANCED THERAPEUTIC FUNCTIONALITY
- M. S. Sep. 2010–Aug. 2012  
Interdisciplinary Program in Bioengineering,  
College of Engineering, Seoul National University  
Supervisor: Professor Young Bin Choy  
Dissertation Topic: POLYMERIC TUBE-SHAPED DEVICES WITH CONTROLLED GEOMETRY FOR PROGRAMMED DRUG DELIVERY
- B. S. Mar. 2002–Aug. 2010  
Materials Science and Engineering  
College of Engineering, Hanyang University

## PUBLICATIONS

1. Choi, S. Y., Hur, W. J., Kim, B. K., Shasteen, C., Kim, M. H., Choi, L., M., Lee, S. H, Park C. G, Park M., Min, H. S, Kim, S.W, Choi, T.H.\* , Choy, Y. B. \* , Bioabsorbable bone fixation plates for X-ray imaging diagnosis by a radiopaque layer of barium sulfate and poly (lactic-co-glycolic acid), Journal of Biomedical Materials Research: Part B – Applied Biomaterials, in press, 2014
2. Park, C. G., Kim, M. J., Park, M., Choi, S. Y., Lee, S. H., Lee, J. E., Shin, G. -S., Park, K. H., Choy, Y. B.\* , Nanostructured Mucoadhesive Microparticles for Enhanced Preocular Retention, Acta Biomaterialia, 10(1), 77–86, 2014

3. Lee, S. H., Park, M., Park, C. G., Kim, B. H., Lee, J. E., Choi, S. Y., Nam, S. R., Park, S. H., Choy, Y. B. \*, Implantable Microchip for Controlled Delivery of Diclofenac Sodium, *Journal of Controlled Release*, 196(28), 52–59, 2014
4. Lee, J. E., Park, S., Park, M., Kim, M. H., Park, C. G., Lee, S. H., Choi, S. Y., Kim, B. H., Park, H. J., Park, J. –H., Heo, C. Y.\*, Choy, Y. B.\* , Surgical Suture assembled with Polymeric Drug–Delivery Sheet for Sustained, Local Pain–relief, *Acta Biomaterialia*, 9(9), 8318–8327, 2013
5. Park, M., Lee, J. E., Park, C. G., Lee, S. H., Seok, H. –K., Choy, Y. B.\* , Polycaprolactone Coating with Varying Thicknesses for Controlled Corrosion of Magnesium, *Journal of Coatings Technology and Research*, 10(5), 695–706, 2013
6. Lee, J. E. †, Park, C. G. †, An, B. M., Kim, M. H., Park, M., Lee, S. H., Choy, Y. B.\* , Linear Delivery of Verapamil via Nanofibrous Sheet–Based System, *Pharmaceutical Research*, 29(7), 1787–1796, 2012.  
† These authors contributed equally to this work.
7. Park, M., Park, C. G., Lee, S. H., Lee, J. E., Cho, E., Prausnitz, M. R., Choy, Y. B.\* , Polymeric Tube–shaped Devices with Controlled Geometry for Programmed Drug Delivery, *Macromolecular Research*, 20(9), 960–967, 2012.
8. Lee, S. H., Park, M., Park, C. G., Lee, J. E., Prausnitz, M. R., Choy, Y. B.\* , Microchip for Sustained Drug Delivery by Diffusion Through Microchannels, *AAPS PharmSciTech*, 13(1), 211–217, 2012.
9. Park, C. G., Kim, M. H., Park, M., Lee, J. E., Lee, S. H., Park, J. –H., Yoon, K.–H., Choy, Y. B.\* , Polymeric Nanofiber Coated Esophageal Stent for Sustained Delivery of an Anticancer Drug, *Macromolecular Research*, 19(11), 1210–1216, 2011
10. Park, C. G., Kim, E., Park, M., Park, J.–H., Choy, Y. B.\* , A nanofibrous sheet based system for linear delivery of nifedipine, *Journal of Controlled Release*, 149(3), 250–257, 2011

## PATENTS

- International Patents (PCT)

1. A Breast Implant for Controlled Drug Release and a Preparation Method thereof

Chan Young Heo, Young Bin Choy, Min Park, Su Bin Park, Won Seok Lee, Byung Whi Kim

2013. 04. 24 (PCT/KR2013/003486)

2. X-ray Visible Medical Device and Preparation Method thereof

Tae Hyun Choi, Young Bin Choy, Seok Min Kwon, Catherine Ann Shasteen, Sung Yoon Choi, Min Park, Suk Wha Kim

2012. 09. 17 (US Patent Application Number 13621744)

- Domestic Patents (대한민국)

등록 특허

1. 약물의 제어 방출이 가능한 유방 보형물 및 이의 제조방법  
허찬영, 최영빈, 박민, 박수빈, 이원석, 김병휘

2014.10.17 (등록번호 예정)

2. X-선 조영이 가능한 의료용 물품 및 이의 제조방법  
최태현, 최영빈, 권석민, 신윤희, 최성윤, 박민, 김석화

2014. 03. 07 (등록번호 10-1374467)

3. 부분적으로 표면 코팅된 의료용 보철장치

최영빈, 박민

2014. 02. 26 (등록번호 예정)

4. 프로그램형 약물전달을 위한 기하학적으로 제어된 튜브 형태의 디바이스

최영빈, 박민

2013. 09. 05 (등록번호 10-1307680)

5. 접착성 물질을 이용하여 신체 이식 후 이동을 최소화하는 스텐트 및 방법

최영빈, 박민, 신윤희

2013. 01. 29 (등록번호 10-2013-0009771)

출원 특허

1. 생체적합성 고분자 물질 및 흉터형성 억제 약물을 포함하는 의료장치 코팅 제형

허찬영, 최영빈, 박민, 최성윤, 허범강, 김병휘

2014.03.25 (출원번호 10-2014-0034585)

2. 접착성 물질을 이용하여 신체 이식 후 이동을 최소화하는 스텐트 및 방법

최영빈, 박민, 신윤희

2014.03.29 (출원번호 10-2013-0009771)

## HONORS and AWARDS

### 1. 2014년 대한의용생체공학회 우수논문 발표상

Paper entitled with “Acute Suppression of Cysteinyl Leukotrienes with Local, Sustained delivery of Montelukast to Reduce the Capsular Contracture around the Silicone Implants”

### 2. 2013년 서울대학교 바이오엔지니어링 학술제 우수논문 발표상

Paper entitled with “Acute Suppression of TGF- $\beta$  with Local, Sustained Release of Tranilast against the Formation of Fibrous Capsules around Silicone Implants”

### 3. 2013년 서울대학교 의생명연구원 우수논문상

Paper entitled with “Polycaprolactone Coating with Varying Thicknesses for Controlled Corrosion of Magnesium”

### 4. 2012년 서울대학교 의생명연구원 우수논문상

Paper entitled with “Polymeric Tube-Shaped Devices with Controlled Geometry for Programmed Drug Delivery”

### 5. 2011년 대한의용생체공학회 우수포스터 발표상

Paper entitled with “Polymeric Tube-Shaped Devices with Controlled Geometry for Programmed Drug Delivery”

## CONFERENCE PROCEEDINGS

### INTERNATIONAL CONFERENCE

1. S. H. Lee, M. Park, B. H. Kim, C. G. Park, Y. B. Choy\*, Implantable Pump Actuated by Static Magnetic Field for On-demand Drug Delivery, Abstract & Poster Presentation, 2014, CRS 41th Annual Meeting, Chicago, Illinois, USA
2. Park, C. G, Kim, Y. K., Kim, M. J., Park, M., Kim, M. H., Lee, S. H., Choi, S. Y., Lee, W. S., Chung, Y. J., Jung, Y. E., Park, K. H.\* and Choy, Y. B.\* , Nanostructured Mucoadhesive Microparticles for Enhanced Bioavailability of Ocular Drug, Abstract & Podium Presentation, 2014, the 3<sup>rd</sup> Li Ka Shing Foundation International Ophthalmic Research Student Forum, Hong Kong (Best Presentation Award/Grants– Second runner-up in Visual Sciences)
3. Choi, S. Y., Lee, J. E., Kim. B. H., Park, M., Heo, C.Y.\*, Choy, Y. B.\* , Surgical Suture Enabled with Controlled Drug Delivery for Anti-Scarring Functionality, Abstract & Poster Presentation, 2013, CRS 40th Annual Meeting, Honolulu, Hawaii, USA
4. Park, C. G., Choi, S. Y., Park, M., Lee, S. H., Chung, Y. J., Jung, Y. E., Choy, Y. B.\* , Nanostructured Mucoadhesive Microparticles for Enhanced Bioavailability of Brimonidine, Abstract & Poster Presentation, 2013, BMES Annual Meeting, Seattle, USA
5. Park, S. B., Lee, J. E., Park, M., Kim, M. H., Park, C. G., Lee, S. H., Heo, C. Y.\* , Choy, Y. B.\* , Drug Delivery Surgical Sutures for Pain Relief, Abstract & Poster Presentation, 2012, BMES Annual Meeting, Atlanta, USA
6. Park, M., Lee, J. E., Park, C. G., Lee, S. H, Seok, H. K., Choy, Y. B.\* , Polycaprolactone Coating with Varying Thickness for Controlled Corrosion of Magnesium, Abstract & Poster Presentation, 2012, BMES Annual Meeting, Atlanta, USA
7. Lee, S. H., Park, M., Park, C. G., Lee, J. E., Choy, Y. B.\* , Implantable Microchip for Long-term Sustained Drug Delivery, Abstract & Poster Presentation, 2012, BMES Annual Meeting, Atlanta, USA
8. Choi, S. Y., Shasteen, C., Kim, M. H., Park, C. G., Lee, J. E., Park, M., Lee, S. H., Choi, T. H., Choy, Y. B.\* , Barium Sulfate Layer Coating on Bioabsorbable Bone Fixation Plate for X-

ray imaging, Abstract & Poster Presentation, 2012, SPIE Nanosystems in Engineering + Medicine, Incheon, Republic of Korea

9. Park, M., Lee, J. E., Park, C. G., Cho, S. Y., Seok, H. K., Choy, Y. B.\* , Titanium Implants enabled with Vancomycin Delivery for Inhibition of Infection, Abstract & Poster Presentation, 2012, SPIE Nanosystems in Engineering + Medicine, Incheon, Republic of Korea
10. Park, C. G., Park, M., Choi, S. Y., Lee, J. E., Lee, S. H., Shin, G. -S., Choy, Y. B.\* , Nano-structured Microparticles for Prolonged Residence Time on Preocular Surface, Abstract & Poster Presentation, 2012, SPIE Nanosystems in Engineering + Medicine, Incheon, Republic of Korea
11. Lee, J. E., Park, S., Park, C. G., Kim, M. H., Park, M., Lee, S. H., Heo, C. Y.\* , Choy, Y. B.\* , Drug-delivery Surgical Sutures for Post-Surgical Pain Relief, Abstract & Poster Presentation, 2012, SPIE Nanosystems in Engineering + Medicine, Incheon, Republic of Korea
12. Lee, S. H., Park, M., Park, C. G., Lee, J. E., Choy, Y. B.\* , Drug Delivery Microchip for Potential Application to Chronic Pain Relief, Abstract & Oral Presentation, 2012, SPIE Nanosystems in Engineering + Medicine, Incheon, Korea
13. Lee, J. E., Park, S., Park, C. G., Kim, M. H., Park, M., Lee, S. H., Heo, C. Y.\* , Choy, Y. B.\* , Drug-delivery Surgical Sutures for Post-Surgical Pain Relief, Abstract & Poster Presentation, 2012, The 39<sup>th</sup> Annual Meeting & Exposition of the Controlled Release Society, Quebec City, Canada
14. Park, C. G., Park, M., Lee, J. E., Lee, S. H., Shin, G. -S., Choy, Y. B.\* , Nano-structured Microparticles for Prolonged Residence Time on Preocular Surface, Abstract & Podium Presentation, 2012, The 39<sup>th</sup> Annual Meeting & Exposition of the Controlled Release Society, Quebec City, Canada
15. Lee, J. E., Park, S., Park, C. G., Park, M., Lee, S. H., Choy, Y. B.\* , Drug-delivery Surgical Sutures for Post-Surgical Pain Relief, Abstract & Oral Presentation, 2011, The 3rd Asian Biomaterials Congress, Busan, Korea

16. Park, C. G., Kim, M. H., Park, M., Lee, J. E., Lee, S. H., Park, J. -H., Choy, Y. B.\*, Esophageal Stent Coated with Biocompatible Polymeric Nanofibers for Sustained Delivery of an Anticancer Agent, Abstract & Poster, 2011, The 38<sup>th</sup> Annual Meeting & Exposition of the Controlled Release Society, Maryland, USA
17. Lee, J. E. <sup>†</sup>, Park, C. G. <sup>†</sup>, Park, M., Lee, S. H., Choy, Y. B.\* , Controlled Delivery of Verapamil through a Nanofibrous Sheet Barrier, Abstract & Poster, 2011, The 38<sup>th</sup> Annual Meeting & Exposition of the Controlled Release Society, Maryland, USA

<sup>†</sup>These authors contributed equally to this work.

18. Lee, S. H., Park, M., Park, C. G., Lee, J. E., Choy, Y. B.\* , Microchip for Sustained Drug Delivery by Diffusion through Microchannels, Abstract & Podium, 2011, The 38<sup>th</sup> Annual Meeting & Exposition of the Controlled Release Society, Maryland, USA.
19. Park, M., Park, C. G., Lee, S. H., Prausnitz, M. R.\* , Choy, Y. B.\* , Tube-shaped Devices with Controlled Geometry for Programmed Drug Delivery, Abstract & Poster, 2011, Annual Meeting & Exposition of Society for Biomaterials, Orlando, USA

#### DOMESTIC CONFERENCE

1. 박민, 김명훈, 이승호, 박천권, 최성윤, 민혜숙, 최태현\*, 최영빈\*, Bioabsorabale Bone Plates Eabled with Local, Sustained Delivery of Alendronate for Bone Regeneration, 제 22 차 한국생체재료학회 추계학술대회, 2014
2. 박천권, 김영국, 김미정, 박민, 김명훈, 이승호, 최성윤, 이원석, 정유정, 정영은, 박기호\*, 최영빈\* Nanostructured Mucoadhesive Microparticles for Enhanced Bioavailability of Brimonidine, 제 22 차 한국생체재료학회 추계학술대회, 2014

3. 김세나, 박천권, 허범강, 박민, 최영빈\*, Biodegradable Microparticles for Sustained Delivery of Anesthetic Drug, Bupivacaine, 한국 고분자학회 추계학술대회, 2014
4. 김병휘, 박민, 박효진, 이승호, 최성윤, 박천권, 정웅, 한수민, 허찬영\*, 최영빈\*, 실리콘 임플란트 주변 피막구축 억제를 위한 Cysteinyl Leukotrienes 장기간 국소억제, 제 49 회 대한의용생체공학회 춘계학술대회, 2014
5. 이승호, 박민, 김병휘, 임병윤, 박천권, 최영빈\*, Implantable, Drug-delivery Pump Actuated by Static Magnetic Field for Treatment of Chronic Diseases, 제 49 회 대한의용생체공학회 춘계학술대회, 2014
6. 박천권, 박민, 이승호, 최성윤, 이원석, 최영빈\*, Nanostructured Mucoadhesive Microparticles for Enhanced Bioavailability of Brimonidine, 한국 고분자학회 춘계학술대회, 2014
7. 허범강, 최성윤, 박천권, 김병휘, 박민, 허찬영\*, 최영빈\*, A Biodegradable Suture Enabled with Local Delivery of Diclofenac Sodium for Pain Relief, 한국 고분자학회 춘계학술대회, 2014
8. 허우준, 박민, 김명훈, 이승호, 박천권, 최태현, 최영빈\*, Bioabsorbable Bone Plates Enabled with Local, Sustained Delivery of Alendronate, 한국 고분자학회 춘계학술대회, 2014
9. 최성윤, 김병휘, 박민, 박천권, 이승호, 허찬영\*, 최영빈\*, 반흔 형성 억제 기능성 봉합사의 개발 및 효용성 평가, 한국 고분자학회 춘계학술대회, 2014
10. 이원석, 박민, 박천권, 이승호, 예성준\*, 최영빈\*, Surface Modification of Metallic Brachytherapy Seed for Prevention of Migration, 한국 고분자학회 춘계학술대회, 2014
11. 박천권, 김영국, 김미정, 박민, 김명훈, 이승호, 최성윤, 이원석, 정유정, 정영은, 박기호\*, 최영빈\*, Nanostructured Mucoadhesive Microparticles for Enhanced Bioavailability of Brimonidine, 제 9 차 한국생체재료학회 춘계학술대회, 2014
12. 허범강, 김병휘, 최성윤, 박천권, 박민, 이승호, 허찬영\*, 최영빈\* 통증완화 기능성 디클로페낙 서방전달 봉합사 개발, 제 9 차 한국생체재료학회 춘계학술대회, 2014
13. 박천권, 김영국, 김미정, 박민, 김명훈, 이승호, 최성윤, 정유정, 정영은, 박기호\*, 최영빈\*, 브리모니딘 생체이용도 향상을 위한

나노구조 친점액성 마이크로입자, 대한안과학회 제 110 회  
학술대회, 2013

14. 최성윤, 김병휘, 정웅, 박민, 박천권, 허찬영\*, 최영빈\* 흉터 형성 억제를 위한 약물전달기능 생체흡수성 외과용 봉합사, 48 회 대한의용생체공학회 추계학술대회, 2013
15. 이승호, 박민, 박천권, 김병휘, 최영빈\* 디클로페넥 서방 전달을 위한 체내 이식형마이크로칩, 8 회 대한의용생체공학회 추계학술대회, 2013
16. 박천권, 김영국, 김미정, 박민, 김명훈, 이승호, 최성윤, 정유정, 정영은, 박기호, 최영빈\* 브로모니딘 생체이용도 향상을 위한 나노구조 친점액성 마이크로입자, 8 회 대한의용생체공학회 추계학술대회, 2013
17. 박수빈, 박민, 이지은, 박효진, 이승호, 박천권, 허찬영\*, 최영빈\* 실리콘 임플란트 주변 피막구축 억제를 위한 TGF- $\beta$  장기간, 국소억제, 48 회 대한의용생체공학회 추계학술대회, 2013
18. 허범강, 최성윤, 박천권, 김병휘, 박민, 허찬영\*, 최영빈\* 통증 완화를 위한 다클로페낙의 국소전달이 가능한 생분해성 봉합사, 48 회 대한의용생체공학회 추계학술대회, 2013
19. 이승호, 박민, 박천권, 김병휘, 이지은, 최성윤, 최영빈\* "Implantable Microchip for Controlled Delivery of Diclofenac Sodium", 제 9 회 생체재료 아카데미, 2013
20. 최성윤, Chatherine Shasteen, 김명훈, 박민, 이승호, 박천권, 최태현\*, 최영빈\* 흡수성 골고정용 플레이트의 X-선 진단을 위한 황산바륨 레이어 코팅, 47 회 대한의용생체공학회 춘계학술대회, 2013
21. 박천권, 박민, 최성윤, 이승호, 이지은, 최영빈\* 점안부 거주시간 향상을 위한 나노형상 친점액성 마이크로입자, 47 회 대한의용생체공학회 춘계학술대회, 2013
22. 박수빈, 박민, 이지은, 이승호, 박천권, 허찬영\*, 최영빈\* 약물의 국소, 서방전달에 의한 실리콘 임플란트 주변 피막구축 억제, 47 회 대한 의용생체공학회 춘계학술대회, 2013
23. 이승호, 박민, 박천권, 최성윤, 최영빈\*, 디클로페넥 제어 전달을 위한 체내 이식형 마이크로칩, 47 회 대한의용생체공학회 춘계학술대회, 2013

24. 최성윤, 김병휘, 박민, 허찬영\*, 최영빈\* "흉터 형성 억제를 위한 약물전달기능 생체흡수성 봉합사", 한국고분자학회 2013 년도 춘계총회, 2013
25. 이승호, 박민, 박천권, 최성윤, 최영빈\*, 디클로페넥 제어 전달을 위한 마이크로칩 디바이스, 한국고분자학회 2013 년도 춘계총회, 2013
26. 박민, 최성윤, 박천권, 이승호, 최영빈\*, Patterned polymeric coating on titanium bone plate for local, sustained release of vancomycin, 한국고분자학회 2013 년도 춘계총회, 2013
27. 박천권, 박민, 최성윤, 이승호, 최영빈\*, Nanostructured Muco adhesive Microparticles for Enhanced Preocular Retention, 한국고분자학회 2013 년도 춘계총회, 2013
28. 최성윤, 김병휘, 박민, 박천권, 이승호, 허찬영\*, 최영빈\*, 흉터 형성 억제를 위한 약물전달기능 생체흡수성 외과용 봉합사, 제 8 회 생체재료 아카데미, 2013
29. 박천권, 박민, 최성윤, 이승호, 이지은, 최영빈\*, 점안부 거주시간 향상을 위한 나노형상 친점액성 마이크로입자", 제 8 회 생체재료 아카데미, 2013
30. 이지은<sup>†</sup>, 박천권<sup>†</sup>, 안병무, 김명훈, 박민, 이승호, 최영빈\*, 나노섬유시트를 통한 베라파밀의 선형전달, 45 회 대한의용 생체공학회 춘계 학술대회, 2012

<sup>†</sup>These authors contributed equally to this work

31. 최성윤, Catherine Shasteen, 김명훈, 박천권, 이지은, 박민, 이승호, 최영빈\*, Barium Sulfate Film Coating on Bioabsorbable Fixation Plate for X-ray Visibility, 44 회 대한의용생체공학회 추계 학술대회, 2011
32. 박민, 이승호, 박천권, 최영빈\*, Implantable Perforated Tubular Devices, 44 회 대한의용생체공학회 추계 학술대회, 2011
33. 이승호, 박민, 박천권, 이지은, 최영빈\*, Microchip Embedded with Diffusion-Channels and Drug-Wells for Sustained Drug Delivery, 43 회 대한의용생체공학회 춘계 학술대회, 2011
34. 박민, 이승호, 박천권, 최영빈\*, Programmable Tubular Devices for Treatment of Parkinson's disease, 43 회 대한의용생체공학회 춘계 학술대회, 2011

35. 이승호, 박민, 박천권, 이지은, 최영빈\*, Implantable Microchip for Continuous Drug Delivery, 42 회 대한의용생체공학회 추계 학술대회, 2010
36. 이지은, 박천권, 김명훈, 박민, 조은빛, 이승호, 허찬영\*, 최영빈\*, Development of Ibuprofen-delivery Biodegradable Sutures for Pain Relief to the Surgical Wound, 42 회 대한의용생체공학회 추계 학술대회, 2010
37. 박민, 박천권, 이승호, 최영빈\*, Implantable Tubular Devices for Pulsatile Drug Delivery, 42 회 대한의용생체공학회 추계 학술대회, 2010 <우수 논문상 선정>
38. 박천권, 김은지, 박민, 박정환, 최영빈\*, Controlled Delivery of Nifedipine via Nanofibrous Sheet Based System, 42 회 대한의용생체공학회 추계 학술대회, 2010
39. 박천권, 김명훈, 김은지, 조은빛, 박민, 박정환, 최영빈\*, 5-FU 서방전달을 위한 의용고분자 나노섬유로 코팅된 식도 스텐트, 제 18 차 한국생체재료학회 학술대회, 2010
40. 박민, 박천권, 김은지, 최영빈\*, 프로그램형 약물전달을 위한 조립형 튜브 디바이스, 41 회 대한의용생체공학회 춘계 학술대회, 2010
41. 박천권, 김은지, 박민, 박정환, 최영빈\*, 항암제 서방전달을 위한 의용고분자 나노섬유로 코팅된 식도 스텐트, 41 회 대한의용생체공학회 춘계 학술 대회, 2010